NAVAL POSTGRADUATE SCHOOL

MONTEREY, CALIFORNIA

THESIS

INFORMING SYSTEM PARAMETER CONSTRAINTS ON TERRESTRIAL PASSIVE RADAR EXPERIMENTAL DESIGN USING JOVIAN DECAMETRIC RADIATION

by

Karissa J. Nessly

June 2023

Thesis Advisor: Sean T. Peters
Second Reader: Christopher G. Smithtro

THIS PAGE INTENTIONALLY LEFT BLANK

REPORT DOCUMENTATION PAGE	*Form Approved OMB No. 0704-0188*

1. AGENCY USE ONLY *(Leave blank)*	**2. REPORT DATE** June 2023	**3. REPORT TYPE AND DATES COVERED** Master's thesis

4. TITLE AND SUBTITLE
INFORMING SYSTEM PARAMETER CONSTRAINTS ON TERRESTRIAL PASSIVE RADAR EXPERIMENTAL DESIGN USING JOVIAN DECAMETRIC RADIATION

5. FUNDING NUMBERS

6. AUTHOR(S) Karissa J. Nessly

7. PERFORMING ORGANIZATION NAME(S) AND ADDRESS(ES)
Naval Postgraduate School
Monterey, CA 93943-5000

8. PERFORMING ORGANIZATION REPORT NUMBER

9. SPONSORING / MONITORING AGENCY NAME(S) AND ADDRESS(ES)
N/A

10. SPONSORING / MONITORING AGENCY REPORT NUMBER

11. SUPPLEMENTARY NOTES The views expressed in this thesis are those of the author and do not reflect the official policy or position of the Department of Defense or the U.S. Government.

12a. DISTRIBUTION / AVAILABILITY STATEMENT
Approved for public release. Distribution is unlimited.

12b. DISTRIBUTION CODE
A

13. ABSTRACT (maximum 200 words)

Due to recent success in Greenland showing that the Sun can be used as a source for passive radar sounding to monitor glacier and ice sheet thickness, we intend to answer the longstanding question of similarly using Jupiter as a passive radar source. While this theory has been extensively examined in literature, there has been no in situ experiment demonstrating that Jupiter's radio emissions can successfully be used as a passive radar source. Our research evaluated system parameter constraints on terrestrial passive radar system design using Jupiter's radio emissions for the first time. Our results showed that Jupiter's radio emissions are limited spatiotemporally to several hours of the day, which can significantly impact experimental design and planning. We analyzed Jupiter's resolution capabilities and found that the best slant range resolution would be obtained at night with an elevation angle of 50° (4.05m -4.5m), while a 10° elevation angle at noon degraded this resolution. If the technique is effective, it could allow military and DOD users to capitalize on ambient radio signals of opportunity as source for passive radar, reduce spectrum overcrowding, and provide long-term observations of current and evolving threats in complex environments. Additionally, as a passive radar does not, itself, radiate, it has the potential to also be used in situations where an active radar would not be ideal.

14. SUBJECT TERMS
Jupiter, radio emission, passive sounding, passive radar, echo detection

15. NUMBER OF PAGES
113

16. PRICE CODE

17. SECURITY CLASSIFICATION OF REPORT	**18. SECURITY CLASSIFICATION OF THIS PAGE**	**19. SECURITY CLASSIFICATION OF ABSTRACT**	**20. LIMITATION OF ABSTRACT**
Unclassified	Unclassified	Unclassified	UU

NSN 7540-01-280-5500

Standard Form 298 (Rev. 2-89)
Prescribed by ANSI Std. 239-18

THIS PAGE INTENTIONALLY LEFT BLANK

Approved for public release. Distribution is unlimited.

INFORMING SYSTEM PARAMETER CONSTRAINTS ON TERRESTRIAL PASSIVE RADAR EXPERIMENTAL DESIGN USING JOVIAN DECAMETRIC RADIATION

Karissa J. Nessly
Lieutenant, United States Navy
BS, Chaminade University of Hawai'i at Honolulu, 2013

Submitted in partial fulfillment of the
requirements for the degree of

MASTER OF SCIENCE IN SPACE SYSTEMS OPERATIONS

from the

NAVAL POSTGRADUATE SCHOOL
June 2023

Approved by: Sean T. Peters
Advisor

Christopher G. Smithtro
Second Reader

James H. Newman
Chair, Space Systems Academic Group

THIS PAGE INTENTIONALLY LEFT BLANK

ABSTRACT

Due to recent success in Greenland showing that the Sun can be used as a source for passive radar sounding to monitor glacier and ice sheet thickness, we intend to answer the longstanding question of similarly using Jupiter as a passive radar source. While this theory has been extensively examined in literature, there has been no in situ experiment demonstrating that Jupiter's radio emissions can successfully be used as a passive radar source. Our research evaluated system parameter constraints on terrestrial passive radar system design using Jupiter's radio emissions for the first time. Our results showed that Jupiter's radio emissions are limited spatiotemporally to several hours of the day, which can significantly impact experimental design and planning. We analyzed Jupiter's resolution capabilities and found that the best slant range resolution would be obtained at night with an elevation angle of 50° (4.05m -4.5m), while a 10° elevation angle at noon degraded this resolution. If the technique is effective, it could allow military and DOD users to capitalize on ambient radio signals of opportunity as source for passive radar, reduce spectrum overcrowding, and provide long-term observations of current and evolving threats in complex environments. Additionally, as a passive radar does not, itself, radiate, it has the potential to also be used in situations where an active radar would not be ideal.

THIS PAGE INTENTIONALLY LEFT BLANK

TABLE OF CONTENTS

THIS PAGE INTENTIONALLY LEFT BLANK

LIST OF FIGURES

THIS PAGE INTENTIONALLY LEFT BLANK

LIST OF ACRONYMS AND ABBREVIATIONS

AKR	Auroral Kilometric Radiation
bKOM	Broadband Kilometric Emission
CME	Coronal Mass Ejection
CMI	Cyclotron Maser Instability
CML	Central Meridian Longitude
DAM	Decametric Radiation
D_E	Jovicentric Declination of Earth (aka Jovian sub-Earth latitude). This has been measured to vary only +/- 3° over Jupiter's 11.9 year orbital period
DEM	Digital Elevation Model
DSI	Direct Signal Interference
EM	Electromagnetic
FPGA	Field-Programmable Gate Array
FWHM	Full Width at Half-Maximum
FM	Frequency Modulation
GBN	Galactic Background Noise
GPS	Global Positioning Satellite
HF	High Frequency
HFR	High Frequency Receiver
HOM	Hectometric Radio Emission
IPR	Ice Penetrating Radar
kHz	Kilohertz
LTE	Long-Term Evolution
MHz	Megahertz
PSD	Power Spectral Density
QP	Quasi-Periodic
RF	Radio-Frequency

REASON	Radar for Europe Assessment and Sounding: Ocean to Near-surface
RIME	Radar for Icy Moon Exploration
R_J	1 Jovian radius (approx. 71,400 km)
SCR	Signal to Clutter ratio
SNR	Signal-to-Noise ratio
UHF	Ultra-High Frequency
VHF	Very-High Frequency
UV	Ultra-violet
VCZ Theorem	Van Cittert–Zernike Theorem
VBLI	Very Long Baseline Interferometry

ACKNOWLEDGMENTS

This work would not have been possible without the support and collaboration of Dr. Sean Peters, Naval Postgraduate School, Dr. Christopher Smithtro, Naval Postgraduate School, Gregor Steinbrügge, NASA Jet Propulsion Laboratory, Dustin Schroeder, Stanford University, and Andrew Romero-Wolf, Jet Propulsion Laboratory California Institute of Technology.

A portion of this research was carried out at the Jet Propulsion Laboratory, California Institute of Technology, under a contract with the National Aeronautics and Space Administration and funded through the internal Research and Technology Development program.

Simulation results have been provided by the Community Coordinated Modeling Center at Goddard Space Flight Center through their publicly available simulation services (https://ccmc.gsfc.nasa.gov). The IRI 2020 Model was developed by the Committee on Space Research (COSPAR) and the International Union of Radio Science (URSI) at the National Space Science Data Center (NSSDC). The information about a particular model/ model developer can be found at the Model Catalog at CCMC.

THIS PAGE INTENTIONALLY LEFT BLANK

I. INTRODUCTION

A. PURPOSE OF STUDY

As humanity makes greater strides toward becoming a space-faring race, there is an increased need for better technology, advanced materials, and increased capabilities. One of the newer technologies being developed is the use of radio-astronomical sources in place of a transmitter for passive radar. Passive radar can decrease the cost of a more traditional radar consisting of both a transmitter and a receiver by only requiring a receiver. However, the difficulty with passive radar is the user is wholly dependent upon ambient sources in the environment and the nature of the sources themselves. For radar to be useful, one needs to understand various characteristics of the signal and whether those signals are predictable to ensure signal processing is capable of meeting requirements. Developing more accurate signal processing and characterizing previously underutilized signals opens the door to advanced techniques that can be applied both terrestrially and in a space environment. Passive radar from space holds the promise of long-term climatological monitoring, remote sensing of our solar system, both for exploration and for security purposes, as well as the development of new code and signal processing techniques that will improve our ability to "see" and "hear" quietly.

Outside of our Sun, Jupiter is the loudest source of radio signals in our galaxy [1]. Its decametric (DAM) radiation (3-41MHz) levels are orders of magnitude larger than the galactic background, which makes it an ideal secondary source and several suggestions have been put forth to use Jupiter's radio emissions to investigate Jovian moons, specifically Europa, to locate subsurface oceans in the search for extraterrestrial life [1].

The initial problem is Jupiter's radio emissions are loud enough to drown out space-based radio observations [1]. In fact, they are five orders of magnitude louder than the galactic background radiation, which makes them a very noisy object in our solar system [1]. In a paper published in 2019, Gerekos et al., ran a simulation of active sounding at Europa. Their work showed during an active Jovian burst, the noise from Jupiter would drown out any active sounding instruments carried aboard a spacecraft [2]. Additionally,

they showed if an active sounding occurred when a Jovian burst was not occurring, then the signal environment was clean enough to obtain an active sounding of Europa [2]. Consequently, from their research we can conclude radar sounders in space would need a significant amount of radiated power to drown out Jupiter's interference, which would make the production of the spacecraft prohibitively expensive. A need for an increase in radiated power from a traditional transmit/receive radar requires greater capability of both the spacecraft itself and the technology onboard. These needs translate to additional equipment, leading to a heavier spacecraft requiring additional engineering to ensure it is structurally sound. This heavier spacecraft requires additional fuel for launch and may even require a heavier rocket to ensure the spacecraft achieves escape velocity.

An answer to this problem would be to utilize Jupiter's radio signals as a source for passive radar sounding, requiring only a receiving antenna to capture the echo that would then be analyzed to determine a variety of characteristics of the subsurface of Europa. While this has been suggested, it has never been attempted. Additionally, this method could be applied to several terrestrial applications such as glaciological monitoring, long-term environmental observations, and more immediate impacts from global warning on navy shipyards and docks. Any experimental design to use Jupiter as a source for passive radar would need to consider Jupiter's temporal availability, its frequency useability, and its spatial coherence. This thesis answers those three questions and establish system parameter constraints when designing terrestrial passive radar experiments utilizing Jovian radio bursts for echo detection.

The organization of this thesis is as follows. The remainder of this chapter is dedicated to reviewing information on radio-astronomical sources as well as radar. Chapter two covers historical data and studies of Jupiter divided into three sections: Jupiter's radio environment, Jupiter's emission characteristics, and passive sounding applications to the Jovian system. Chapter three is a breakdown of what we know about Jupiter as a source of DAM radiation. Chapter four is the experimental setup and results, focusing on informing terrestrial passive radar experiment design and system parameter constraints using Jovian radiation. Chapter five discusses conclusions and areas for future work in the area.

B. HISTORICAL RADIO-ASTRONOMICAL SOURCES FOR PASSIVE RADAR

Our Sun is the most well-known body within our solar system to be associated with electromagnetic radiation emissions. A class G2V star (yellow dwarf star), it's surface temperature of approximately 5,800 K is mild in comparison to a core temperature of 15 million K [3]. Solar radio emission was identified in 1942 with scientists initially noting the radiation appeared in the centimeter frequency, but was later also identified in the frequency range of 40 to 200 MHz[4]. Additionally, the radio emission was observed simultaneously with the appearance of sunspots, thus making it prone to rapid fluctuations [4]. Later observations of solar radio emissions suggest there may be many different mechanisms for solar bursts, but they are not fully understood [4].

Physicists have determined the Sun emits both electromagnetic (EM) radiation (radio waves to gamma-rays) and corpuscular radiation (e.g., the solar wind) [3]. Within EM radiation, the spectral distribution of the Sun is as follows: 10–8% radio waves, 41% visible light, 52% infrared radiation, 7% near-infrared radiation, and 0.1% ultraviolet and x-ray radiation [3]. Much like the Earth, the Sun is composed of various layers where different processes take place. Fusion occurs within the core of the Sun, outside of which is a layer known as the radiative transport layer wherein gamma-rays lose energy and become x-rays, ultraviolet rays, visible light, and radio waves [3]. In the outer convective layer, the movement of plasma provides most of the transport energy, which can be seen on the photosphere, the visible surface of the Sun, as sunspots, granulation, and other surface phenomena [3]. Outside of the photosphere is a region of cooler plasma known as the chromosphere [3]. Solar flares and solar prominences can be seen active between the photosphere and chromosphere, and beyond in the case of solar flares and coronal mass ejections (CME) [3].

More generally, the Sun provides a temporally incoherent source of radiation with a finite angular extent for the full disk (for radio frequencies) viewed at Earth with random phase fronts (which are not perfectly planar) and thus a finite radius of coherence [5]. In the absence of sunspots and solar burst activity, the emission is approximately uniformly distributed across an area only a few percent larger than the visible disc of the Sun with

minor limb brightening variations at lower radio frequencies; however, this effect is only significant when the antenna beam width is less than the angle subtended by the Sun [5]. Thus, the Sun's limited temporal availability and wide angular extent further motivates the development of passive radar using Jupiter's radio emissions (which has a much smaller source size ranging from 20 km to enable sounding across polar fieldwork seasons where a single source is not available [5]. To this effect, the temporal and structural characteristics of Jovian bursts have also been analyzed over a range of radio frequencies of interest for passive radar sounding and is discussed further in Chapter II.

C. PASSIVE RADAR CONCEPT OVERVIEW

For passive radar sounding, a single receiver measures both the direct and reflected signals and extracts the reflections by identifying delayed peaks in the autocorrelation of the received waveform. Traditional passive radars rely on coherent anthropogenic sources (e.g., frequency modulated (FM) radio, Digital Video Broadcast, long-term evolution (LTE), and (global positioning satellite (GPS)) for low-resource echo detection, target tracking, and imaging. The incoming signal may either originate from the system itself, (monostatic active sounding), or originate from a separate transmitter (bistatic active sounding) [2]. The system is known as passive sounding if the emission is generated by a secondary source with unknown properties [2]. Passive sounding relies on signals of opportunity that originate from one, or even several, sources [2]. These signals of opportunity produce reflections, or echoes, when said signal encounters sudden changes of, as Peters et al. put it, the "dielectric constant across the propagation volume, such as the surface of a body, possible subsurface layers, and/or discrete diffractors within the subsurface" [2]. In essence, when these echoes or reflections encounter differences in material characteristics through whatever medium they are propagating through, those differing materials produce echoes with different characteristics. From the characteristics of these reflected signals, it is possible to determine a variety of characteristics of the targeted medium, such as surface topography or subsurface composition [2].

Passive radars have shown great promise for performing remote sensing and overcoming spectrum congestion; however, major challenges for passive radar remote

sensing include the lack of user control over the source waveform, power, location, and timing. Moreover, planetary environments (such as Mars and Europa) do not possess well-characterized, human-made radio sources that could be used for passive radar sensing applications [5]. Recent work has thus expanded passive radar techniques to also include temporally incoherent radio-astronomical sources, such as using the Sun for ranging and passive radar sounding of glaciers, as well as [5] exploring Jupiter's radio emissions as potential signals of opportunity for passive radar sounding of the Earth's polar regions and Jupiter's Galilean moons [6]. Figure 1 illustrates two possible paths for passive radar geometry. There is a direct path from the signal to the receiver and there is a reflected path from the signal to a reflection surface to the receiver. The reflected path is the focus of this thesis.

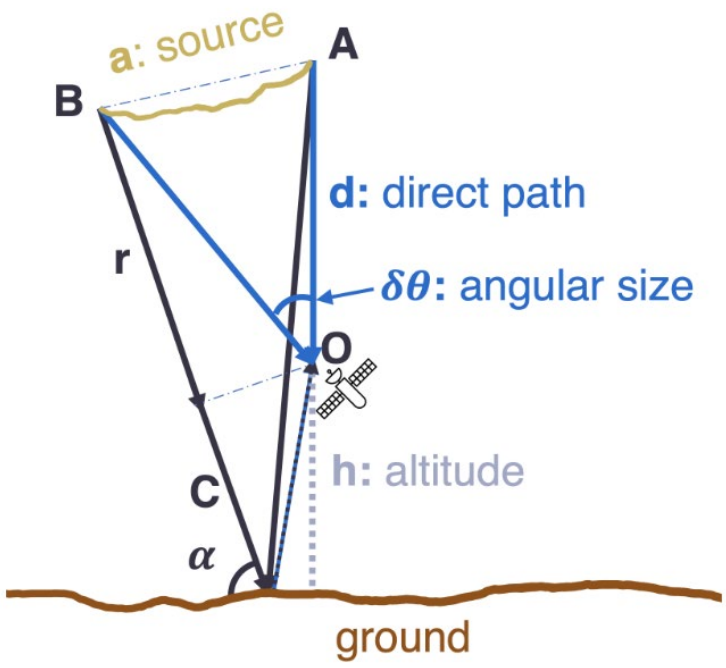

Figure 1. Passive Radar Geometry Showing a Direct Path and a Reflected Path to a Receiver at an Altitude of Height h. Source: [5].

Peters et al. [5]. showed the intensity pattern of an interferometer experiment decays with increasing path length difference, while the echo peak in the autocorrelation technique does not experience this path difference degradation [5]. The loss of the signal's

coherence due to pulse broadening has been analyzed for passive radars using radio-astronomical sources as a function of source size, incidence angle, and orbital altitude; however, additional work is needed to fully analyze the spatial coherence limitations and effects imposed by radar wavelength for passive sounding and better define its relationship to pulse broadening [5]. Providing these spatial coherence constraints on passive sounding is therefore crucial for determining the viability and design of future terrestrial and planetary passive sounding experiments, which can have parameters over a wide range of orbital altitudes, incidence angles, and radio frequencies of interest [5].

Accordingly, there has been increasing interest in developing signals of opportunity for monitoring the cryosphere, as there exists a range of signals (both radio-astronomical and anthropogenic) that can be exploited to monitor processes across a range of glaciological settings (mountain glaciers, ice sheets, and ice shelves) as well as observable glaciological targets, storage of water, and snow water equivalent techniques [7]. In such an environment, arrays and interferometric imaging techniques could be used to determine the direction of arrival for these sources and increase a passive radar's spatiotemporal coverage [7]. Moreover, anthropogenic sources (again consisting of GPS, ultra-high frequency (UHF), very high frequency (VHF), and even high frequency (HF) signals) as well as radio-astronomical signals, could enable passive radio-frequency sensor networks to create much richer, widespread monitoring of these remote regions and other environmental signals within the Earth system[7].

Recent work has therefore projected the performance of future passive radar sounding deployments in terms of signal-to-noise ratio (SNR) and seasonal availability across Greenland and Antarctica using the Sun [7]; however, additional analysis is needed to address the issue of spatial coherence (due to the spatial extension of ambient radio noise sources) [5] and determine the applicability of the technique over a hypothetical range of experiment conditions where resources (i.e., power, size, mass, and data volume) are limited [7].

D. PASSIVE RADAR SIGNAL PROCESSING

Signal processing is an essential step of passive radar analysis and can include a wide variety of techniques. The primary ones discussed within this work are 1) radio frequency interference filtering [8], 2) spectral stitching [8], 3) autocorrelation processing [8] and, 4) SAR focusing [9] .

Radar measures the distance of a given target (either on the surface or subsurface) by assessing the gaps between observed echoes [8]. Experiment designers need to keep in mind that the radar's range resolution is driven by the main lobe while sensitivity to weak signals beneath a given surface is driven by side lobes. The autocorrelation technique discussed in section II.B.1 utilizes a subsurface waveform to determine the point spread function (a method of using an impulse to determine the responsiveness of an optical focusing system) of the passive radar [10]. Section II.B.1 also discusses the need for onboard radio frequency interference filtering to ensure that the desired frequencies are captured, while the unwanted/interference frequencies are discarded [10]. If not filtered out, interference frequencies can deteriorate system performance as interference increases the noise floor, which could mask subsurface reflections [10].

Historically, Jovian radio bursts were assumed to be white noise and any experimental change from that assumption resulted a degradation of the range resolution as well as echo masking [8]. It has also been noted that while experimental changes can impact white noise assumption results, other sources could be at play such as interference generation by instrument electronics [8]. To increase the frequency range, researchers can combine passive echoes from nonoverlapping sub-bands, a process known as Spectral Stitching [8]. In other words, multiple sub-bands can be sampled, and the resulting spectral data can then be combined into one data product for analysis.

SAR focusing is a well-known signal-processing technique and requires a sensor to produce its own energy to illuminate a target and collect the echo [9]. The technique improves signal to noise ratios, making this technique desirable for passive radar sounding in situations that have high attenuation losses [9]. However, Peters et al. [9] utilized a different passive SAR processing technique known as backscattering in their 2021 paper.

To perform SAR processing, back-projection is an attractive focusing algorithm because it avoids approximations and assumptions that break down for other techniques within several limitations that occur at lower frequencies [9]. However, not only is back-projection more computationally expensive, but the entire technique itself is also an active sounding technique and should be utilized in conjunction with passive sounding techniques with care [9]. The data requirement for SAR sounding is extensive and would tax a system to its limits [9]. Peters et al. suggest the use of a field-programmable gate array (FPGA) which would reduce the onboard data volume storage requirement by implementing onboard processing and storing the final processed result [9]. Lowering the data volume requirement would allow the use of maximum passive SAR focusing integration time and would increase the SNR of the passive radar and make the passive SAR technique comparable to an active system's SNR [9].

II. BACKGROUND

A variety of studies of Jupiter and its decametric (DAM) radiation have been conducted over the years; however, it is only recently that Jupiter's radiation has been studied with the intention of using it for future passive sounding applications. This chapter provides an overview of the historical data of Jupiter's radiation environment. The final section focuses on the application of passive sounding, signal processing for radio-astronomical sources, as well as a specific application of using Jovian DAM passive sensing for Galilean Satellites.

A. JUPITER RADIO EMISSION CHARACTERISTICS

As was previously mentioned, for passive radar one of the key factors is the ability to predict the characteristics of the signal being utilized. That requirement is equally important to our study of Jupiter. Using Jupiter as a source for passive radar sounding is only possible if its decametric radio emissions are predictable. Therefore, this section briefly touches on what is known about Jupiter's radio emission characteristics.

1. Temporal and Structural Characteristics of Jovian Radio Emissions

The Juno waves instrument in 2016 characterized Jovian DAM emissions between 3 and 41MHz [8], a characterization that agreed with earlier observations [2], [7], [11]. Jupiter DAM radiation has been effectively utilized for surveying the subsurface of the icy Galilean satellites using passive radio sounding [8]. However, since conclusions of various studies utilizing the DAM radiation data were based on the faulty assumption that Jovian radio noise is white and stationary, additional investigation into temporal availability, probability of occurrence, and spectral characteristics of Jovian noise is necessary for further detailed studies [8]. Newer studies have concluded Jupiter's DAM are not perfect white noise, but neither are there severe distortions in the projected range results. [8]. The result is Jovian DAM has a varying probability of occurrence for some frequency ranges and locations and may prove sporadic for these characteristics over time [8]. Experimental results suggest a large bandwidth receiver would increase the probability of recording Jovian noise in greater detail for follow-on analysis [8].

Radio waves transmitted into a targeted medium result in signal reflections, also known as echoes and are detected and recorded by a receiving antenna [8]. Radar systems calculate a distance to a target by receiving echoes and calculating the delay in its return to the antenna [8]. Radar designers should take into consideration that range resolution is driven by the width of the main lobe while the side lobes influence the system's sensitivity to detect weak reflections from the subsurface [8].

Correlating the reflected signals with the corresponding direct path leads to an estimation of echo amplitude delays from which it is possible to calculate subsurface structure and composition [8]. Correlating direct emissions and reflected signals results in estimations of echo delays and amplitudes [8]. The DAM frequency range is ideal for passive radar at Europa as it's above Europa's ionospheric critical frequency, has a larger exploitable bandwidth leading to enhanced resolution of subsurface features, and is detectable from the ground, since it's above Earth's ionosphere cut off, allowing for the potential of terrestrial experiments (though the presence of distortions from the ionosphere should be considered in terrestrial experimental design) [8]. The severity of ionospheric distortion is a function of emission frequency; therefore, it is more likely to become an issue for lower frequencies [8]. Terrestrial observations have linked DAM emission with the Central Meridian Longitude (CML) of Jupiter and to Io's orbital position with regard to the observer's geocentric conjunction [8]. As such, the probability of collecting a DAM emission is dependent on the CML's specific value as well as the geocentric conjunction calculated with respect to the observer's position [8].

Carrer et al. noted Jovian DAM has an average probability occurrence of 0.2 which correlates to about 5 cumulative hours of observation each day [8]. Understanding the temporal and spectral properties of Jovian DAM is required before undertaking a more realistic design and assessment of the performance of radar passive sounding [8]. Further analysis of Jovian DAM shows there is a reasonable expectation for the possibility of a subsurface detection from orbit [8]. While it is not possible to extend the frequency range of current spaceborne sensors to allow for collection on a larger bandwidth, Carrer et al. suggest the entire recording of passive recording could be uploaded to the onboard memory and then downlinked back to Earth for continued analysis [8]. For future missions, Carrer

at al. [8] recommend having onboard "radio frequency interference filtering, spectral stitching, and autocorrelation processing (reducing data volume) capabilities" [8]. Radio frequency interference can deteriorate performance as it increases the noise floor, which could mask subsurface reflections [8].

Any change from a white noise assumption can cause a degradation of the system resolution as well as increase the likelihood of echo masking [8]. The impacts of this change in assumption, can be mitigated using several using signal processing techniques [8]. One such method for increasing frequency range of passive sounding is to combine echoes collected at nonoverlapping sub-bands, a technique known as Spectral Stitching [8]. While changes in white noise assumption can impact experimental results, experimental results can be impacted by interference from instrument electronics [8]. Because of the chance of this degradation or echo masking, passive radar systems should be designed with extremely low distortion tolerances [8].

2. Jupiter's Decametric Modulation Lines

Modulation lanes within Jupiter's radio spectra were observed in 1968, but our understanding of the underlying magnetospheric processes leading to these modulation lanes is not fully understood [12]. The most apparent feature of these modulation lanes are Long bursts (L bursts) [12]. L bursts have a timescale of approximately 1 to 10 seconds [12]. Radiation acquires its L burst structure because of scintillation when it propagates through the randomly drifting plasma inhomogeneities of the solar wind between Jupiter and Earth [12]. However, if the timescale is shortened to around 0.2 seconds and the bandwidth decreased to a few MHz, another type of structure is revealed [12]. This is the structure of the modulation lanes discovered by Riihimaa [12]. The spectral regions occupied by individual L bursts of randomly varying sizes and shapes extend over 2 to 5 MHz and last about 1 to 10 seconds, with little to no systematic variation of the frequency [12]. On the other hand, modulation lane spectra consist of groups of equally spaced intensity alterations having separations of approximately 2 seconds, sloping together upward or downward in a frequency, often over a range of 5MHz or more [12]. Such a set of sloping parallel lanes of alternating minima and maxima may pass continuously from L

burst to another suggesting the L burst structure was impressed farther along the propagation path than was the modulation lane structure [12].

Modulation lanes have been classified based upon the sign of the frequency-time slope (positive slopes trend upward to higher frequencies and vice versa) [12]. Most modulation slopes have been observed in the vicinity of 23MHz with slopes of +/- 100 kHz/s and +/- 150kHz/s [12]. Imli et al. [12] assumed the modulation lanes are an interference pattern produced by the passage of the DAM radiation through a two-dimensional screen between Io's orbit close to the longitude of the sub-Earth point [12].

The Io-excited flux tube is not perfectly perpendicular to the equatorial plane; its longitude changes with the source height above the plasma [12]. As a result, the longitudinal locations of the fan-lobed interference patterns are different for different heights, and therefore for different source emission frequencies [12]. Radiation passing through enhanced plasma columns scatter at a higher frequency than those which pass through lower-density plasma columns [12]. Imai et al. state that the "intensity maxima occur in those directions for which the path length differences from successive enhanced scattering columns to the wavefront differs by zero or an whole integral number of wavelengths whereas intensity minima occur for directions in which the path differences are odd numbers of half-wavelengths" [12]. Imli et al. observed that the impact of the Jovicentric Declination of Earth (D_E) on DAM emissions results in a "significant impact on the North-South component of the direction of Earth from Jupiter" [12]. They also note that this has a profound effect on the statistical properties of the Jovian DAM received on Earth [12]. As an example, the probability of occurrence of non-Io-A emissions drops "abruptly to near zero as the 2–3 year period of the most negative D_E is approached" [12].

3. Decametric Bursts

Below 40MHz, Jovian radio signals are dominated by sporadic, but very intense cyclotron emissions from Jupiter's high latitudes [13]. Frequencies higher than the radio noise are a combination of synchrotron radiation from Jovian radiation belts and galactic background radio signals [13]. High latitude emissions are in the 3–40MHz range (DAM) and correspond to cyclotron frequencies along magnetic field lines between the extent of

the Jovian ionosphere and the border with the equatorial Io plasma torus [13]. Due to the cyclotron maser instability requiring high energy electrons and an unstable electron distribution, Jovian radio bursts have a spectral cut off at 40MHz [13]. These radio bursts have an anisotropic beaming pattern and elliptical polarization, requiring the observer to be in line of sight with the direction the emission is traveling [13]. DAM emissions have a large opening angle, between 70° and 90°, though the direction of the emission is determined by the plasma density profile and the distribution of electrons [13]. There are four categories for emission phases: 1) A and C ranges have a 270° phase and 2) B and D ranges have a 90° phase [13]. The dynamic and variable behavior of the Jovian electron belt has been linked to solar activity [13].

Very long baseline interferometry (VBLI) observations, approximately around 18MHz, were undertaken to obtain measurements of the source size of Jupiter's DAM bursts [14]. This specific type of interferometer requires a high SNR, something easily achieved by extremely powerful DAM emissions [14]. Carr et al. suggest that the "most plausible theory of the origin of Jovian decametric bursts is the radiation is emitted coherently at the local electron frequency from the relatively low altitude of the Jovian ionosphere, within the bounds of the tube of magnetic flux passing through the satellite Io" [14]. The factor determining the duration of an individual short burst (S burst) might be the lifetime of the coherence of a particular group of radiating electrons, or it might be the time required for the beam from a rotating or wobbling coherent source to sweep past the receiving station [14]. If the former supposition is correct, there does not appear to be a way to terrestrially measure the source size, however, if the latter is correct, there should be a way to capture the delay in the arrival from one end of the baseline to the other [14]. From the measurement of the delay for a given reference, it should be possible to calculate the angular velocity of the emission beam [14]. The velocity along with the measured burst duration would allow the researcher to determine the angular width of the beam, and from there the size of the coherent source could be quickly determined [14].

4. Emission Characteristics Significant to Thesis

Decametric radiation exceeds Earth's ionosphere cut off, making Jovian DAM detectable from the ground for terrestrial sounding missions [8]. However, radio frequency interference can raise the noise floor, potentially resulting in masking of reflections returning from the subsurface [8]. Spectral stitching can extend the available frequency range by combining echoes from nonoverlapping sub-bands [8]. While experimental results (echo masking, range resolution degradation, etc.) can be impacted by a deviation from the assumption of Jovian signal as white noise, these deviations can also be caused by interference generated by the instrument electronics; therefore, system design must be carefully considered when crafting the experiment [8].

Within Jovian bursts, modulation lanes have been observed and categorized [12]. One of the more prominent modulation lanes is known as long bursts (L bursts) [12]. L bursts have a timescale of approximately 1 to 10 seconds and may acquire their structure due to scintillation in the solar wind between Jupiter and Earth [12]. The Jovicentric Declination of Earth (D_E) has a significant impact on DAM signals originating North-South of the bearing of Earth from Jupiter impacts the properties of signal ultimately received on Earth [12].

We know that Jovian DAM has a spectral cutoff at 40MHz and corresponds to magnetic field line interactions between the Jovian ionosphere and the Io plasma torus [13]. Because these bursts have an anisotropic beaming pattern and elliptical polarization, it requires the observer to be in line of sight with the direction the emission is traveling. However, we also know that these bursts have a large opening angle, between 70° and 90° [13]. There are four categories for emission phases: 1) A and C ranges have a 270° phase and 2) B and D ranges have a 90° phase [13]. Measurement of a DAM burst delay should enable observers to calculate the angular velocity of the emission beam [14]. The velocity combined with the burst duration would yield the angular width of the beam enabling the calculation of the coherent source size [14].

B. INFLUENCES ON JUPITER'S RADIO ENVIRONMENT

Jupiter's magnetosphere produces radio signals from <1kHz to approximately 40MHz [8], [12], [13]. This broad bandwidth makes it more intricate than any other planetary source in the solar system [15]. Jovian emissions that exceed Earth's ionospheric cutoff frequency of approximately 10MHz have been detected on the surface, while lower frequencies have been observed in space [15]. Some of the components are very powerful, Jovian DAM radio emissions magnitudes are comparable to solar radio emissions. The electron cyclotron instability is the mechanism behind high-latitude emissions and the structure of these emissions can be modeled with a fair amount of accuracy [15]. In contrast, low-latitude emissions are produced by mode conversion mechanisms but are less quantitatively documented [15]. Earth-based studies have always been limited to within plus or minus four degrees of Jupiter's equator and, with few exceptions, space-based studies have remained limited to within a few degrees of the equator [15]. The Juno probe is one of those exceptions and operates in a polar orbit around Jupiter [15]. Juno provides scientists with a complete sampling of all the observable latitudes in an effort to understand the overall emission component as a function of the Jovian latitude [15]. Jupiter's low frequency radio spectrum includes a variety of elements between 1KHz and 40MHz [15]. Quasiperiodic (QP) bursts comprise the lowest frequencies and include a range from roughly 1kHz to 20–30kHz [15]. They were named Jovian Type III bursts with bursts occurring around 15-minute and 40-minute intervals [15]. Observations suggest they are emitted from auroral regions and generate drifting tails due to complex propagation mechanisms [15]. Observers believe that QP burst nature is related to outer magnetosphere electron bursts [15].

Broadband kilometric emission (bKOM) lies above 20kH, up to a few hundred kHz, and is made of sporadic, often drifting, features [15]. Originating along high-latitude, auroral field lines, with an apex at 15–60R_J from the planet, bKOM is produced cyclotron maser instability (CMI) [15]. Above 200–300kHz is hectometric (HOM) emission, which is much more steady than bKOM and observed at longitudes approximately in antiphase from bKOM, along field lines with an apex similar to, or slightly lower than bKOM, [15]. DAM radiation ranges from 3MHz to 41MHz [15]. It is the only low-frequency planetary

radio emission detectable from the ground above Earth's ionosphere cut off (~10MHz) [15] and is produced primarily near the CMI [15].

DAM is induced by the interaction of Jupiter's magnetic field with Ganymede, Europa, and Io [15]. It is possible to distinguish between these sources based on the time-frequency shape of the emission [15]. At larger distances, the auroral component of DAM fades out and only Io-DAM emissions remain visible [15]. Horizontal emission gaps are due to interference [15]. DAM intensity is nearly even at all latitudes but that result may be slightly biased if a fraction of the HOM signal is included in the subtracted background [15]. Its occurrence remains high up to 90 degrees, with two relative minima in the ranges from +/- 30–20 degrees [15]. HOM occurrence is significantly higher than DAM [15]. DAM consists of a population of time-frequency arcs not exceeding 20MHz detected over a broad range of latitudes [15]. No intense northern (high-frequency) emission seems to be detectable below -10 degrees [15].

1. Jupiter and Ganymede

In their 2018 paper, Zarka et al. investigated empirical scaling laws that were derived to determine whether the primary engine of the radio emission "is the kinetic or magnetic power input from the solar wind to planetary magnetospheres" [10]. To determine which scaling law applied, Zarka et al. generalized the paradigm of solar wind-planet interaction to "the interaction between a magnetized flow and conductive obstacle (magnetized or not) leading to dissipation of the flow's power (kinetic and magnetic) on the obstacle." They also noted that a fraction of this dissipation went into electron acceleration and precipitation of generating radio emissions [10].

This model can be extended to the interactions of Jupiter with its moons [10]. The flow of magnetic energy between magnetic reconnection between Io and Ganymede dominates interactions of Jupiter's magnetosphere [10]. The central meridian longitude (CML) changes with planetary rotation and satellite's orbital phase [10]. Satellite influence on radio emissions can result in enhanced occurrence probability [10]. Circular polarization sense and time-frequency shape of emission are specific for each region [10]. Auroral radio emissions resulting from non-Io emissions exhibit polarizations and time-frequency shapes

that can be categorized (i.e., northern and southern sources can be seen near both limbs of the planet) [10]. No emission with a frequency >33 MHz is detected in regions of enhanced probability for non-Io northern emissions [10]. No emission with a frequency >27MHz is detected in regions of enhanced probability in the CML-Ganymede phase plane for non-Io southern emissions [10].

Ganymede-Jupiter radio emissions are approximately 7.8 times less frequent but only 0.5dB weaker on average than Io-Jupiter and non-Io emissions [10]. Ganymede-Jupiter emissions are approximately 1.7 times shorter than Io-Jupiter emissions and have an average magnitude approximately 15 times lower than that Io-Jupiter radio emissions [10]. The temporal behaviors of Ganymede-Jupiter and Io-Jupiter are very different. Ganymede-Jupiter emissions occur 7.8 times less frequently than Io-Jupiter emissions, last 1.25 times longer than non-Io auroral emissions but are 1.7 times shorter than Io-Jupiter missions [10]. When planning for observations, researchers should note that CMI emissions are anisotropic and within a few tens of minutes, Jupiter's rotation carries the beam out of the observer's view. [10].

2. Jupiter and Io

Jupiter's sodium nebula (the largest permanently visible structure in the solar system) grew in size in late May through the beginning of June 2007, indicating an uptick in Io's volcanic activity and an increase of magnetospheric plasma density [11]. Conversely, Jupiter's HOM radio emission, which is related to Jovian auroral activity, became quiet after the sodium nebula grew [11]. These observations suggest that increasing plasma supply from Io weakens Jupiter's field-aligned current, which decreases the emissions and aurorae on Jupiter [11].

Jupiter obtains magnetospheric plasma from Io's atmosphere via the Io plasma torus [11]. The electrons produced by volcanism on Io are ionized in Io's day-side ionosphere before reaching the Io plasma torus later in the process [11]. Although Jupiter's inner magnetosphere is populated by heavy ions, influence from the solar wind cannot be discounted as Jupiter's HOM radiation depends on the solar wind dynamic pressure and

ultra-violet (UV) aurorae triggered by shocks in the solar wind [11]. Because of this feature, HOM activity can be used as an index of Jupiter's auroral activity [11].

Jupiter's inner magnetosphere receives most of its energy from planetary rotation, with the Io torus serving as a source for plasma, however the solar wind appears to influence its variability [11]. HOM measurements indicated that its intensity was weak (nonactive) around the period when plasma was abundant and resulted in smaller HOM bursts seen before a plasma event [11]. A wide range of HOM emissions are seen before nebula growth, but strong emissions occur less frequently after the enhancement, indicating that an increase in plasma appears to decrease the rate of HOM emissions [11]. The sensitivity of HOM emission regarding Io volcanic activity is unknown [11]. Additionally, decay in HOM has only been seen only at specific longitudes and may imply that the drop in field-aligned current intensity from the increase of plasma from Io only occurs at particular longitudes and in specific hemispheres [11].

3. Importance of Jupiter's Radio Environment to Thesis

We can conclude that several different emission mechanisms produce a wide range of electromagnetic frequencies emanating from Jupiter [10]. HOM, bKOM, and DAM are all potential signals for remote sensing, but the one we are interested in is DAM, as it has a terrestrially detectable frequency range of approximately 10MHz to approximately 40MHz [10]. We also know where these signals are generated regarding Jupiter's central meridian longitude (CML) [10] and that these DAM signals are influenced by interactions with the Jovian moons [10].

Jupiter's central meridian longitude (CML) varies with planetary rotation and the orbital phase of the satellite [10]. Satellites influence radio emissions and the probability of emission occurrence [10]. Non-Io emissions include auroral radio emissions as well as emissions possibly caused by satellites other than Io and possess characteristics that can be classified and categorized for further identification [10]. Because Ganymede's flux tube footprint lies northward of Jupiter's norther high-amplitude magnetic anomaly and is crossed by the northern Io flux tube footprint, no electron cyclotron frequencies >33MHz

are reached [10]. Frequencies >27MHz have not been detected in the CML-Ganymede phase plane for non-Io southern emissions [10].

From the analysis we conclude that the CMI operates at a relatively uniform efficiency around Jupiter resulting in similar intensity distributions for all radio components [10]. We can also delineate between Io-driven and Ganymede-driven bursts. Ganymede-Jupiter emissions were observed to be 7.8 times less frequent than Io-Jupiter/ non-Io emissions but were only 0.5dB weaker [10]. Ganymede-Jupiter emissions lasted approximately 1.7 times shorter than Io-Jupiter emissions but were 1.25 times longer than non-Io emissions [10]. Ganymede-Jupiter emissions were observed to be 15 times lower in power than Io-Jupiter emissions [10].

Jupiter's field-aligned current decreased with an increase of plasma supply from Io into Jupiter's magnetosphere, generating Jupiter's aurorae and its radio emissions [11]. The Io plasma torus changes Io's atmosphere into magnetospheric plasma, generating neutral particles and heavy ions populate that Jupiter's inner magnetosphere [11]. This volcanically supplied stream of electrons is ionized in Io's day-side ionosphere before entering the Io plasma torus [11]. Jupiter's ultra-violet (UV) aurorae are triggered by shocks in the solar wind and Jupiter's hectometric (HOM) radiation can be used as an index of Jupiter's auroral activity to predict other Jovian radiation emissions [11].

C. PASSIVE SOUNDING APPLICATIONS

Passive sounding using radio-astronomical sources is a new technique and still in development, but there are hopes in the scientific community that it will prove useful not only for observing and monitoring our own environment, but also for the exploration of our neighboring planets and moons.

1. Passive Radar using Radio-Astronomical Sources

Passive radars are beginning to show promise as a low-resource remote sensing approach [9]. Such implementations would be useful for glaciological monitoring at large spatial scales [9]. This radio-echo sounding technique is the primary method of monitoring ice sheet thickness and subsurface conditions [9]. It has been applied terrestrially for

monitoring glaciers in Greenland [6] and the scientific community has theorized the technique could also be applied to the Jovian icy moons [9]. Passive sounding has the potential to also serve as a low-resource approach to provide a wide range of temporal and spatial observations of glaciers, ice sheets, and ice shelves [9]. Further improvements to passive radar sounding techniques, systems, and signal property databases (waveform, power, source, location, or transmission event, etc.) are required for widespread implementations [9]. One consequence of the incomplete knowledge and control of ambient signals results in reduced SNR and degraded resolution when compared to an active radar [9]. Peters et al. [6] used the Sun's radio waves for remote sensing of glaciers and encountered several challenges as the Sun is only available half the year in the polar regions.

The passive approach utilizing radio-astronomical sources works by receiving the direct signal from the source and then recording long enough to obtain the echo [9]. Correlation between the direct signal and reflected echo peak produces data on the echo amplitude and delay which can then be mapped to produce data of the target reflected signal [9].

For passive sounding with radio-astronomical sources, it is assumed the distant source arrives as a plane wave and is received as a reflection from the target to the instrument [9]. For a flat Fresnel zone (zone reflecting energy arriving on Earth's surface within a specific time delay) that increases linearly with altitude, there is no inherent range dependency of the distance of the target to the receiver due to the received plane wave [9]. Therefore, for a flat Fresnel zone, the passive signal does not experience geometric spreading loss as opposed to active radars which do experience spreading loss in an identical scenario [9].

Previous passive SAR focusing techniques worked by using timing and geometric unknowns regarding the source's transmission event and location, deep learning models could also be used to invert and reconstruct the passive SAR image [9]. However, both of these methods assumed coherent, digital, man-made sources in order to work [9]. A technique to increase resolution in the azimuth and SNR is to perform SAR-focusing in the time-domain (via back-projection), enabling better results when mapping the terrain of an

illuminated target location [9]. Peters et al. [9] showed that even with a short integration time, a white noise signal using a SAR focusing technique can recover the geometry of a tested digital elevation model (DEM) [9]. Having argued the potential for the passive SAR focusing technique to improve both the radar's azimuth resolution and SNR, it can be noted that increasing the length of the receiving window would improve the passive SAR results. Increasing the length of the receiving signal would result in a greater data volume requiring processing at increased computational expense [9].

A system designed for passive sounding would therefore have several key differences to provide improvements to its performance [9]. Peters et al. [9] suggest the data volume requirement would be drastically decreased if a field-programmable gate array (FPGA) was used to conduct real-time, on-board processing of the data before storing the final processed result enabling maximum usage of passive SAR focusing integration time and therefore increasing the SNR of the radar [9]. "Using the full integration time, the maximum theoretical SNR for the passive system would be comparable to the active system's SNR, furthermore, a passive sounder can be sensitive to greater bandwidths by using an electrically short antenna" [9]. Increasing the bandwidth would improve the range resolution, however, this would not improve the SNR for a distant target and Peters et al. suggest that "increasing the size of the synthetic aperture of the system would result in improvements in SNR" [9].

Another improvement to passive sounding would be the use of direct signal suppression (DSI) [9]. DSI techniques are common when working with passive radar, and reply on existing algorithms requiring both an observation channel of the actual received signal and a reference channel for DSI mitigation [9]. Spatial coherence of an astronomical source's radio signal could be another possible limiting factor for passive sounding [9].

Peters et al. showed in their 2021 paper that the coherence limitation requirement using the Sun can be met for terrestrial ground-based experiments with small antenna altitudes and larger incidence angles [6]. However, this could present an issue for platforms with greater altitudes than those that are terrestrially based, a question that will need to be answered in later studies [9]. Because the Sun is an extended source, the extent to which the spatial coherence of the Sun limits spacecraft measurements to small incidence angles

or near-zenith positions will be studied later [9]. Jupiter's DAM Io sources have been constrained to less than 400km using a technique known as very-long baseline interferometry (VBLI), however Carr et al. suggest a more refined limit of less than 70km (with some evidence for less than 20km) from their analysis of Io-driven Jovian burst modulation lanes [14]. This provides optimistic conditions for many passive sounding applications.

2. Signal Processing for Radio-Astronomical Sources

Realistic signals will be comprised of emissions created by physical processes and, as a result, have variations in their spectral signatures and may contain phase stability that could produce artifacts in the correlation that resemble echoes [16]. Designers must also take into account thermal instrument noise and uncorrelated noise signals, when designing a system and choosing which signal processing technique to utilize as these additional noise signals will be part of the collected signal, lowering the chance of detecting true echoes in low SNR situations [16]. The creation of these non-echoes impacts the sensitivity to true echoes by reducing the range resolution while simultaneously broadening the correlation peaks [16]. Understanding the severity of these effects while collecting live Jovian bursts is imperative when designing a sounding system and deriving methods to mitigate them is equally important [16].

In 2022, Roberts et al. [16] proposed a method to mitigate these non-echoes using signal truncation to eliminate some of the effects [16]. While it effectively removes artifacts from the correlation, the tradeoff for such a technique comes at the cost of power reduction in the signal [16]. Because some of the targeted echoes can be very faint, this may result in a non-ideal experimental set up. These observed variations in spectral amplitude and phase results in artifacts appearing in a superposition of pairs leading/ lagging the source signal [16]. These artifacts will appear as a broadening of the correlation peaks during short delay period variations, leading to a reduction of the measured range resolution [16]. There are known fast ripple variations that have their own echo-like artifacts, but they are not common within Jovian bursts and will not be discussed further [16].

Roberts et al. suggest that the impact of variation and conditioning can be calculated using metrics from several different correlations of each signal: "1) correlation amplitude at echo delay relative to autocorrelation peak, 2) floor amplitude from far echo delay relative to autocorrelation peak, 3) maximum sidelobe amplitude near the echo delay and 4) full width at half-maximum (FWHM) of the peak at the echo delay" [16]. Because range resolution is determined by bandwidth, observations of increasing bandwidth result in the expected narrowing of correlation peak width [16]. The Roberts et al. analysis indicated there was little to no change in the benefits of conditioning the bandwidth (also expected) [16].

Jovian spectral variation has a very clear impact on echo correlation [16]. The presence of sidelobes with approximately 20%-40% of the echo's amplitude, a percentage significantly higher than the 5%-10% in the broadening of the echo delay at the correlation peak, could result in masking of a series of multiple, closely timed, reflections [16]. However, more than 50% of observed bursts have bandwidths over 6MHz and are at least 3dB above the background [16]. These 6MHz bursts provide opportunities obtaining resolutions better than 50m [16]. An additional 15% of bursts are greater than 9MHz which corresponds to resolutions better than 35m [16]. While the bursts at Jupiter are loud enough to drown out other outside source emissions, GBN, which can be ignored within the Jovian system, becomes more influential farther from the Jovian system (e.g. Mars or Earth) [16]. This influence can be diminished by altering the conditioning process by averaging incoherent spectra and subtracting noise floor offset [16]. This enhances the ability of the system to detect echoes as well as increasing resolution because the SNR drops below one [16]. This technique is particularly useful for sounding in our own Earth-moon system [16]. However, the tradeoff of this averaging technique is a decrease in measurement rate [16]. Increases in spectrographic measurement power on the receiver serves to detect and characterize when bursts are occurring and then applying the approach described earlier [16].

Around 9 MHz, Jupiter's radio emissions share both HOM and DAM components, both of which originate at Jupiter's poles [2]. The proposed idea by Roberts et al. is to use Jovian emissions when properties of the autocorrelation function of the emission is a

function of backscattering geometry and subsurface properties [2]. Earlier modeling assumed Jovian emissions as white noise whereas *in situ* the Jovian emission collection has shown that these bursts possess a far more complex spectrum and this complexity impacts the quality of the collected signal [2]. Roberts et al.'s newly suggested method would include a larger selection of radar parameters, such as, "power, central frequency, bandwidth, as well as the altitude of the instrument, the duration of its listening window, and its antenna pattern" [2]. Simulation of a particular passive signal can be accomplished by choosing a particular amplitude, polarization, or time-dependence and then modeling the external source as a plane wave. [2].

3. Galilean Satellite Applications

In their 2015 paper, Romero-Wolf et al. propose a technique for direct detection of liquid water and possible subsurface oceans in Jovian icy moons: Ice Penetrating Radar (IPR) [17]. A dual-frequency system, IPR can produce high-resolution images for shallow depths (>5km) and characterize ice depth with 100m resolution at depths up to 30km [17]. Positive detection and identification of a subsurface ocean requires a depth sensitivity as high as possible [17]. Frequencies lower than 30MHz have been proposed as an ideal frequency range for this technique; however, surface clutter and absorption of the signal due to the ice require both the usage of lower frequencies, which require a strong transmitter to overcome the loud radio environment of the Jovian system (>40MHz) [17]. The impact of DAM emission structure on the autocorrelation function as compared to a white noise function is currently unknown [17].

Surface and volume clutter produce diffusion effects, reducing the strength of a reflected signal, requiring the use of decametric frequencies for successful sounding of an ocean beneath a thick ice shell [17]. Surface roughness corresponds to topographic features that are smaller or equal to the chosen wavelength while surface clutter refers to features larger than, or equal to, the chosen wavelength [17].

As an example, Europa potentially has an active silicate crust in contact with its (possible) global ocean, which lies below a dynamic ice crust that, in some areas, reaches up to 30-km thick [18]. "The shape and composition of Europa's surface is the result of

multiple geological processes, most of which likely involve both direct and indirect interactions between the ice shell and the subsurface ocean" [18]. In the field of planetary geology, surface chemistry is known to be partially governed by material exchanged with a sub-surface ocean [18]. Observations of the disrupted icy surface suggest "shallow water lenses and brines could reside within the ice crust providing a mechanism for exchange between the surface and shallow subsurface of the ice shell" [18]. It has been argued by experts in a variety of fields that these very signatures of material and energy exchange within a liquid-solid hydrosphere environment make Europa a leading candidate for extraterrestrial life [18]. To assist in this search for extraterrestrial life, IPR has the capability to reach ice several kilometers deep, returning samples of its macro-structure and composition via echo detection [18]. Europa's space environment is dynamic due to its orbit lying both within Jupiter's inner magnetosphere and the outer edge of the Io plasma torus [18]. This results in a charged and magnetized planetary ionosphere, which can cause distortion and attenuation of the signal potentially altering the detection capabilities of the instrument [18].

The use of Jupiter's own emissions as source for IPR sounding, via an interferometric reflectometry technique, could resolve some of the issues of working within Jupiter's loud radio environment [17]. IPR uses the same dipole antenna as the radar system that is in use and requires very low power usage, making it an is an attractive complement to a radar system [17]. By acting as an electrically short dipole, interferometric reflectometry has the potential to increase number of frequency bands available for observation [17]. Currently, GPS uses interferometric reflectometry to measure snow depth [17]. The system modulates the transmitted GPS signal, as well as its subsurface reflection SNR, by using a sinusoidal wave with a frequency directly proportional to snow depth [17].

Non-Io sources are solely dependent on the rotational phase of Jupiter and occur varying duty cycles [17]. "Non-Io-A, near CML III of 270°, is not the strongest source but has a 100% duty cycle" [17]. "Non-Io-B, located at a CML of 90–180°, has a duty cycle of approximately 40%" [17]. The strongest source, known as Io-B as it occurs as an interaction between Io and a Non-Io-B source, occurs when "Io is at a 90 phase relative to the observer and the CML III of Jupiter is 90–180°" [17]. An active Io-A source has also

been observed at the Non-Io-A longitude when Io is at a 240° of orbital phase [17]. All the sources have varying time scales of seconds to minutes at an amplitude of 20dB [17]. These are the previously discussed L bursts [12], [17]. Io sources all produce stronger bursts than the non-Io source and VBLI observations [14] indicate L-bursts are generated in a region less than 400km in diameter and this highly localized, and predicable, source characteristic and temporal structure makes L-bursts an attractive signal for passive radar detection [17].

4. Passive Sounding Considerations to Thesis

Regardless of origin, passive radar users have no control over an ambient source's characteristics or predictability. Peters et al. demonstrated that it was possible to receive the direct path of the astronomical noise source and receive the reflected path from a possible material boundary [9]. By relating the emitted signal with the reflected one it is possible to calculate the white noise echo's amplitude and time [9]. Correlation between the delay time between direct and reflected echo peaks can then be mapped to an estimate of the ice thickness [9]. In the case of remote sensing of a glacier, that delay time between direct and reflected echo peaks then maps to an ice thickness estimate [9]. Peters et al. also suggested using a FPGA for rea-time onboard processing to reduce the data volume [9]. This in turn would enable the system to increase the radar's SNR by ensuring that the maximum focus integration time was used [9]. In using the full integration time, the SNR for the passive system would equal an active system's SNR and further frequency sensitivity could be added with the use of a short electrical antenna [9]. Improved range resolution can be achieved by increasing the bandwidth and would suppress the main and side lobes in the autocorrelation [9]. However, the use of these techniques would not improve a distant target's SNR [9].

The extent of a source's spatial coherence, however, could be a potential limiting factor [9]. While Peters et al. met coherence limitation requirements using the Sun for terrestrial ground-based experiments, high altitude platform sensors could be impacted by spatial coherence limitations [9].

The strongest observed DAM burst are driven by interactions with its moon Io [16]. While initial measurements of Jupiter DAM Io sources constrained the sizes to less than

400km (utilizing VBLI), a narrower limit of 20km-70km has been suggested by Roberts et al.[16]. Additionally, Roberts et al. suggest that the impact of variation and conditioning can be calculated using metrics from several different correlations of each signal: "1) correlation amplitude at echo delay relative to autocorrelation peak, 2) floor amplitude from far echo delay relative to autocorrelation peak, 3) maximum sidelobe amplitude near the echo delay and 4) full width at half-maximum (FWHM) of the peak at the echo delay" [16]. Because range resolution is determined by bandwidth, observations of increasing bandwidth result in the expected narrowing of correlation peak width [16]. Roberts et al.'s analysis indicated there was little to no change in the benefits of conditioning the bandwidth (also expected) [16].

Jovian spectral variation has a clear impact on observed echoes [16]. The correlation maximum at the delay increased by 5%-10% on average. However it is increase of 20%-40% of sidelobe amplitude of the echo that could potentially mask, multiple, closely spaced reflections [16]. More than 50% of available bursts have a bandwidth of at least 6MHz at are 3dB above the background noise which provides ample opportunity for soundings with resolutions better than 50m. An additional 15% of bursts are wider than 9MHz, which gives greater than 35m resolution [16].

Non-Io sources are solely dependent on the rotational phase of Jupiter and occur varying duty cycles [17]. "Non-Io-A, near CML III of 270°, is not the strongest source but has a 100% duty cycle" [17]. "Non-Io-B, located at a CML of 90–180°, has a duty cycle of approximately 40%" [17]. The strongest source, known as Io-B as it occurs as an interaction between Io and a Non-Io-B source, occurs when "Io is at a 90°phase relative to the observer and the CML III of Jupiter is 90–180°" [17]. An active Io-A source has also been observed at the Non-Io-A longitude when Io is at a 240° of orbital phase [17]. All the sources have varying time scales of seconds to minutes at an amplitude of 20dB [17]. These are the previously discussed L bursts [12], [17]. Io sources all produce stronger bursts than the non-Io source and VBLI observations [14] indicate L-bursts are generated in a region less than 400km in diameter and this highly localized, and predicable, source characteristic and temporal structure makes L-bursts an attractive signal for passive radar detection [17].

THIS PAGE INTENTIONALLY LEFT BLANK

III. SOURCE SPATIAL COHERENCE AND CHARACTERISTICS

A modified version of this section was published as:

A modified version of this section was submitted to and under review as:

Peters, Sean, Nessly, Karissa, Roberts, Maximillian, Schroeder, Dustin, and Romero-Wolf, Andrew, "Spatial Coherence Constraints on Passive Sounding with Radio-Astronomical Sources," IEEE Transactions on Geoscience and Remote Sensing, In Review, 2022.

Previous work [6] developed a passive sounding signal model using a plane wave assumption for the source by treating the wavefront of the radio noise as planar and constant when incident on both the radar and the target. Here, we develop a new model for the signal autocorrelation function generalizing this problem to consider the intensity distribution of a random source by including the coherence function (derived with the help of the Van Cittert–Zernike (VCZ theorem). Within the coherence theory (the study of optical effects from radio sources and partially coherent light) the VCZ theorem states that the Fourier transform of the intensity distribution of an incoherent source is an indicator of its complex visibility (within certain conditions).

The VCZ theorem states the mutual coherence function is given by:

$$\Gamma_{12}(u, v, 0) = \iint_{src} I(l, m) e^{-2\pi i(ul+vm)} dldm$$

where I(l,m) is the intensity distribution of the source, (l,m) are the direction cosines defined with respect to the (x, y) axes in the measurement plane, and u and v are the x and

y components of the spacing between the two points measured in wavelengths (i.e., the spatial frequencies).

While similar in the sense of receiving an extended source, the passive sounding problem is not one of imaging sources in the u, v plane but rather one that leverages the correlation function for echo detection. This is, however, perfectly equivalent to the VCZ theorem by taking a few steps back in its derivation, as the phase term in the derivation arises from the path length difference relation: R1 − R2 = (ul + vm)c/ν, where R1 is the distance between the source and the first received path, R2 is the distance between the source and a second received path, and ν (nu) is the temporal frequency. We again note that in the case of passive sounding, there is a single receiver and R1 − R2 becomes the path length difference between the direct and reflected signals. We also go back to the definitions of u and v to make it pertinent to the passive sounding problem. The definitions are u = (x1 − x2)ν/c and v = (y1 − y2)ν/c. The path length difference then becomes R1 −R2 = (x1 −x2)l+(y1 −y2)m. However, if we instead express the mutual coherence function in terms of the delay Δt(l,m) = (R1−R2)/c, we can remove the spatial frequencies terms. The mutual coherence function then becomes

$$\Gamma_{12}(R_1 - R_2, v, 0) = \iint_{arc} I(l,m)\, e^{-2\pi i v \Delta t(l,m)} dl dm.$$

We note that the arguments of the equation above are the path length difference and temporal frequency (ν), rather than the spatial frequencies (u, v) using the relations given above. The cross correlation, as a function of delay, is therefore the Fourier transform of the mutual coherence function:

$$\mathrm{C}(\tau) = \int e^{2\pi i v \tau}\, \Gamma_{12}(R_1 - R_2, v, 0) dv.$$

This modified version of the VCZ theorem thus considers the geometry of the source size (e.g., the Sun disk) and will be used for the simulations in Section IV-C, which considers a random distribution of emitters than span the extent of the Sun to analyze the spatial coherence effects on the autocorrelation.

There are bounds to the applicability of passive sounding as set by the angular source extent. If the source is sufficiently extended, incoherent contributions from multiple source regions could interfere and potentially reduce the strength of the echo peak in the correlation-based technique. In addition to considering the extended source size for the Sun and Jovian bursts, we derive the spatial coherence constraints in terms of altitude, wavelength, and incidence angle. We start by demonstrating the passive sounding technique fulfills the Fraunhofer criterion for the case of a distant, radio- astronomical source.

If the source is sufficiently extended, incoherent contributions from multiple source regions could interfere and potentially reduce the strength of the echo peak in the correlation-based technique. In addition to considering the extended source size for the Sun and Jovian bursts, we derive the spatial coherence constraints in terms of altitude, wavelength, and incidence angle. We start by demonstrating the passive sounding technique fulfills the Fraunhofer criterion for the case of a distant, radioastronomical source. If one assumes that a ≪ d (which is the general case for passive sounding using distant, compact radio-astronomical sources), then the difference in propagation path lengths OA and OB above can be neglected. Following the Fraunhofer criterion, we find that

$$k(OB - OA) \approx k\frac{a^2}{2d} = \frac{ka}{2}\delta\theta \ll 1,$$

where k is the angular wavenumber, a is the size of the source, d is the distance from the source to the target, and the source angular extent is δθ = a/d. In this sense, the source becomes a "point source," as the spread of the source points between A and B can be ignored, and one can therefore assume that the source collapsed into a point A. However, one must also consider the interference between the direct and surface/subsurface reflected signals received by a passive sounder. Again, the path length difference between the direct and reflected signals (L) is given by L = 2h cos(θ). If the source angular extent is δθ, then the associated path length variation is dL = 2hδθ sin(θ) [22]. The spatial coherence

requirement of $dL < \lambda$ thus results in a maximum altitude limit for passive sounding using extended radio-astronomical sources

$$h < \frac{\lambda}{2\delta\theta \sin(\theta)} = \frac{\lambda \cdot d}{2 \cdot a \cdot \sin(\theta)},$$

where λ is the wavelength of the radio emission. We consider two brief examples using radio emissions from the Sun and Jupiter measured at the Earth and Europa respectively, which is a subset of analysis that could be applied to any planetary passive sounding experiment. The source angular extent of the Sun as seen from the Earth is approximately $\delta\theta_{S,T} = 10^{-2}$ rad when assuming the source of the radio emissions originates across the full Sun disk in the most incoherent case (i.e., a Sun diameter of 1.39×10^6 km and a distance to the Sun of 1.5×10^8 km). In the case of Jupiter's radio emissions, assuming the spatial extent for the Jovian bursts is constrained to 70 km and the distance from Jupiter to Europa is roughly 7×10^5 km, the source angular extent as seen from Europa is $\delta\theta_{J,E} = 10^{-4}$ rad. Rewriting Eq. 13 to highlight the respective source size over the radio wavelengths of interest, the maximum altitudes for a passive radar (1) using the Sun to perform sounding terrestrially and (2) Jupiter's radio emissions to perform passive sounding at Europa are, respectively:

$$h_{S,T} < \left(\frac{5\ km}{sin\theta}\right)\left(\frac{1.39 \cdot 10^6\ km}{a}\right)\left(\frac{\lambda}{100\ m}\right)$$

and

$$h_{J.E} < \left(\frac{500\ km}{sin\theta}\right)\left(\frac{70\ km}{a}\right)\left(\frac{\lambda}{100\ m}\right)$$

where a is the spatial extent of the source in km. These bounds should be considered in the experiment design to establish the maximum sounding altitude for a passive radar remote sensing mission. We note that these limits serve as the conservative case for the coherence requirement, as previous work has shown that although the intensity pattern decays with increasing path length difference, the echo peak in the autocorrelation did not experience

this path difference limitation. The spatial coherence limitations for using Jovian bursts as a source for echo detection are illustrated in Figure 2. The top line of figures shows the maximum altitude using the limitations as a function of the wavelength, bistatic angle, and the angular size of the source for three different locations: Earth, Mars, and Europa. The Jovian burst source extent utilized for this scenario was 70km. The numbers on the contour lines for the top row figures indicate the power of 10 for the maximum altitude (in km). For direct comparison, the bottom row depicts the pulse broadening using Jovian bursts as a function of bistatic angle and altitude for the Earth, Mars, and Europa. The numbers on the contour lines for the bottom row figures indicate the number of samples broadened (delay smear) in the autocorrelation.

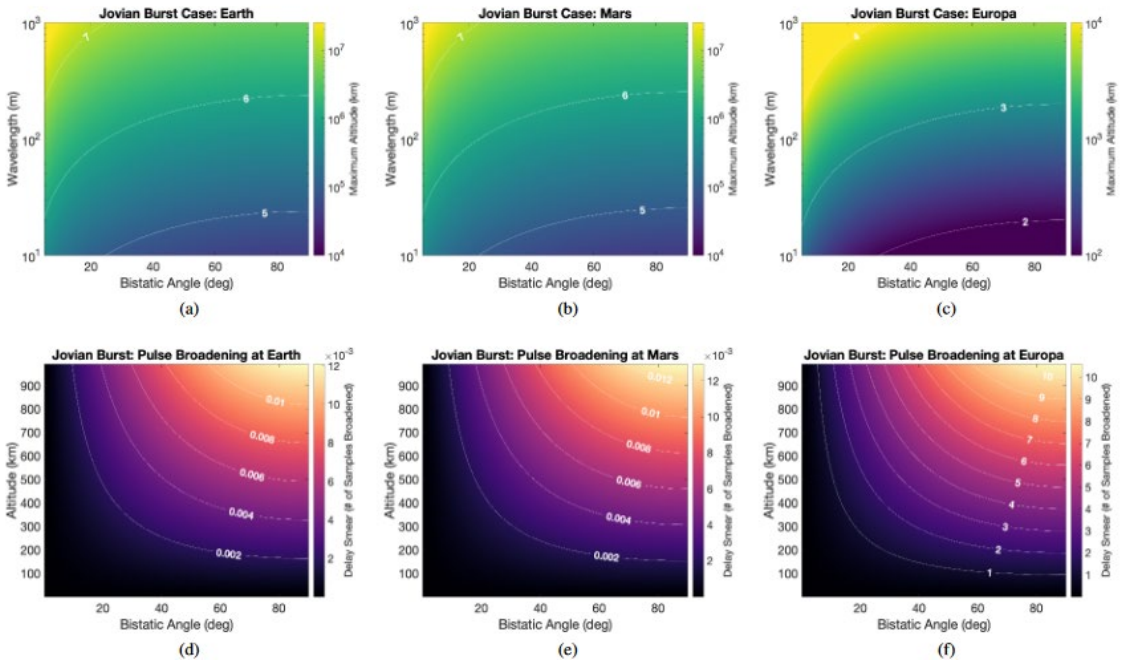

The top row shows the maximum altitude using the limitations as a function of the wavelength, bistatic angle, and the angular size of the source (where a 70 km spatial extent is used for Jupiter's radio emissions for 3 passive sounding scenarios (columns): on Earth $\delta\theta_{J,T} \sim 6.8 \times 10^{-6}$◦ (left, a), Mars $\delta\theta_{J,M} \sim 7.3 \times 10^{-6}$◦ (middle, b),and Europa $\delta\theta_{J,E} \sim 0.034$◦(right, c). The numbers on the contour lines for the top row figures indicate the power of 10 for the maximum altitude (in km). For direct comparison, the bottom row depicts the pulse broadening using Jovian bursts (which also depends on the angular size of the source) as a function of bistatic angle and altitude for the 3 passive sounding targets of interest at Earth (3d), Mars (3e), and Europa (3f). The numbers on the contour lines for the bottom row figures indicate the number of samples broadened (delay smear) in the autocorrelation.

Figure 2. Spatial Coherence Constraints Using Jovian Bursts as the Source for Echo Detection. Source: [5].

IV. EXPERIMENTAL DESIGN AND SYSTEM MODELING RESULTS

A. INFORMING TERRESTRIAL PASSIVE RADAR EXPERIMENTAL DESIGN USING JUPITER'S RADIO EMISSIONS FOR ECHO DETECTION

A modified version of this section was submitted as:

K. Nessly, "Informing Terrestrial Passive Radar Experimental Design Using Jupiter's Radio Emissions for Echo Detection," presented at the AGU Fall Meeting 2022, Chicago IL, Chicago IL, Dec. 14, 2022.

There is ongoing interest in the theoretical performance of a passive radar using Jupiter's decametric radio emissions as a source for passive Synthetic Aperture Radar (SAR) imaging of Jupiter's icy moons and terrestrial glacial monitoring. Experiments utilizing the Sun's radio emissions have shown it can be used as a passive radar source to measure terrestrial ice thickness. However, there has been no work performing an in-situ demonstration using Jupiter's decametric radio bursts as a source for passive radar sensing. Several questions need to be answered regarding Jupiter's spatial usability, its temporal availability, and its frequency usability.

One of the important characteristics of Jupiter's decametric radiation is it is driven by interactions between Jupiter's magnetosphere and the Io torus. Figure 3, generated by Radio Jupiter Pro Software [19], is a prediction of the probability of Io-driven decametric bursts on a specific day as well as a prediction of when the Sun and Jupiter will both be above the Earth's horizon at a specific location (Monterey, CA, for this example) on a specific day. In the figure on the left, we can see Io-A and Io-B (refer to II.C.4) have a high probability of occurrence, while Io-C has a lower probability of occurrence. The dashed diagonal lines across the graph indicate the time of day and the light blue line indicates that Jupiter is below the horizon at this specific location while the white line indicates that Jupiter is about the horizon. The righthand figure is a year-long guide to when Jupiter and the Sun will be above or below Earth's horizon at a specific location (Monterey, CA, for this example). White indicates that neither the Sun nor Jupiter is above the horizon. The

yellow bar is indicative of the Sun above the horizon while the blue bar indicates when Jupiter is above the horizon. The green segments, where the blue and yellow intersect, show when both Jupiter and the Sun are above the horizon. Knowing when the Sun is above Earth's horizon at the same time as Jupiter is important to terrestrial sounding missions as the radio signals from the Sun are the loudest in the solar system and introduce interference into the environment.

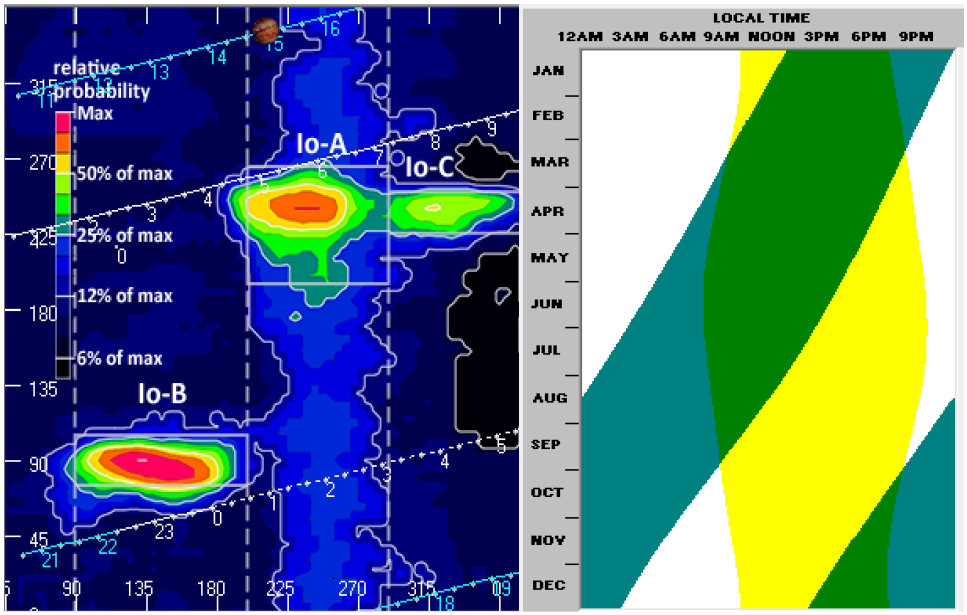

The image on the left shows a prediction of the probability of a DAM burst occurring on a specific day. The image on the right shows a prediction of the availability of both Jupiter and the Sun above the horizon. The Sun is a significant source of noise and creates interference when gathering burst data.

Figure 3. Prediction of Probability of a DAM Burst Occurring and a Prediction of Jupiter's Availability above the Horizon

Figure 4 includes four graphs that were generated using Radio-Jove Pro Software for summer and winter solstice of 2022 at four different locations around the world: Dante's View, Death Valley, CA, Big Sur, California, Store Glacier, Greenland, and McMurdo Station, Antarctica. The key locations to note are Store Glacier, Greenland and McMurdo Station, Antarctica. Radio-Astronomical sourcing using the Sun in these extreme latitudes can be difficult due to the long periods when the Sun is below the horizon

during the respective winter and summer seasons. During the summer solstice at McMurdo Station, the Sun remains below the local horizon for the entire day. However, Jupiter has periods where it is above the horizon and therefore provides an opportunity for remote sounding using Jovian bursts. Store Glacier, Greenland has an identical situation, only during the winter solstice vice the summer solstice. With the addition of Jupiter as a usable radio-astronomical source, observations undertaken at the more extreme latitudes have the potential to continue for additional time periods compared to when only the Sun is utilized as a source.

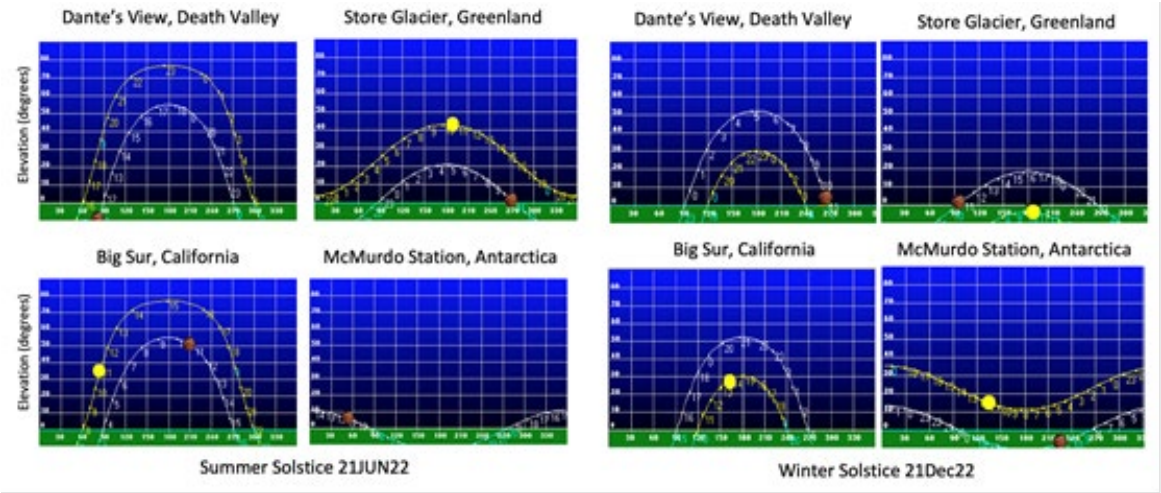

Figure 4. Elevation Angles for the Sun and Jupiter for Four Locations During Summer and Winter Solstice of 2022

The impact of source size on expected results were modeled utilizing code developed by Peters et al. [20], to calculate the pulse broadening as a factor of incidence angle and elevation angle. Figure 5 shows even in the extreme case of an extended source size of approximately 70,000km, the spatial coherence of the signal was well below the threshold for a chosen 30MHz pulse width. The purple line correlates to approximately 70,000 km which is the diameter of Jupiter and represents an extended source size. The yellow, 400 km, red, 70 km, and blue 20 km, source sizes were chosen correspond to the analysis done by Roberts et al. [16] (refer to II.C.2). Because the pulse broadening for both

cases (elevation angle and incidence angle) were below the chosen 30MHz pulse width, we can conclude that pulse broadening is not a concern.

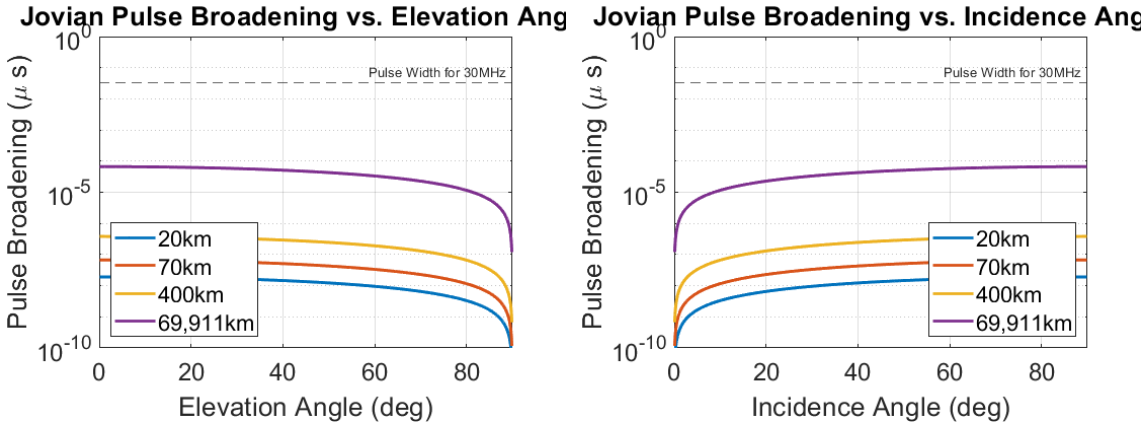

Jovian Pulse Broadening vs. Elevation Angle (Left) and Jovian Pulse Broadening vs. Incidence Angle (Right). Each of the colored lines indicates a point source size, from 20km, to 69,911 km, Jupiter's diameter, effectively making it an extended source. Refer to Appendix A for MATLAB code.

Figure 5. Jovian Pulse Broadening vs. Elevation Angle. Jovian Pulse Broadening vs. Incidence Angle

To carry the analysis forward, we applied the same criteria to our two test locations: Big Sur, CA and Dante's View, Death Valley. Using the same code developed by Peters et al., we modeled pulse broadening vs. elevation angle and pulse broadening vs. incidence angle for Big Sur (figure 6) as well as for Dante's View (Figure 7). Here we can see that the pulse broadening, regardless of location, elevation angle, or incidence angle are well below our modeled 10MHz pulse width cutoff for elevation and our 30MHz cutoff for incidence angle.

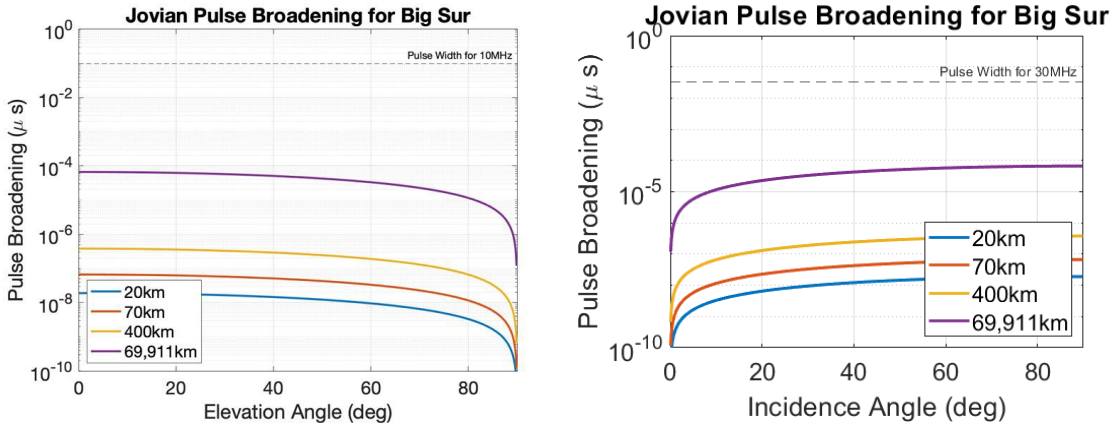

Jovian Pulse Broadening vs. Elevation Angle (Left) and Jovian Pulse Broadening vs. Incidence Angle (Right). The results of Figure 6 show, regardless of show that regardless of source size, pulse broadening at Big Sur is well below the limitation of a 10MHz bandwidth regarding elevation angle is well below a 30MHz bandwidth with regard to incidence angle. Refer to Appendix B for MATLAB code.

Figure 6. Jovian Pulse Broadening vs. Elevation Angle for Big Sur. Jovian Pulse Broadening vs. Incidence Angle for Big Sur

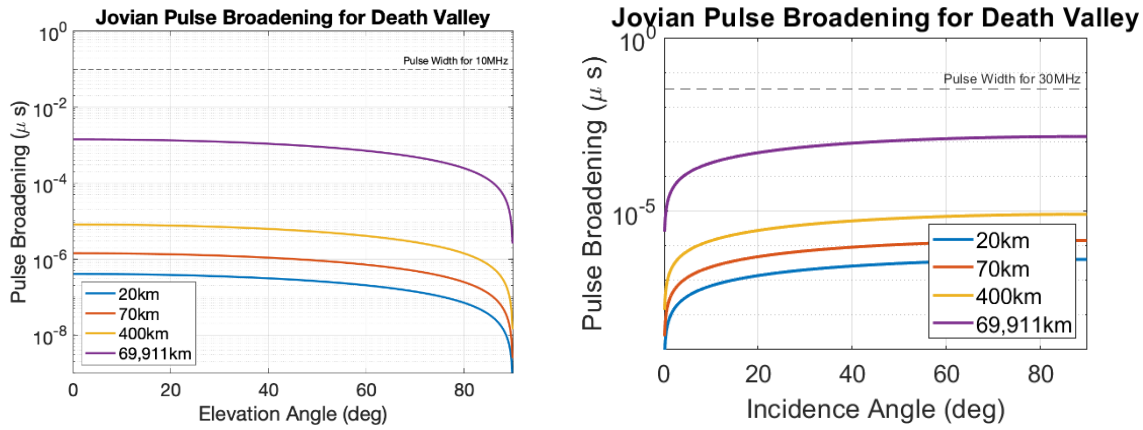

Jovian Pulse Broadening vs. Elevation Angle (Left) and Jovian Pulse Broadening vs. Incidence Angle (Right). The results of Figure 7 show, regardless of show that regardless of source size, pulse broadening at Death Valley is well below the limitation of a 10MHz bandwidth regarding elevation angle is well below a 30MHz bandwidth with regard to incidence angle. Refer to Appendix B for MATLAB code.

Figure 7. Jovian Pulse Broadening for Big Sur vs. Elevation Angle. Jovian Pulse Broadening for Big Sur vs. Elevation Angle

Analysis of Fresnel reflection losses, utilizing code developed by Peters et al. [9], showed Death Valley (rough, desert terrain) had greater losses than Big Sur (specular reflection). Comparing the results in Figure 8 showing Big Sur and Death Valley

respectively, we can see that the S (horizontal) polarization losses (-2dB) are significantly smaller than those of Death Valley's S polarization losses, -6dB. The P polarization (vertical polarization) losses for both Big Sur and Death Valley are significant for most elevation angles, before recovering and matching the S polarization losses at approximately 75° at Big Sur and at 85° at Death Valley. Additionally, the losses at Death Valley did not take account for additional scattering losses, which would only increase the total amount of signal loss for a non-specular reflection scenario. From both figures we can conclude that S polarization provides the least amount of reflection losses and that a specular reflection retains the least amount of loss compared to a rougher, desert-type terrain. Passive sounding using radio-astronomical sources relies on capturing the reflections of the source signal. If the source has a weak signal, then utilizing a specular reflection may increase the odds of capturing the echo.

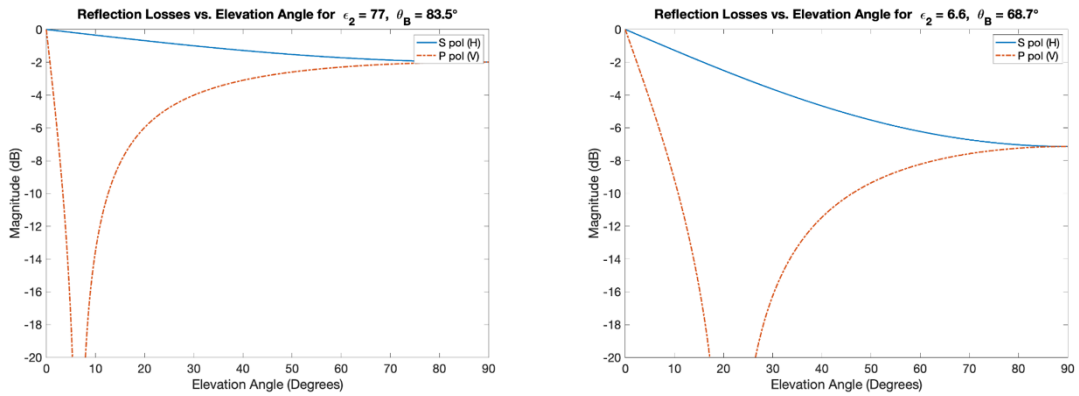

Figure 8. Reflection Losses vs. Elevation Angle for Big Sur and Reflection Losses vs. Elevation Angle for Death Valley

In addition to the reflection losses, we also considered the expected echo delay time for Big Sur and Death Valley (Figure 9). Because Death Valley cliff has a greater height, this increases the range of usable elevation angles. The dashed line shows the width of the main lobe in the autocorrelation function, which impacts our resolvability. Here a conservative, simulated, 10 MHz bandwidth is used. Anything below the dashed line we cannot resolve, and as we can see from Figure 13, Death Valley would be a more optimal experimental location as it has a higher elevation, and that higher elevation increases the

range of usable elevation angles for our simulated 10MHz bandwidth. Side lobes were not included in this evaluation but would need to be considered in follow-on analysis.

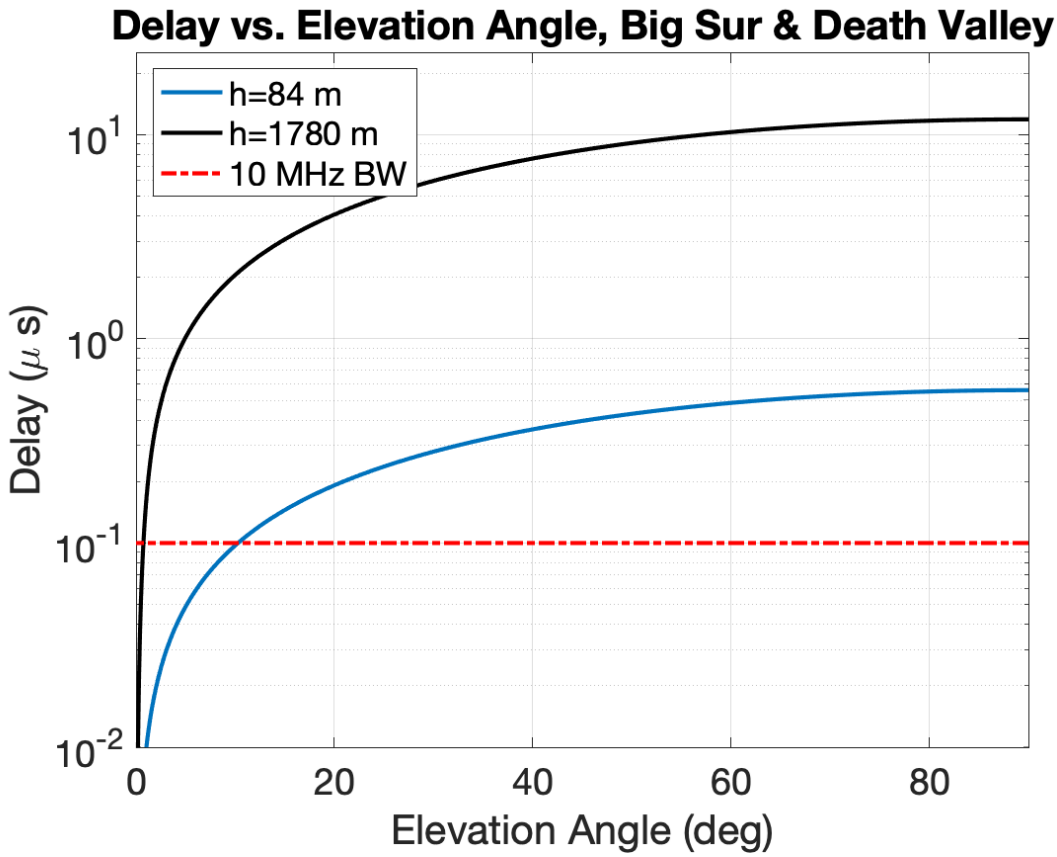

Figure 9. Comparison of Delay vs. Elevation Angle for Big Sur and Death Valley

Figure 10 models the delay as a function of elevation angle, but also includes altitude. The contour shading illustrates that a low elevation angle allows for a range of sensor altitudes that correspond to the lowest delay (approximately 0.1μs) whereas a high sensor altitude results in a more significant delay as the elevation angle increases (up to 0.6 μs at a 65° elevation angle at a sensor height of 100 m).

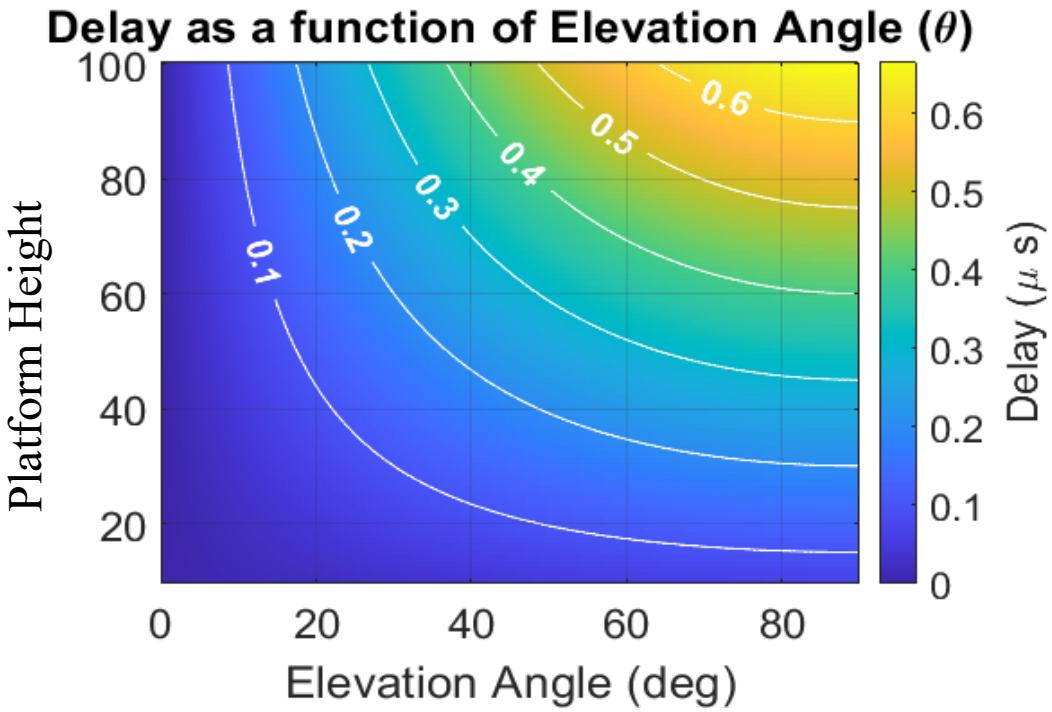

Figure 10. Delay as a Function of Elevation Angle and Platform Height

B. SYSTEM PARAMETER CONSTRAINTS ON TERRESTRIAL PASSIVE RADAR SOUNDING USING JOVIAN DECAMETRIC RADIATION.

A modified version of this section was submitted as:

Karissa Nessly, Sean Peters, Gregor Steinbrugge, Dustin Schroeder, and Andrew Romero-Wolf, "System Parameter Constraints On Terrestrial Passive Radar Sounding Using Jovian Decametric Radiation," IEEE Geoscience and Remote Sensing Society, Accepted 2023.

The temporal availability of Jupiter relies on three factors: 1) When is Jupiter above the horizon 2) When are both the Sun and Jupiter above the horizon and 3) What is the probability of an Io-driven burst occurring? The first question can readily be answered by several programs currently available that calculate when Jupiter is above the horizon for specific dates and locations. The addition of the Sun's radio energy must be considered when both are above the horizon, as its radio emissions are strong enough to introduce significant noise in the environment that may impact observations. Radio-Jupiter Pro software was used to obtain information for both the Sun and Jupiter's time above the

horizon and was able to show throughout the entire year Jupiter maintained usability, even at McMurdo Station and Store Glacier (See Figure 5). One of the key characteristics of Jupiter's decametric radiation is that it is driven by interactions between Jupiter's magnetosphere and the Io torus which, in turn, is driven by volcanic activity on Io. To date, it is difficult to predict volcanism on Io, therefore estimated probabilities of Io-driven radio bursts need to be studied in greater detail and over a significant period, preferably over several orbits of Jupiter around the Sun (a cycle takes approximately 12 Earth years).

To calculate Jupiter's radiometric usability, we needed to determine the foF2 frequency of the ionosphere. The foF2 frequency is also known as the critical frequency and is related to the electron density in the ionosphere and dictates the highest radio frequency that can be reflected back to Earth. We modeled the foF2 frequency using International Reference Ionosphere 2020 InstantRun [21] data (refer to Appendices B-E) and the results showed that the critical frequency of Earth's ionosphere varied both seasonally and diurnally, with a particularly noticeable trend of the variations occurring approximately in conjunction with the change of the seasons (Figure 11). Knowing Jupiter's upper cutoff frequency for DAM radiation is 40MHz, the calculated minimum foF2 frequencies was used for each location and time to calculate a best-case bandwidth range. Once again utilizing the International Reference Ionosphere 2020 InstantRun [21] software, we sampled critical frequencies from January to December 2022 and used the data (refer to Appendices B-E) to generate Figure 11 in MATLAB to compare the radiometric usability not only during the day, but also at night for the same four locations discussed earlier. The image on the left shows the predicted critical frequency for each day of the year at 0000 (midnight) while the image on the right shows the predicted foF2 frequency for each day of the year at 1200. There is very clearly a dip in the foF2 value during the day in the summer months while there is an increase in the foF2 for the same period at night.

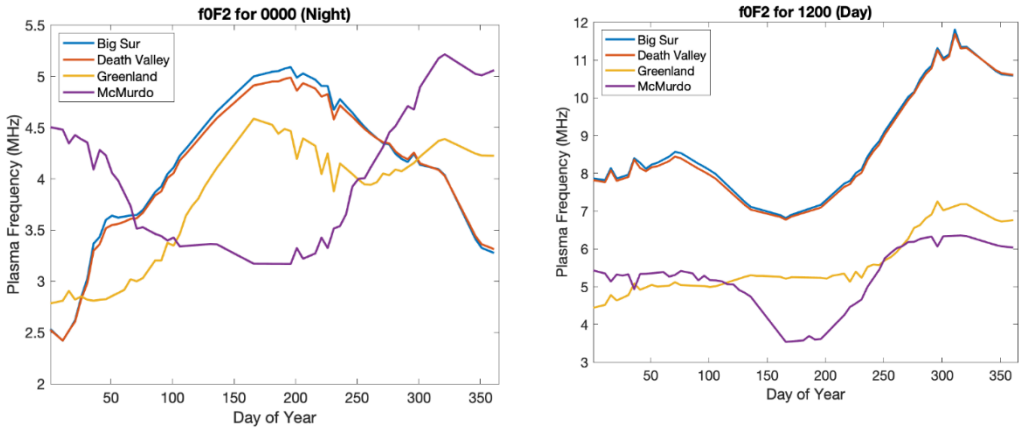

foF2 Ionosphere Plasma Frequency for Big Sur, Death Valley, Store Glacier Greenland, and McMurdo Station, Antarctica for night (Left) and day (Right). Refer to Appendices B-E for full IRI2020 data sets.

Figure 11. foF2 Ionosphere Plasma Frequency for Big Sur, Death Valley, Store Glacier Greenland, and McMurdo Station, Antarctica

Taking the analysis further, we modeled the expected range resolutions by utilizing the known DAM ionospheric cutoff at 40MHz and the critical frequencies discovered earlier (refer to Figure 11). As part of our analysis, we chose angles of 50°, 20°, and 10° to correspond to a maximum elevation angle, a low elevation angle, and a near-worst case angle scenario. These cases were then modeled for two times of the day, midnight, and noon. The results are shown in Figure 12.

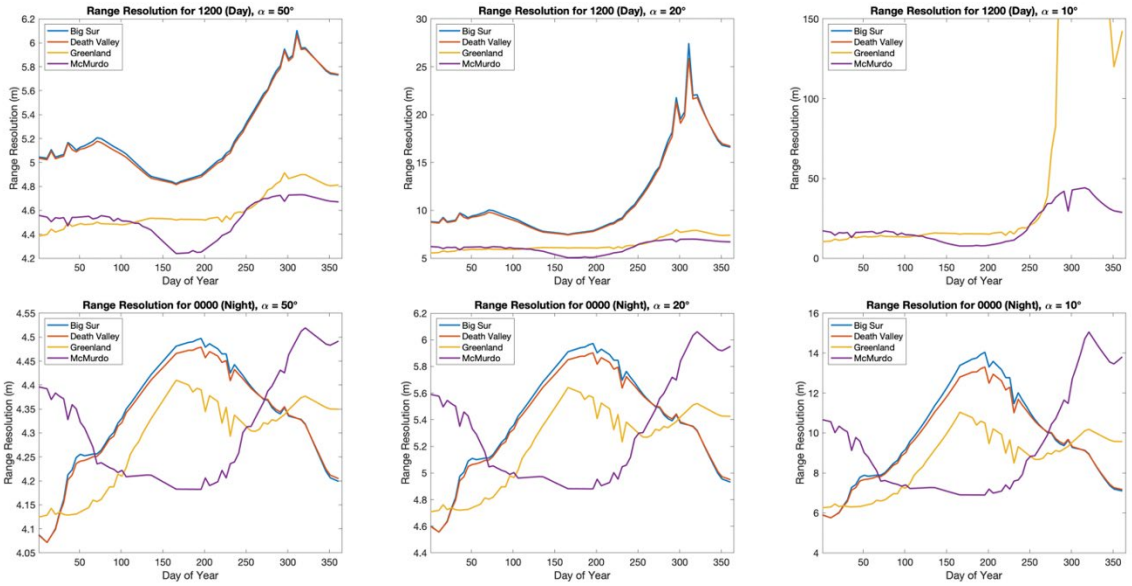

Using the IRI 2020 Model for four locations three cases were considered: maximum elevation angle (left) 50°, (middle) 20°, and (right) 10° for two times of day (top) 1200 and (bottom) 0000 local time PST. Note the y-axis limits, especially for the 10° case as the maximum y limit shows the range resolution of 150MHz corresponding to a 1 MHz bandwidth. Refer Appendices B-E for full IRI2020 data sets.

Figure 12. Derived Range Resolution

Peters et al. [6], [20] has shown the maximum and minimum angles of Jupiter's elevation can be larger (over 80° at +/- 30° latitude) however, this occurs over Jupiter's entire orbital period and a conservative maximum of 50° degrees was selected to match the results of Radio-Jupiter software for Summer and Winter solstice of 2022. The same selection criteria were applied for the 20° and 10° choices. Our analysis, refer back to Figure 12, showed the best range resolution for all four locations would be obtained at night with a Jupiter elevation angle of 50° (4.05m -4.5m), whereas a 10° degree elevation angle at noon produced the worst results for Store Glacier, Death Valley, and Big Sur. Death Valley and Big Sur results were above the 1 MHz bandwidth cutoff for the entire year while Store Glacier results returned acceptable range resolutions for only two-thirds of the year.

THIS PAGE INTENTIONALLY LEFT BLANK

V. CONCLUSIONS AND FUTURE WORK

A. SUMMARY OF RESULTS

The purpose of this study was to consider the question of whether Jupiter's radio emissions could be used as a source to study passive radar. We evaluated three criteria: 1) Jupiter's temporal usability, 2) Jupiter's frequency usability, and 3) Jupiter's spatial coherence.

Analysis of Fresnel reflection losses showed Death Valley (rough, desert terrain) had greater losses than Big Sur (specular reflection). The losses at Death Valley did not take account for additional scattering losses, which would only increase the total amount of signal loss. Modeling also showed in both cases H-polarization was the better choice. Expected echo delay times for Big Sur and Death Valley were also modeled; Dante's Peak is located at a higher altitude, increasing the range of usable elevation angles for a simulated 10MHz bandwidth. Lastly, even in the extreme case of an extended source size of approximately 70,000km the spatial coherence of the signal was well below the threshold for a 10MHz pulse width.

The results showed Jupiter has a temporal availability year-round, even at the poles. Jupiter's radio emissions may be limited, but they are still available and experimental planning requiring the use of these signals may be undertaken. Analysis showed a drop in the foF2 during the day in the summer months with a corresponding increase in the foF2 for the same period at night. Since the cutoff frequency for Jupiter's DAM radio emissions is 40MHz, and the foF2 variations throughout the day and night can be predicted, the usable bandwidth of Jupiter's emissions for experimental design can be computed. Building on this knowledge, maximum and minimum angles of Jupiter's elevation were chosen to compute the best range resolution and our analysis showed the best range resolution for all four locations would be obtained at night with a Jupiter elevation angle of 50° (4.05m -4.5m), whereas a 10° degree elevation angle at noon produced the worst results for Store Glacier, Death Valley, and Big Sur. Death Valley and Big Sur results were above the 1 MHz bandwidth cutoff for the entire year while Store Glacier results returned acceptable range resolutions for only two-thirds of the year.

B. FUTURE WORK

The passive technique demonstrated here for the first time shows radar echo detection using radio emissions from Jupiter is possible. Another use for this technique would be to utilize varying slant angles to probe the ionosphere [22]. This would allow for a reconstruction of the ionosphere tomography, allowing researchers to better answer the question of how changing tomography impacts the detected signal and if there are cases when passive ionospheric tomography is practical in further studies [22].

This research did not discuss implementing active HF and VHF radar designs nor did it discuss the theory that both active and passive HF radar measurements could be undertaken simultaneously, provided of course the system is designed to generate the passive measurement between the active signal measurements [22]. Theoretically, VHF and HF active measurements could be active with the degraded HF signal removed [22]. Once the degraded signal has been eliminated, autocorrelation techniques can be performed on the received Jovian noise data [22].

Throughout this research, we have conducted system modeling. The next step would be to implement the software and hardware component of the experiment *in situ*. Successful demonstration of passive radar echo detection using Jupiter's radio emissions, collected in two separate environments, would allow for follow-on testing and experiments. The full capability and limitations of this technique would need to be identified prior to it being deployed to a fleet or the DOD as a whole. If the technique is effective, it could allow military and DOD users to capitalize on ambient radio signals of opportunity as source for passive radar, reduce spectrum overcrowding, and provide long-term observations of current and evolving threats in complex environments. Additionally, as a passive radar does not, itself, radiate, it has the potential to also be used in situations where an active radar would not be ideal. Currently, the technique holds more immediate promise for glacial and environmental monitoring on a global scale. Given the state of global warming, the ability to continually monitor ice packs, glaciers, and sea level would prove invaluable to the U.S. Navy as sea levels begin to rise and threaten bases and shipyards around the globe.

APPENDIX A. MATLAB MODELING CODES

A. CODE FOR ESTIMATING PULSE BROADENING

```
clear all
close all

set(0,'defaultAxesFontsize',18)
set(0,'defaultLineLineWidth',2);


h = 84;  % in meters
theta = 0.1:.1:89.9;  % length 401 % theta is the bistatic angle
c = 2.998*10^8; % m/s

% (1) could do a for loop over source sizes of 20km, 400km, and 69,911 km
%J_source_extent = 70; %~km Jupiter source extent in km. (400km) see K. Imai, L. Wang,
and T. D. Can, "Modeling Jupiter%s decametric modulation lanes,

J_source_extent_list = [20, 70, 400, 69911];
%J_source_extent_list = 70;

for ii = 1:length(J_source_extent_list)
    J_source_extent = J_source_extent_list(ii);

    d_EarthJmin = 588e6; %~km Jupiter to Earth (588 million kilometers) at their closest
point (https://www.space.com/18383-how-far-away-is-jupiter.html)

    % ang_ext_Jupiter_Earth_deg = 0.5; % this is a check for the Sun case;

    ang_ext_Jupiter_Earth_rad = J_source_extent/d_EarthJmin; % angular source size =
diameter / distance from J to E. % meters cancel out, units rad.
    ang_ext_Jupiter_Earth_deg = ang_ext_Jupiter_Earth_rad*360/(2*pi);

    % Romero Wolf 2015
    Deltat_m_EarthS_2 = (h/c).*(((1+cosd(2*(theta)))./(cosd(theta))));
    Deltat_p_EarthS_2 = (h/
c).*(((1+cosd(2*(theta+ang_ext_Jupiter_Earth_deg))).(cosd(theta+ang_ext_Jupiter_Earth_de
g))));

    deltat_EarthS_2 = (Deltat_m_EarthS_2 - Deltat_p_EarthS_2); % pulse broadening
equation
    % delaySmear = deltat*bw; (if we have a specific bandwidth)

    elevation_angle = 90-theta;

    figure(1), set(gcf,'color','w');
    semilogy(elevation_angle,deltat_EarthS_2*1e6)
    xlabel('Elevation Angle (deg)')
    ylabel('Pulse Broadening (\mu s)')
```

```
    xlim([0 90])
    ylim([10^(-10) 10^(0)])
    grid on
    title('Jovian Pulse Broadening vs. Elevation Angle')
    hold on

    figure(2), set(gcf,'color','w');
    semilogy(theta,deltat_EarthS_2*1e6)
    xlabel('Incidence Angle (deg)')
    ylabel('Pulse Broadening (\mu s)')
    xlim([0 90])
    grid on
    title('Jovian Pulse Broadening vs. Incidence Angle')
    ylim([10^(-10) 10^(0)])
    hold on

end

BW = 30e6;
figure(1), hold on, yline((1/BW)*1e6,'--',['Pulse Width for ',num2str(BW/1e6),'MHz']);
figure(2), hold on, yline((1/BW)*1e6,'--',['Pulse Width for ',num2str(BW/1e6),'MHz']);

figure(1),     legend('20km','70km','400km','69,911km','location','SW')
figure(2),     legend('20km','70km','400km','69,911km','location','SE')
```

B. CODE FOR ESTIMATING PULSE BROADENING SEA CLIFF

```
clear all
close all

BW = 30e6;

set(0,'defaultAxesFontsize',18)
set(0,'defaultLineLineWidth',2);


h = 84;  % in meters
theta = 0.1:.1:89.9;  % length 401 % theta is the bistatic angle
c = 2.998*10^8; % m/s

% (1) could do a for loop over source sizes of 20km, 400km, and 69,911 km
%J_source_extent = 70; %~km Jupiter source extent in km. (400km) see K. Imai, L. Wang,
and T. D. Can, "Modeling Jupiter%s decametric modulation lanes,

J_source_extent_list = [20, 70, 400, 69911];
%J_source_extent_list = 70;

for ii = 1:length(J_source_extent_list)
    J_source_extent = J_source_extent_list(ii);
```

```
    d_EarthJmin = 588e6; %~km Jupiter to Earth (588 million kilometers) at their closest
point (https://www.space.com/18383-how-far-away-is-jupiter.html)

    % ang_ext_Jupiter_Earth_deg = 0.5; % this is a check for the Sun case;

    ang_ext_Jupiter_Earth_rad = J_source_extent/d_EarthJmin; % angular source size =
diameter / distance from J to E. % meters cancel out, units rad.
    ang_ext_Jupiter_Earth_deg = ang_ext_Jupiter_Earth_rad*360/(2*pi);

    % Romero Wolf 2015
    Deltat_m_EarthS_2 = (h/c).*(((1+cosd(2*(theta)))./(cosd(theta))));
    Deltat_p_EarthS_2 = (h/
c).*(((1+cosd(2*(theta+ang_ext_Jupiter_Earth_deg))).(cosd(theta+ang_ext_Jupiter_Earth_de
g))));

    deltat_EarthS_2 = (Deltat_m_EarthS_2 - Deltat_p_EarthS_2); % pulse broadening
equation
    % delaySmear = deltat*bw; (if we have a specific bandwidth)

    elevation_angle = 90-theta;

    figure(1), set(gcf,'color','w');
    semilogy(elevation_angle,deltat_EarthS_2*1e6)
    xlabel('Elevation Angle (deg)')
    ylabel('Pulse Broadening (\mu s)')
    xlim([0 90])
    ylim([10^(-10) 10^(0)])
    grid on
    title('Jovian Pulse Broadening for Big Sur')
    hold on

    figure(2), set(gcf,'color','w');
    semilogy(theta,deltat_EarthS_2*1e6)
    xlabel('Incidence Angle (deg)')
    ylabel('Pulse Broadening (\mu s)')
    xlim([0 90])
    grid on
    title('Jovian Pulse Broadening for Big Sur')
    ylim([10^(-10) 10^(0)])
    hold on

end

figure(1), hold on, yline((1/BW)*1e6,'--',['Pulse Width for ',num2str(BW/1e6),'MHz']);
figure(2), hold on, yline((1/BW)*1e6,'--',['Pulse Width for ',num2str(BW/1e6),'MHz']);

figure(1),     legend('20km','70km','400km','69,911km','location','SW')
figure(2),     legend('20km','70km','400km','69,911km','location','SE')
```

C. CODE FOR ESTIMATING PULSE BROADENING DEATH VALLEY

```
clear all
close all

set(0,'defaultAxesFontsize',18)
set(0,'defaultLineLineWidth',2);

BW = 30e6; % maximum usable bandwidth for Jovian bursts (extreme case)
h = 1781;  % in meters
theta = 0.1:.1:89.9;  % length 401 % theta is the bistatic angle
c = 2.998*10^8; % m/s

% (1) could do a for loop over source sizes of 20km, 400km, and 69,911 km
%J_source_extent = 70; %~km Jupiter source extent in km. (400km) see K. Imai, L. Wang,
and T. D. Can, "Modeling Jupiter%s decametric modulation lanes,

J_source_extent_list = [20, 70, 400, 69911];
%J_source_extent_list = 70;

for ii = 1:length(J_source_extent_list)
    J_source_extent = J_source_extent_list(ii);

    d_EarthJmin = 588e6; %~km Jupiter to Earth (588 million kilometers) at their closest
point (https://www.space.com/18383-how-far-away-is-jupiter.html)

    % ang_ext_Jupiter_Earth_deg = 0.5; % this is a check for the Sun case;

    ang_ext_Jupiter_Earth_rad = J_source_extent/d_EarthJmin; % angular source size =
diameter / distance from J to E. % meters cancel out, units rad.
    ang_ext_Jupiter_Earth_deg = ang_ext_Jupiter_Earth_rad*360/(2*pi);

    % Romero Wolf 2015
    Deltat_m_EarthS_2 = (h/c).*(((1+cosd(2*(theta))))./(cosd(theta))));
    Deltat_p_EarthS_2 = (h/
c).*(((1+cosd(2*(theta+ang_ext_Jupiter_Earth_deg)))./(cosd(theta+ang_ext_Jupiter_Earth_de
g))));

    deltat_EarthS_2 = (Deltat_m_EarthS_2 - Deltat_p_EarthS_2); % pulse broadening
equation
    % delaySmear = deltat*bw; (if we have a specific bandwidth)

    elevation_angle = 90-theta;

    figure(1), set(gcf,'color','w');
    semilogy(elevation_angle,deltat_EarthS_2*1e6)
    xlabel('Elevation Angle (deg)')
    ylabel('Pulse Broadening (\mu s)')
    xlim([0 90])
    ylim([10^(-9) 10^(0)])
    grid on
```

```
    title('Jovian Pulse Broadening for Death Valley')
    hold on

    figure(2), set(gcf,'color','w');
    semilogy(theta,deltat_EarthS_2*1e6)
    xlabel('Incidence Angle (deg)')
    ylabel('Pulse Broadening (\mu s)')
    xlim([0 90])
    grid on
    title('Jovian Pulse Broadening for Death Valley')
    ylim([10^(-9) 10^(0)])
    hold on

end


figure(1), hold on, yline((1/BW)*1e6,'--',['Pulse Width for ',num2str(BW/1e6),'MHz']);
figure(2), hold on, yline((1/BW)*1e6,'--',['Pulse Width for ',num2str(BW/1e6),'MHz']);

figure(1),     legend('20km','70km','400km','69,911km','location','SW')
figure(2),     legend('20km','70km','400km','69,911km','location','SE')
```

D. CODE FOR ESTIMATING JOVIAN BURST DELAY

```
% Estimating the delay as a function of the incidence angle (or elevation angle)
% at test sites (Big Sur and Death Valley)

% THe "%%" splits it up into distinct sections
% You can run these sections individually ("Run Current Section")
```

This first section is just for testing and validating against previous model Earth Curvature

```
h = 84;
c = 3e8;

R = 6371e3; % radius of curvature in meters

theta = 0:0.1:90; % incidence angle in degrees, use cosd;

a = R.*cosd(theta);
b = (R+h);
d1 = sqrt(a.^2 + b.^2 - R.^2)-a;
d2 = d1.*cosd(180-(2*theta));

t_est1 = (d1 - d2)/c;  % delay in seconds
```

```
t_est2 = d1.*(1+cosd(2*theta))/c; % delay in seconds (2nd estimate)

isequal(t_est1,t_est2)  % check that they are the same

close
% First Draft for Elevation Angle (Sanity Check)
figure
% Plot the delay (in microseconds)
plot(theta,t_est1*(1e6))
legend('delay 1')
pause(1)
hold on
plot(theta,t_est2*(1e6))
xlabel('Incidence Angle')
ylabel('Delay (\mu s)')
legend('delay 1','delay 2')
title('Delay as a function of Incidence Angle (\theta)')
close all


figure
% Plot the delay (in microseconds) but still in linear
alpha = 90 - theta;
plot(alpha,t_est1*(1e6))
xlabel('Elevation Angle')
ylabel('Delay (\mu s)')
legend('delay 1','delay 2')
title('Delay as a function of Incidence Angle (\theta)')
%
close all
% plot as a semilogy function and also limit the axis to 90 deg.
semilogy(alpha,t_est1*(1e6))
xlabel('Elevation Angle (deg)')
xlim([0 90])
ylim([10^(-2) 10^(0)])
ylabel('Delay (\mu s)')
title('Delay as a function of Elevation Angle (\theta)')
grid on

%%%%%%%%%%%%%%%%%%%%%%%%%%%%%%%%%%%%%%%%%%%%%%%%%%%%%%%%%%%%%%%%%%%%%%%%%%%%
%%%%%%%%%%%%%%%%%%%%%%%%%%%%%%%%%%%%%%%%%%%%%%%%%%%%%%%%%%%%%%%%%%%%%%%%%%%%
%%%%%%%%%%%%%%%%%%%%%%%%%%%%%%%%%%%%%%%%%%%%%%%%%%%%%%%%%%%%%%%%%%%%%%%%%%%%
%%%%%%%%%%%%%%%%%%%%%%%%%%%%%%%%%%%%%%%%%%%%%%%%%%%%%%%%%%%%%%%%%%%%%%%%%%%%
```

```
ans =

  logical

   0

Warning: Ignoring extra legend entries.
```

E. BIG SUR ESTIMATING BURST DELAY CODE

This Second Section Focuses on Big Sur Testing Only Placeholder of h = 84m.

```
clear all
close all

h = 84;  % just a placeholder in meters for sea cliff, will vary on site
c = 3e8;
R = 6371e3; % radius of curvature in meters

theta = 0:0.1:90; % incidence angle in degrees, use cosd;
alpha = 90 - theta;

a = R.*cosd(theta);
b = (R+h);
d1 = sqrt(a.^2 + b.^2 - R.^2)-a;
d2 = d1.*cosd(180-(2*theta));

t_est1 = (d1 - d2)/c;  % delay in seconds

% plot as a semilogy function and also limit the axis to 90 deg.
semilogy(alpha,t_est1*(1e6))
xlabel('Elevation Angle (deg)')
xlim([0 90])
ylim([10^(-2) 10^(0)])
ylabel('Delay (\mu s)')
title('Delay as a function of Elevation Angle (\theta)')
grid on
```

F. DEATH VALLEY ESTIMATING BURST DELAY CODE

This Third Section Focuses on Death Valley Testing Placeholder of h = 84m.

```
clear all
close all

h = 1780;  % just a placeholder in meters for DV cliff, will vary on site
c = 3e8;
R = 6371e3; % radius of curvature in meters

theta = 0:0.1:90; % incidence angle in degrees, use cosd;
alpha = 90 - theta;

a = R.*cosd(theta);
b = (R+h);
d1 = sqrt(a.^2 + b.^2 - R.^2)-a;
d2 = d1.*cosd(180-(2*theta));

t_est1 = (d1 - d2)/c;  % delay in seconds
```

```
% plot as a semilogy function and also limit the axis to 90 deg.
semilogy(alpha,t_est1*(1e6))
xlabel('Elevation Angle (deg)')
xlim([0 90])
%ylim([min(t_est1*(1e6)) max(t_est1*(1e6))])
ylim([10^(-2) 2.5*10^(1)])
ylabel('Delay (\mu s)')
title('Delay as a function of Elevation Angle (\theta)')
grid on
```

This Final Section Models the 2D Image of Delay in Color as a function of Elevation Angle and Altitude Adds in Contours Adds in Colorbar label Placeholder in meters currently 10:100, but will vary also consider using this for future space-based platform altitudes.

```
clear all
close all

h = (10:1:100).';  % just a placeholder in meters
%h = (84:1:1780).';  % just a placeholder in meters
c = 3e8;
R = 6371e3; % radius of curvature in meters

theta = 0:0.1:90; % incidence angle in degrees, use cosd;
alpha = 90 - theta;

a = R.*cosd(theta);
b = (R+h);
d1 = sqrt(a.^2 + b.^2 - R.^2)-a;
d2 = d1.*cosd(180-(2*theta));

t_est1 = (d1 - d2)/c;  % delay in seconds

% plot as a semilogy function and also limit the axis to 90 deg.
%semilogy(alpha,t_est1*(1e6))

imagesc(alpha,h,t_est1*(1e6))
xlabel('Elevation Angle (deg)')
%xlim([0 90])
%ylim([min(t_est1*(1e6)) max(t_est1*(1e6))])
%ylim([10^(-2) 2.5*10^(1)])
%ylim()
title('Delay as a function of Elevation Angle (\theta)')
colorbar
grid on
set(gca,'YDir','normal')

% Colorbar Labeling
```

```
yc = colorbar; %hc.Label.String = 'Maximum Altitude (km)';
LabelText = 'Delay (\mu s)';
ylabel(yc,LabelText,'FontSize',18)
hold on
% % Contour Adding and Labeling
[Co,hc] = contour(alpha,h, t_est1*(1e6), 'w-');%,'ShowText', 'on');
clabel(Co,hc,'FontSize',15,'FontWeight','bold','Color','white');
hc.LevelList=round(hc.LevelList,3)  %rounds levels to 3rd decimal place
clabel(Co,hc, 'labelspacing', 1000);
```

```
hc =

  Contour with properties:

    LineColor: [1 1 1]
    LineStyle: '-'
    LineWidth: 0.5000
         Fill: off
    LevelList: [0.1000 0.2000 0.3000 0.4000 0.5000 0.6000]
        XData: [90 89.9000 89.8000 89.7000 89.6000 89.5000 89.4000 89.3000 … ]
        YData: [91×1 double]
        ZData: [91×901 double]

  Use GET to show all properties
```

Published with MATLAB® R2021b

THIS PAGE INTENTIONALLY LEFT BLANK

APPENDIX B. BIG SUR IRI 2020 DATA FOR MATLAB MODELING

A. 20MAR2022 FULL DAY

yyyy/mmdd(or -ddd)/hh.h):2022/ 320/ 0.0LT geog Lat/Long/Alt= 36.3/ 238.2/ 100.0

IRIcor2 is used for topside Ne profile
URSI maps are used for the F2 peak density (NmF2)
foF2 STORM model is turned on
Shubin2015model is used for F2 peak height (hmF2)
ABT-2009 option is used for the bottomside thickness parameter B0
Scotto-97 no L option is used for the F1 occurrence probability
foE auroral storm model is turned off
IRI-1990 option is used for D-region
TBT-2012 with solar dependence is used for the electron temperature
Tru-2021 option is used for the ion temperature
RBV10+TBT15 option is used for ion composition
CGM coordinates not computed
auroral boundaries not computed

Solar and magnetic parameter for the 1st profile point:
Solar Zenith Angle/degree 141.8
Dip (Magnetic Inclination)/degree 60.21
Modip (Modified Dip)/degree 49.49
Solar Sunspot Number (12-months running mean) Rz12 48.6
Ionospheric-Effective Solar Index IG12 46.9
Solar radio flux F10.7 (daily) 94.1
Solar radio flux F10.7 (81-day average) 118.9

TEC [1.E16 m-2] is obtained by numerical integration in 1km steps
from 50 to 1500.0 km. t is the percentage of TEC above the F peak.

HOUR	M3000	B0	B1	E-VALLEY		PLASMA FREQUENCIES / MHz			
L.T.		km		W/km	Depth	foF2	foF1	foE	foD
1.0	2.9184	82.6	2.4	63.5	0.2024	3.714	0.000	0.448	0.180
2.0	2.9213	83.8	2.4	62.2	0.2229	3.595	0.000	0.448	0.180
3.0	2.9172	87.1	2.5	59.0	0.2735	3.334	0.000	0.448	0.180
4.0	2.9353	90.1	2.6	52.1	0.3812	3.155	0.000	0.448	0.180
5.0	2.9979	90.4	2.6	41.1	0.5540	3.463	0.000	0.452	0.180
6.0	3.0948	88.9	2.7	29.6	0.7349	4.386	0.000	1.219	0.180
7.0	3.1847	89.7	2.6	21.9	0.8567	5.589	0.000	2.221	0.180
8.0	3.2230	95.3	2.6	18.1	0.9164	6.638	0.000	2.758	0.180
9.0	3.1920	103.1	2.4	16.5	0.9411	7.410	0.000	3.083	0.225
10.0	3.1121	108.7	2.3	15.9	0.9505	7.991	4.520	3.290	0.251
11.0	3.0263	110.0	2.1	15.7	0.9539	8.375	4.633	3.410	0.261
12.0	2.9736	107.9	2.0	15.7	0.9549	8.479	4.674	3.455	0.264
13.0	2.9719	103.8	2.0	15.7	0.9543	8.367	4.650	3.429	0.262
14.0	3.0176	98.8	2.0	15.9	0.9517	8.215	4.556	3.328	0.255
15.0	3.0940	93.3	2.1	16.3	0.9444	8.070	0.000	3.145	0.235
16.0	3.1779	86.4	2.3	17.6	0.9250	7.795	0.000	2.856	0.180
17.0	3.2413	78.6	2.4	20.6	0.8770	7.249	0.000	2.391	0.180

18.0	3.2569	71.7	2.6	27.2	0.7735	6.448	0.000	1.523	0.180
19.0	3.2103	69.5	2.7	38.0	0.6040	5.545	0.000	0.566	0.180
20.0	3.1130	74.2	2.7	49.6	0.4214	4.751	0.000	0.448	0.180
21.0	3.0022	81.1	2.7	57.6	0.2953	4.213	0.000	0.448	0.180
22.0	2.9211	85.1	2.6	61.6	0.2324	3.930	0.000	0.448	0.180
23.0	2.8913	85.6	2.5	63.2	0.2062	3.800	0.000	0.448	0.180
24.0	2.9010	83.9	2.4	63.9	0.1960	3.746	0.000	0.448	0.180

B. 21JUN2022 FULL DAY

yyyy/mmdd(or -ddd)/hh.h):2022/ 621/ 0.0LT geog Lat/Long/Alt= 36.3/ 238.2/ 100.0

IRIcor2 is used for topside Ne profile
URSI maps are used for the F2 peak density (NmF2)
foF2 STORM model is turned on
Shubin2015model is used for F2 peak height (hmF2)
ABT-2009 option is used for the bottomside thickness parameter B0
Scotto-97 no L option is used for the F1 occurrence probability
foE auroral storm model is turned off
IRI-1990 option is used for D-region
TBT-2012 with solar dependence is used for the electron temperature
Tru-2021 option is used for the ion temperature
RBV10+TBT15 option is used for ion composition
CGM coordinates not computed
auroral boundaries not computed

Solar and magnetic parameter for the 1st profile point:
Solar Zenith Angle/degree 118.8
Dip (Magnetic Inclination)/degree 60.21
Modip (Modified Dip)/degree 49.49
Solar Sunspot Number (12-months running mean) Rz12 57.9
Ionospheric-Effective Solar Index IG12 66.6
Solar radio flux F10.7 (daily) 143.2
Solar radio flux F10.7 (81-day average) 130.0

TEC [1.E16 m-2] is obtained by numerical integration in 1km steps
from 50 to 1500.0 km. t is the percentage of TEC above the F peak.

-

HOUR	M3000	B0	B1	E-VALLEY		PLASMA FREQUENCIES / MHz			
L.T.		km		W/km	Depth	foF2	foF1	foE	foD
1.0	2.9638	83.1	2.6	60.7	0.2462	4.647	0.000	0.465	0.180
2.0	2.9529	83.2	2.5	55.6	0.3256	4.339	0.000	0.465	0.180
3.0	2.9399	87.6	2.5	46.3	0.4726	4.125	0.000	0.465	0.180
4.0	2.9384	96.2	2.4	34.4	0.6602	4.165	0.000	0.696	0.180
5.0	2.9541	105.0	2.3	24.7	0.8121	4.603	0.000	1.583	0.180
6.0	2.9743	111.5	2.3	19.4	0.8960	5.308	0.000	2.380	0.180
7.0	2.9763	116.8	2.2	17.1	0.9329	5.919	0.000	2.853	0.180
8.0	2.9465	123.2	2.1	16.1	0.9475	6.221	0.000	3.172	0.246
9.0	2.8925	129.7	2.1	15.8	0.9530	6.336	4.696	3.397	0.269
10.0	2.8377	134.1	2.0	15.7	0.9550	6.491	4.841	3.549	0.279
11.0	2.8035	135.3	1.9	15.6	0.9557	6.727	4.925	3.638	0.283
12.0	2.7960	132.9	1.9	15.6	0.9559	6.911	4.953	3.668	0.284
13.0	2.8082	127.9	1.9	15.6	0.9558	6.946	4.928	3.641	0.283

14.0	2.8329	122.3	1.9	15.7	0.9551	6.872	4.847	3.555	0.279
15.0	2.8713	117.9	2.0	15.8	0.9531	6.795	4.705	3.406	0.270
16.0	2.9273	113.7	2.1	16.1	0.9479	6.780	0.000	3.186	0.248
17.0	2.9956	106.4	2.2	17.0	0.9341	6.795	0.000	2.872	0.185
18.0	3.0563	94.8	2.3	19.2	0.8988	6.745	0.000	2.410	0.180
19.0	3.0859	82.8	2.5	24.4	0.8180	6.582	0.000	1.634	0.180
20.0	3.0747	76.7	2.6	33.8	0.6694	6.349	0.000	0.728	0.180
21.0	3.0361	77.2	2.6	45.7	0.4817	6.100	0.000	0.465	0.180
22.0	2.9961	80.8	2.7	55.3	0.3313	5.807	0.000	0.465	0.180
23.0	2.9735	83.9	2.7	60.5	0.2489	5.430	0.000	0.465	0.180
24.0	2.9674	84.5	2.6	62.8	0.2128	5.017	0.000	0.465	0.180

C. 22SEP2022 FULL DAY

yyyy/mmdd(or -ddd)/hh.h):2022/ 922/ 0.0LT geog Lat/Long/Alt= 36.3/ 238.2/ 100.0

IRIcor2 is used for topside Ne profile
URSI maps are used for the F2 peak density (NmF2)
foF2 STORM model is turned on
Shubin2015model is used for F2 peak height (hmF2)
ABT-2009 option is used for the bottomside thickness parameter B0
Scotto-97 no L option is used for the F1 occurrence probability
foE auroral storm model is turned off
IRI-1990 option is used for D-region
TBT-2012 with solar dependence is used for the electron temperature
Tru-2021 option is used for the ion temperature
RBV10+TBT15 option is used for ion composition
CGM coordinates not computed
auroral boundaries not computed

Solar and magnetic parameter for the 1st profile point:
Solar Zenith Angle/degree 140.4
Dip (Magnetic Inclination)/degree 60.21
Modip (Modified Dip)/degree 49.49
Solar Sunspot Number (12-months running mean) Rz12 65.0
Ionospheric-Effective Solar Index IG12 88.1
Solar radio flux F10.7 (daily) 137.7
Solar radio flux F10.7 (81-day average) 132.6

TEC [1.E16 m-2] is obtained by numerical integration in 1km steps
from 50 to 1500.0 km. t is the percentage of TEC above the F peak.

HOUR	M3000	B0	B1	E-VALLEY		PLASMA FREQUENCIES / MHz			
L.T.		km		W/km	Depth	foF2	foF1	foE	foD
1.0	2.9133	86.0	2.6	63.2	0.2060	4.355	0.000	0.476	0.180
2.0	2.8946	85.8	2.6	61.6	0.2320	4.195	0.000	0.476	0.180
3.0	2.8795	87.7	2.7	57.6	0.2942	3.884	0.000	0.476	0.180
4.0	2.9057	89.4	2.7	49.7	0.4196	3.762	0.000	0.476	0.180
5.0	2.9880	88.2	2.7	38.1	0.6018	4.276	0.000	0.575	0.180
6.0	3.0990	84.2	2.8	27.3	0.7719	5.416	0.000	1.552	0.180
7.0	3.1852	81.2	2.7	20.7	0.8762	6.705	0.000	2.449	0.180
8.0	3.2045	82.9	2.6	17.6	0.9247	7.746	0.000	2.929	0.186
9.0	3.1537	88.5	2.4	16.3	0.9443	8.525	0.000	3.228	0.250

10.0	3.0657	94.6	2.2	15.9	0.9517	9.145	4.702	3.416	0.272
11.0	2.9835	98.9	2.1	15.7	0.9543	9.569	4.801	3.519	0.280
12.0	2.9354	100.2	2.0	15.7	0.9549	9.751	4.827	3.547	0.282
13.0	2.9288	98.3	2.0	15.7	0.9539	9.775	4.783	3.500	0.278
14.0	2.9602	93.1	2.1	15.9	0.9505	9.734	0.000	3.377	0.268
15.0	3.0223	85.6	2.2	16.6	0.9409	9.577	0.000	3.163	0.240
16.0	3.1014	77.7	2.4	18.1	0.9160	9.179	0.000	2.829	0.180
17.0	3.1708	71.7	2.6	22.0	0.8559	8.470	0.000	2.275	0.180
18.0	3.1970	69.3	2.8	29.7	0.7334	7.488	0.000	1.242	0.180
19.0	3.1601	70.4	3.0	41.3	0.5522	6.406	0.000	0.476	0.180
20.0	3.0727	75.8	3.0	52.2	0.3798	5.496	0.000	0.476	0.180
21.0	2.9765	82.9	3.0	59.0	0.2727	4.931	0.000	0.476	0.180
22.0	2.9146	87.9	2.9	62.2	0.2226	4.648	0.000	0.476	0.180
23.0	2.9005	89.4	2.8	63.5	0.2023	4.489	0.000	0.476	0.180
24.0	2.9115	88.0	2.7	64.0	0.1946	4.403	0.000	0.476	0.180

D. 2022 FULL YEAR 0000

yyyy/mmdd(or -ddd)/hh.h):2022/-366/ 0.0LT geog Lat/Long/Alt= 36.3/ 238.2/ 100.0

IRIcor2 is used for topside Ne profile
URSI maps are used for the F2 peak density (NmF2)
foF2 STORM model is turned on
Shubin2015model is used for F2 peak height (hmF2)
ABT-2009 option is used for the bottomside thickness parameter B0
Scotto-97 no L option is used for the F1 occurrence probability
foE auroral storm model is turned off
IRI-1990 option is used for D-region
TBT-2012 with solar dependence is used for the electron temperature
Tru-2021 option is used for the ion temperature
RBV10+TBT15 option is used for ion composition
CGM coordinates not computed
auroral boundaries not computed

Solar and magnetic parameter for the 1st profile point:
Solar Zenith Angle/degree 166.7
Dip (Magnetic Inclination)/degree 60.21
Modip (Modified Dip)/degree 49.49
Solar Sunspot Number (12-months running mean) Rz12 40.7
Ionospheric-Effective Solar Index IG12 37.3
Solar radio flux F10.7 (daily) 90.8
Solar radio flux F10.7 (81-day average) 101.3

TEC [1.E16 m-2] is obtained by numerical integration in 1km steps
from 50 to 1500.0 km. t is the percentage of TEC above the F peak.

-

DAYOF	M3000	B0	B1	E-VALLEY		PLASMA FREQUENCIES / MHz			
YEAR		km		W/km	Depth	foF2	foF1	foE	foD
1.0	3.0902	87.2	2.6	64.2	0.1915	2.529	0.000	0.431	0.180
6.0	3.0867	86.8	2.6	64.2	0.1915	2.472	0.000	0.432	0.180
11.0	3.0833	86.4	2.6	64.2	0.1915	2.415	0.000	0.434	0.180
16.0	3.0780	86.1	2.6	64.2	0.1915	2.512	0.000	0.436	0.180
21.0	3.0654	85.7	2.5	64.2	0.1916	2.615	0.000	0.437	0.180

26.0	3.0528	85.5	2.5	64.1	0.1916	2.842	0.000	0.438	0.180
31.0	3.0402	85.2	2.5	64.1	0.1917	3.024	0.000	0.438	0.180
36.0	3.0275	85.0	2.5	64.1	0.1918	3.364	0.000	0.439	0.180
41.0	3.0149	84.8	2.5	64.1	0.1920	3.432	0.000	0.440	0.180
46.0	3.0017	84.6	2.5	64.1	0.1921	3.598	0.000	0.441	0.180
51.0	2.9862	84.4	2.5	64.1	0.1925	3.639	0.000	0.442	0.180
56.0	2.9708	84.3	2.5	64.1	0.1927	3.619	0.000	0.442	0.180
61.0	2.9553	84.1	2.4	64.1	0.1930	3.630	0.000	0.444	0.180
66.0	2.9398	84.1	2.4	64.0	0.1934	3.640	0.000	0.445	0.180
71.0	2.9244	84.0	2.4	64.0	0.1938	3.645	0.000	0.445	0.180
76.0	2.9094	83.9	2.4	64.0	0.1943	3.693	0.000	0.447	0.180
81.0	2.8953	83.9	2.4	63.9	0.1949	3.781	0.000	0.448	0.180
86.0	2.8813	83.8	2.4	63.9	0.1955	3.869	0.000	0.449	0.180
91.0	2.8672	83.8	2.4	63.9	0.1962	3.923	0.000	0.450	0.180
96.0	2.8531	83.8	2.5	63.8	0.1971	4.045	0.000	0.452	0.180
101.0	2.8390	83.7	2.5	63.7	0.1980	4.108	0.000	0.454	0.180
106.0	2.8300	83.7	2.5	63.7	0.1991	4.223	0.000	0.455	0.180
111.0	2.8414	83.7	2.5	63.6	0.2002	4.291	0.000	0.456	0.180
116.0	2.8529	83.8	2.5	63.5	0.2015	4.365	0.000	0.456	0.180
121.0	2.8643	83.8	2.5	63.4	0.2028	4.439	0.000	0.457	0.180
126.0	2.8757	83.8	2.5	63.4	0.2042	4.512	0.000	0.457	0.180
131.0	2.8872	83.9	2.5	63.3	0.2057	4.586	0.000	0.458	0.180
136.0	2.8985	83.9	2.5	63.2	0.2071	4.656	0.000	0.459	0.180
141.0	2.9096	84.0	2.5	63.1	0.2084	4.713	0.000	0.460	0.180
146.0	2.9206	84.0	2.6	63.0	0.2096	4.770	0.000	0.461	0.180
151.0	2.9316	84.1	2.6	62.9	0.2106	4.827	0 000	0.462	0.180
156.0	2.9427	84.2	2 6	62.9	0.2114	4.884	0.000	0.463	0.180
161.0	2.9537	84.3	2.6	62.9	0.2118	4.942	0.000	0.464	0.180
166.0	2.9647	84.4	2.6	62.9	0.2119	4.999	0.000	0.465	0.180
171.0	2.9670	84.5	2.6	62.9	0.2117	5.014	0.000	0.465	0.180
176.0	2.9692	84.6	2.6	62.9	0.2113	5.028	0.000	0.465	0.180
181.0	2.9715	84.7	2.6	63.0	0.2105	5.043	0.000	0.465	0.180
186.0	2.9737	84.8	2.7	63.0	0.2096	5.050	0.000	0.466	0.180
191.0	2.9760	85.0	2.7	63.1	0.2085	5.073	0.000	0.467	0.180
196.0	2.9782	85.1	2.7	63.2	0.2073	5.088	0.000	0.468	0.180
201.0	2.9688	85.3	2.7	63.2	0.2061	4.985	0.000	0.468	0.180
206.0	2.9593	85.5	2.7	63.3	0.2049	5.027	0.000	0.469	0.180
211.0	2.9499	85.7	2.7	63.4	0.2037	4.996	0.000	0.469	0.180
216.0	2.9404	85.8	2.7	63.5	0.2027	4.965	0.000	0.470	0.180
221.0	2.9309	86.0	2.7	63.5	0.2016	4.904	0.000	0.470	0.180
226.0	2.9215	86.3	2.7	63.6	0.2007	4.903	0.000	0.470	0.180
231.0	2.9172	86.5	2.7	63.6	0.1999	4.672	0.000	0.471	0.180
236.0	2.9142	86.7	2.7	63.7	0.1991	4.775	0.000	0.472	0.180
241.0	2.9112	86.9	2.7	63.7	0.1984	4.706	0.000	0.473	0.180
246.0	2.9082	87.1	2.7	63.8	0.1978	4.643	0.000	0.473	0.180
251.0	2.9052	87.4	2.7	63.8	0.1973	4.570	0.000	0.474	0.180
256.0	2.9022	87.6	2.7	63.8	0.1968	4.502	0.000	0.474	0.180
261.0	2.9055	87.8	2.7	63.9	0.1963	4.444	0.000	0.475	0.180
266.0	2.9130	88.0	2.7	63.9	0.1959	4.393	0.000	0.476	0.180
271.0	2.9205	88.3	2.7	63.9	0.1955	4.344	0.000	0.476	0.180
276.0	2.9279	88.5	2.7	63.9	0.1951	4.332	0.000	0.475	0.180
281.0	2.9354	88.7	2.7	64.0	0.1948	4.240	0.000	0.475	0.180
286.0	2.9429	88.9	2.7	64.0	0.1945	4.189	0.000	0.476	0.180
291.0	2.9577	89.1	2.7	64.0	0.1942	4.161	0.000	0.476	0.180
296.0	2.9773	89.3	2.7	64.0	0.1939	4.241	0.000	0.475	0.180

301.0	2.9969	89.5	2.7	64.0	0.1936	4.133	0.000	0.474	0.180
306.0	3.0165	89.7	2.7	64.0	0.1934	4.120	0.000	0.475	0.180
311.0	3.0361	89.8	2.7	64.1	0.1931	4.106	0.000	0.475	0.180
316.0	3.0557	90.0	2.8	64.1	0.1929	4.092	0.000	0.475	0.180
321.0	3.0654	90.2	2.8	64.1	0.1927	4.034	0.000	0.454	0.180
326.0	3.0601	90.3	2.8	64.1	0.1924	3.908	0.000	0.455	0.180
331.0	3.0548	90.4	2.8	64.1	0.1922	3.783	0.000	0.455	0.180
336.0	3.0496	90.5	2.8	64.1	0.1920	3.658	0.000	0.455	0.180
341.0	3.0443	90.6	2.9	64.1	0.1919	3.532	0.000	0.456	0.180
346.0	3.0390	90.7	2.9	64.1	0.1918	3.407	0.000	0.456	0.180
351.0	3.0352	90.8	2.9	64.1	0.1917	3.322	0.000	0.457	0.180
356.0	3.0335	90.8	3.0	64.1	0.1916	3.298	0.000	0.457	0.180
361.0	3.0317	90.8	3.0	64.2	0.1916	3.273	0.000	0.457	0.180

E. 2022 FULL YEAR 1200

yyyy/mmdd(or -ddd)/hh.h):2022/-366/12.0LT geog Lat/Long/Alt= 36.3/ 238.2/ 100.0

IRIcor2 is used for topside Ne profile
URSI maps are used for the F2 peak density (NmF2)
foF2 STORM model is turned on
Shubin2015model is used for F2 peak height (hmF2)
ABT-2009 option is used for the bottomside thickness parameter B0
Scotto-97 no L option is used for the F1 occurrence probability
foE auroral storm model is turned off
IRI-1990 option is used for D-region
TBT-2012 with solar dependence is used for the electron temperature
Tru-2021 option is used for the ion temperature
RBV10+TBT15 option is used for ion composition
CGM coordinates not computed
auroral boundaries not computed

Solar and magnetic parameter for the 1st profile point:
Solar Zenith Angle/degree 59.3
Dip (Magnetic Inclination)/degree 60.21
Modip (Modified Dip)/degree 49.49
Solar Sunspot Number (12-months running mean) Rz12 40.7
Ionospheric-Effective Solar Index IG12 37.3
Solar radio flux F10.7 (daily) 90.8
Solar radio flux F10.7 (81-day average) 101.3

TEC [1.E16 m-2] is obtained by numerical integration in 1km steps
from 50 to 1500.0 km. t is the percentage of TEC above the F peak.

-

HOUR	M3000	B0	B1	E-VALLEY		PLASMA FREQUENCIES /MHz			
L.T.		km		W/km	Depth	foF2	foF1	foE	foD
1.0	3.3808	81.6	2.3	15.8	0.9086	7.866	0.000	3.062	0.205
6.0	3.3731	81.7	2.3	15.8	0.9086	7.844	0.000	3.074	0.208
11.0	3.3654	82.1	2.3	15.8	0.9088	7.822	0.000	3.094	0.212
16.0	3.3555	82.8	2.3	15.8	0.9089	8.141	0.000	3.118	0.216
21.0	3.3364	83.7	2.3	15.8	0.9091	7.863	0.000	3.141	0.221
26.0	3.3173	84.9	2.2	15.8	0.9092	7.913	0.000	3.165	0.226

31.0	3.2982	86.3	2.2	15.8	0.9094	7.963	0.000	3.190	0.230
36.0	3.2791	88.0	2.2	15.8	0.9096	8.400	0.000	3.217	0.235
41.0	3.2600	90.0	2.2	15.8	0.9098	8.279	0.000	3.245	0.240
46.0	3.2365	92.1	2.2	15.7	0.9100	8.119	0.000	3.276	0.244
51.0	3.1951	94.4	2.1	15.7	0.9539	8.231	4.489	3.304	0.248
56.0	3.1536	96.8	2.1	15.7	0.9541	8.280	4.525	3.331	0.251
61.0	3.1122	99.3	2.1	15.7	0.9543	8.361	4.560	3.361	0.255
66.0	3.0708	101.7	2.1	15.7	0.9545	8.442	4.593	3.388	0.258
71.0	3.0294	104.1	2.0	15.7	0.9546	8.564	4.626	3.413	0.260
76.0	2.9921	106.5	2.0	15.7	0.9548	8.534	4.657	3.440	0.263
81.0	2.9612	108.8	2.0	15.7	0.9549	8.442	4.686	3.465	0.265
86.0	2.9302	111.2	2.0	15.7	0.9551	8.345	4.713	3.487	0.267
91.0	2.8992	113.5	2.0	15.6	0.9552	8.251	4.739	3.508	0.269
96.0	2.8683	115.9	2.0	15.6	0.9553	8.167	4.763	3.529	0.270
101.0	2.8373	118.1	1.9	15.6	0.9554	8.075	4.785	3.549	0.272
106.0	2.8111	120.3	1.9	15.6	0.9555	7.972	4.806	3.566	0.273
111.0	2.8038	122.3	1.9	15.6	0.9555	7.824	4.825	3.580	0.274
116.0	2.7966	124.2	1.9	15.6	0.9556	7.676	4.843	3.592	0.276
121.0	2.7893	126.0	1.9	15.6	0.9557	7.528	4.860	3.602	0.277
126.0	2.7821	127.6	1.9	15.6	0.9557	7.381	4.875	3.612	0.278
131.0	2.7748	129.0	1.9	15.6	0.9558	7.233	4.889	3.622	0.279
136.0	2.7696	130.2	1.9	15.6	0.9558	7.106	4.901	3.631	0.280
141.0	2.7729	131.2	1.9	15.6	0.9558	7.063	4.912	3.639	0.281
146.0	2.7761	132.0	1.9	15.6	0.9559	7.020	4.921	3.646	0.281
151.0	2.7793	132.6	1.9	15.6	0.9559	6.977	4.929	3.651	0.282
156.0	2.7826	133.0	1.9	15.6	0.9559	6.934	4.936	3.656	0.283
161.0	2.7858	133.3	1.9	15.6	0.9559	6.891	4.943	3.662	0.283
166.0	2.7890	133.3	1.9	15.6	0.9559	6.811	4.948	3.667	0.284
171.0	2.7948	133.0	1.9	15.6	0.9559	6.901	4.953	3.668	0.284
176.0	2.8006	132.6	1.9	15.6	0.9559	6.953	4.956	3.667	0.285
181.0	2.8064	131.9	1.9	15.6	0.9559	7.005	4.959	3.667	0.285
186.0	2.8122	131.0	1.9	15.6	0.9559	7.057	4.961	3.668	0.285
191.0	2.8180	130.0	1.9	15.6	0.9559	7.110	4.962	3.669	0.286
196.0	2.8238	128.8	1.9	15.6	0.9559	7.162	4.963	3.669	0.286
201.0	2.8191	127.5	1.9	15.6	0.9558	7.302	4.963	3.666	0.286
206.0	2.8144	125.9	1.9	15.6	0.9558	7.441	4.962	3.665	0.286
211.0	2.8097	124.3	1.9	15.6	0.9558	7.581	4.959	3.662	0.287
216.0	2.8050	122.4	1.9	15.6	0.9557	7.721	4.956	3.656	0.287
221.0	2.8003	120.5	1.9	15.6	0.9557	7.793	4.951	3.648	0.287
226.0	2.7956	118.5	1.9	15.6	0.9556	8.000	4.944	3.641	0.287
231.0	2.8076	116.3	1.9	15.6	0.9555	8.104	4.936	3.634	0.287
236.0	2.8237	114.1	1.9	15.6	0.9555	8.436	4.925	3.626	0.286
241.0	2.8397	111.8	1.9	15.6	0.9554	8.665	4.913	3.617	0.286
246.0	2.8558	109.4	2.0	15.6	0.9553	8.842	4.899	3.606	0.285
251.0	2.8719	107.0	2.0	15.6	0.9552	9.116	4.883	3.591	0.285
256.0	2.8880	104.6	2.0	15.7	0.9551	9.343	4.865	3.575	0.284
261.0	2.9120	102.1	2.0	15.7	0.9550	9.570	4.845	3.560	0.283
266.0	2.9412	99.8	2.0	15.7	0.9548	9.796	4.823	3.543	0.281
271.0	2.9704	97.5	2.0	15.7	0.9547	10.022	4.798	3.521	0.280
276.0	2.9996	95.3	2.0	15.7	0.9545	10.152	4.772	3.495	0.278
281.0	3.0288	93.3	2.0	15.7	0.9543	10.475	4.744	3.472	0.276
286.0	3.0581	91.5	2.0	15.7	0.9541	10.702	4.715	3.450	0.273
291.0	3.0887	89.7	2.0	15.7	0.9539	10.852	0.000	3.425	0.270
296.0	3.1204	88.2	2.0	15.7	0.9537	11.319	0.000	3.395	0.267
301.0	3.1520	86.9	2.1	15.8	0.9535	11.050	0.000	3.366	0.263

306.0	3.1837	85.8	2.1	15.8	0.9533	11.149	0.000	3.342	0.259
311.0	3.2154	84.9	2.1	15.8	0.9531	11.807	0.000	3.317	0.255
316.0	3.2470	84.4	2.1	15.8	0.9529	11.348	0.000	3.292	0.251
321.0	3.2679	84.1	2.1	15.8	0.9527	11.356	0.000	3.205	0.246
326.0	3.2727	84.2	2.1	15.8	0.9090	11.227	0.000	3.186	0.242
331.0	3.2775	84.7	2.1	15.8	0.9088	11.098	0.000	3.168	0.238
336.0	3.2823	85.6	2.1	15.8	0.9087	10.969	0.000	3.154	0.234
341.0	3.2872	86.8	2.1	15.8	0.9086	10.840	0.000	3.142	0.231
346.0	3.2920	88.4	2.1	15.8	0.9085	10.711	0.000	3.134	0.229
351.0	3.2913	90.4	2.1	15.8	0.9085	10.626	0.000	3.130	0.228
356.0	3.2823	92.8	2.1	15.9	0.9085	10.608	0.000	3.130	0.228
361.0	3.2733	95.7	2.1	15.8	0.9085	10.589	0.000	3.134	0.229

APPENDIX C. DEATH VALLEY IRI 2020 DATA FOR MATLAB MODELING

A. 20MAR2022 FULL DAY

yyyy/mmdd(or -ddd)/hh.h):2022/ 320/ 0.0LT geog Lat/Long/Alt= 36.4/ 243.2/ 100.0

IRIcor2 is used for topside Ne profile
URSI maps are used for the F2 peak density (NmF2)
foF2 STORM model is turned on
Shubin2015model is used for F2 peak height (hmF2)
ABT-2009 option is used for the bottomside thickness parameter B0
Scotto-97 no L option is used for the F1 occurrence probability
foE auroral storm model is turned off
IRI-1990 option is used for D-region
TBT-2012 with solar dependence is used for the electron temperature
Tru-2021 option is used for the ion temperature
RBV10+TBT15 option is used for ion composition
CGM coordinates not computed
auroral boundaries not computed

Solar and magnetic parameter for the 1st profile point:
Solar Zenith Angle/degree 141.7
Dip (Magnetic Inclination)/degree 61.32
Modip (Modified Dip)/degree 50.03
Solar Sunspot Number (12-months running mean) Rz12 48.6
Ionospheric-Effective Solar Index IG12 46.9
Solar radio flux F10.7 (daily) 94.1
Solar radio flux F10.7 (81-day average) 118.9

TEC [1.E16 m-2] is obtained by numerical integration in 1km steps
from 50 to 1500.0 km. t is the percentage of TEC above the F peak.

-

HOUR	M3000	B0	B1	E-VALLEY		PLASMA FREQUENCIES / MHz			
L.T.		km		W/km	Depth	foF2	foF1	foE	foD
1.0	2.9192	83.3	2.4	63.6	0.2025	3.696	0.000	0.448	0.180
2.0	2.9168	84.7	2.4	62.3	0.2230	3.585	0.000	0.448	0.180
3.0	2.9109	88.1	2.5	59.1	0.2735	3.330	0.000	0.448	0.180
4.0	2.9310	91.0	2.6	52.2	0.3814	3.149	0.000	0.448	0.180
5.0	2.9964	91.2	2.6	41.2	0.5542	3.437	0.000	0.453	0.180
6.0	3.0941	89.6	2.7	29.7	0.7350	4.326	0.000	1.219	0.180
7.0	3.1828	90.3	2.6	22.0	0.8566	5.492	0.000	2.220	0.180
8.0	3.2204	95.6	2.6	18.2	0.9162	6.519	0.000	2.756	0.180
9.0	3.1914	103.1	2.4	16.6	0.9408	7.280	0.000	3.081	0.225
10.0	3.1159	108.4	2.3	16.0	0.9502	7.854	4.511	3.288	0.251
11.0	3.0338	109.7	2.1	15.8	0.9537	8.236	4.623	3.408	0.261
12.0	2.9816	107.6	2.0	15.8	0.9546	8.348	4.665	3.453	0.264
13.0	2.9773	103.7	2.0	15.8	0.9540	8.244	4.640	3.427	0.262
14.0	3.0200	98.9	2.0	16.0	0.9515	8.090	4.547	3.327	0.255
15.0	3.0953	93.5	2.1	16.4	0.9441	7.947	0.000	3.144	0.234
16.0	3.1796	86.7	2.3	17.7	0.9248	7.700	0.000	2.854	0.180

17.0	3.2428	78.7	2.4	20.7	0.8769	7.209	0.000	2.390	0.180
18.0	3.2560	71.9	2.6	27.3	0.7735	6.455	0.000	1.523	0.180
19.0	3.2061	70.1	2.7	38.1	0.6042	5.569	0.000	0.567	0.180
20.0	3.1078	74.9	2.7	49.7	0.4216	4.763	0.000	0.448	0.180
21.0	3.0002	81.6	2.7	57.7	0.2954	4.205	0.000	0.448	0.180
22.0	2.9245	85.5	2.6	61.7	0.2325	3.906	0.000	0.448	0.180
23.0	2.8984	85.9	2.5	63.4	0.2062	3.771	0.000	0.448	0.180
24.0	2.9070	84.4	2.4	64.0	0.1960	3.719	0.000	0.448	0.180

B. 21JUN2022 FULL DAY

yyyy/mmdd(or -ddd)/hh.h):2022/ 621/ 0.0LT geog Lat/Long/Alt= 36.4/ 243.2/ 100.0

IRIcor2 is used for topside Ne profile
URSI maps are used for the F2 peak density (NmF2)
foF2 STORM model is turned on
Shubin2015model is used for F2 peak height (hmF2)
ABT-2009 option is used for the bottomside thickness parameter B0
Scotto-97 no L option is used for the F1 occurrence probability
foE auroral storm model is turned off
IRI-1990 option is used for D-region
TBT-2012 with solar dependence is used for the electron temperature
Tru-2021 option is used for the ion temperature
RBV10+TBT15 option is used for ion composition
CGM coordinates not computed
auroral boundaries not computed

Solar and magnetic parameter for the 1st profile point:
Solar Zenith Angle/degree 118.6
Dip (Magnetic Inclination)/degree 61.31
Modip (Modified Dip)/degree 50.03
Solar Sunspot Number (12-months running mean) Rz12 57.9
Ionospheric-Effective Solar Index IG12 66.6
Solar radio flux F10.7 (daily) 143.2
Solar radio flux F10.7 (81-day average) 130.0

TEC [1.E16 m-2] is obtained by numerical integration in 1km steps
from 50 to 1500.0 km. t is the percentage of TEC above the F peak.

-

HOUR	M3000	B0	B1	E-VALLEY		PLASMA FREQUENCIES / MHz			
L.T.		km		W/km	Depth	foF2	foF1	foE	foD
1.0	2.9733	83.9	2.6	60.8	0.2467	4.555	0.000	0.465	0.180
2.0	2.9668	84.3	2.5	55.7	0.3267	4.251	0.000	0.465	0.180
3.0	2.9586	89.0	2.4	46.3	0.4743	4.044	0.000	0.465	0.180
4.0	2.9586	97.5	2.4	34.4	0.6619	4.088	0.000	0.702	0.180
5.0	2.9700	106.2	2.3	24.8	0.8131	4.528	0.000	1.589	0.180
6.0	2.9821	112.4	2.3	19.5	0.8963	5.238	0.000	2.383	0.180
7.0	2.9773	117.3	2.2	17.1	0.9329	5.863	0.000	2.853	0.180
8.0	2.9459	123.2	2.1	16.2	0.9473	6.181	0.000	3.172	0.246
9.0	2.8960	129.2	2.1	15.9	0.9527	6.305	4.688	3.396	0.269
10.0	2.8472	133.3	2.0	15.8	0.9547	6.458	4.832	3.548	0.279
11.0	2.8165	134.5	1.9	15.7	0.9555	6.688	4.916	3.637	0.283

12.0	2.8085	132.4	1.9	15.7	0.9556	6.868	4.944	3.667	0.284
13.0	2.8180	127.7	1.9	15.7	0.9555	6.902	4.919	3.640	0.283
14.0	2.8406	122.5	1.9	15.8	0.9548	6.828	4.838	3.554	0.279
15.0	2.8785	118.3	2.0	15.9	0.9529	6.747	4.697	3.406	0.270
16.0	2.9346	114.1	2.1	16.2	0.9477	6.729	0.000	3.186	0.248
17.0	3.0018	106.8	2.2	17.1	0.9340	6.748	0.000	2.873	0.185
18.0	3.0602	95.2	2.3	19.3	0.8991	6.712	0.000	2.412	0.180
19.0	3.0880	83.5	2.5	24.4	0.8189	6.560	0.000	1.640	0.180
20.0	3.0772	77.6	2.6	33.8	0.6710	6.326	0.000	0.733	0.180
21.0	3.0409	77.9	2.6	45.7	0.4835	6.061	0.000	0.465	0.180
22.0	3.0030	81.2	2.7	55.3	0.3325	5.748	0.000	0.465	0.180
23.0	2.9811	84.3	2.7	60.6	0.2494	5.353	0.000	0.465	0.180
24.0	2.9751	85.0	2.6	62.9	0.2130	4.928	0.000	0.465	0.180

C. 22SEP2022 FULL DAY

yyyy/mmdd(or -ddd)/hh.h):2022/ 922/ 0.0LT geog Lat/Long/Alt= 36.4/ 243.2/ 100.0

IRIcor2 is used for topside Ne profile
URSI maps are used for the F2 peak density (NmF2)
foF2 STORM model is turned on
Shubin2015model is used for F2 peak height (hmF2)
ABT-2009 option is used for the bottomside thickness parameter B0
Scotto-97 no L option is used for the F1 occurrence probability
foE auroral storm model is turned off
IRI-1990 option is used for D-region
TBT-2012 with solar dependence is used for the electron temperature
Tru-2021 option is used for the ion temperature
RBV10+TBT15 option is used for ion composition
CGM coordinates not computed
auroral boundaries not computed

Solar and magnetic parameter for the 1st profile point:
Solar Zenith Angle/degree 140.3
Dip (Magnetic Inclination)/degree 61.31
Modip (Modified Dip)/degree 50.02
Solar Sunspot Number (12-months running mean) Rz12 65.0
Ionospheric-Effective Solar Index IG12 88.1
Solar radio flux F10.7 (daily) 137.7
Solar radio flux F10.7 (81-day average) 132.6

TEC [1.E16 m-2] is obtained by numerical integration in 1km steps
from 50 to 1500.0 km. t is the percentage of TEC above the F peak.

-

HOUR	M3000	B0	B1	E-VALLEY		PLASMA FREQUENCIES / MHz			
L.T.		km		W/km	Depth	foF2	foF1	foE	foD
1.0	2.9194	86.5	2.6	63.4	0.2060	4.365	0.000	0.476	0.180
2.0	2.8981	86.4	2.6	61.7	0.2320	4.215	0.000	0.476	0.180
3.0	2.8805	88.3	2.7	57.7	0.2944	3.908	0.000	0.476	0.180
4.0	2.9058	90.1	2.7	49.8	0.4198	3.776	0.000	0.476	0.180
5.0	2.9889	88.8	2.7	38.2	0.6021	4.264	0.000	0.576	0.180
6.0	3.1014	84.8	2.7	27.4	0.7720	5.376	0.000	1.552	0.180

7.0	3.1889	81.7	2.7	20.8	0.8761	6.650	0.000	2.448	0.180
8.0	3.2088	83.1	2.6	17.7	0.9245	7.686	0.000	2.927	0.186
9.0	3.1588	88.4	2.4	16.4	0.9440	8.457	0.000	3.226	0.250
10.0	3.0728	94.3	2.2	16.0	0.9514	9.066	4.692	3.414	0.272
11.0	2.9942	98.3	2.1	15.8	0.9540	9.488	4.791	3.517	0.280
12.0	2.9500	99.6	2.0	15.8	0.9546	9.673	4.817	3.545	0.282
13.0	2.9460	97.7	2.0	15.8	0.9536	9.695	4.773	3.499	0.278
14.0	2.9766	92.7	2.1	16.0	0.9502	9.647	0.000	3.375	0.268
15.0	3.0346	85.4	2.2	16.7	0.9407	9.497	0.000	3.162	0.239
16.0	3.1073	77.4	2.4	18.2	0.9158	9.134	0.000	2.827	0.180
17.0	3.1702	71.3	2.6	22.0	0.8558	8.473	0.000	2.274	0.180
18.0	3.1918	68.7	2.8	29.8	0.7336	7.525	0.000	1.242	0.180
19.0	3.1533	70.2	3.0	41.3	0.5524	6.448	0.000	0.476	0.180
20.0	3.0672	75.9	3.0	52.3	0.3801	5.519	0.000	0.476	0.180
21.0	2.9747	83.0	3.0	59.1	0.2729	4.931	0.000	0.476	0.180
22.0	2.9172	88.0	2.9	62.3	0.2227	4.636	0.000	0.476	0.180
23.0	2.9066	89.5	2.8	63.6	0.2023	4.478	0.000	0.476	0.180
24.0	2.9188	88.3	2.7	64.1	0.1946	4.402	0.000	0.476	0.180

D. 2022 FULL YEAR 0000

yyyy/mmdd(or -ddd)/hh.h):2022/-366/ 0.0LT geog Lat/Long/Alt= 36.4/ 243.2/ 1.8

IRIcor2 is used for topside Ne profile
URSI maps are used for the F2 peak density (NmF2)
foF2 STORM model is turned on
Shubin2015model is used for F2 peak height (hmF2)
ABT-2009 option is used for the bottomside thickness parameter B0
Scotto-97 no L option is used for the F1 occurrence probability
foE auroral storm model is turned off
IRI-1990 option is used for D-region
TBT-2012 with solar dependence is used for the electron temperature
Tru-2021 option is used for the ion temperature
RBV10+TBT15 option is used for ion composition
CGM coordinates not computed
auroral boundaries not computed

Solar and magnetic parameter for the 1st profile point:
Solar Zenith Angle/degree 166.6
Dip (Magnetic Inclination)/degree 61.32
Modip (Modified Dip)/degree 50.03
Solar Sunspot Number (12-months running mean) Rz12 40.7
Ionospheric-Effective Solar Index IG12 37.3
Solar radio flux F10.7 (daily) 90.8
Solar radio flux F10.7 (81-day average) 101.3

TEC [1.E16 m-2] is obtained by numerical integration in 1km steps
from 50 to 1500.0 km. t is the percentage of TEC above the F peak.

-

DAYOF	M3000	B0	B1	E-VALLEY		PLASMA FREQUENCIES / MHz			
YEAR		km		W/km	Depth	foF2	foF1	foE	foD
1.0	3.0885	87.3	2.6	64.3	0.1915	2.524	0.000	0.431	0.180

6.0	3.0855	86.9	2.6	64.3	0.1915	2.472	0.000	0.432	0.180
11.0	3.0826	86.6	2.6	64.3	0.1915	2.420	0.000	0.434	0.180
16.0	3.0781	86.3	2.6	64.3	0.1915	2.517	0.000	0.436	0.180
21.0	3.0674	86.0	2.5	64.3	0.1916	2.606	0.000	0.437	0.180
26.0	3.0567	85.8	2.5	64.3	0.1916	2.826	0.000	0.438	0.180
31.0	3.0460	85.5	2.5	64.3	0.1917	2.985	0.000	0.438	0.180
36.0	3.0353	85.3	2.5	64.3	0.1918	3.298	0.000	0.439	0.180
41.0	3.0247	85.2	2.5	64.3	0.1920	3.363	0.000	0.440	0.180
46.0	3.0128	85.0	2.5	64.2	0.1921	3.519	0.000	0.441	0.180
51.0	2.9964	84.8	2.5	64.2	0.1925	3.550	0.000	0.442	0.180
56.0	2.9799	84.7	2.4	64.2	0.1927	3.560	0.000	0.442	0.180
61.0	2.9635	84.6	2.4	64.2	0.1930	3.581	0.000	0.444	0.180
66.0	2.9470	84.5	2.4	64.2	0.1934	3.609	0.000	0.445	0.180
71.0	2.9305	84.5	2.4	64.1	0.1938	3.615	0.000	0.445	0.180
76.0	2.9152	84.4	2.4	64.1	0.1943	3.669	0.000	0.447	0.180
81.0	2.9016	84.4	2.4	64.1	0.1949	3.753	0.000	0.448	0.180
86.0	2.8879	84.3	2.4	64.0	0.1955	3.838	0.000	0.449	0.180
91.0	2.8743	84.3	2.4	64.0	0.1963	3.878	0.000	0.450	0.180
96.0	2.8606	84.3	2.4	63.9	0.1971	4.006	0.000	0.452	0.180
101.0	2.8470	84.3	2.5	63.9	0.1981	4.056	0.000	0.454	0.180
106.0	2.8382	84.3	2.5	63.8	0.1991	4.180	0.000	0.455	0.180
111.0	2.8489	84.3	2.5	63.7	0.2003	4.243	0.000	0.456	0.180
116.0	2.8597	84.3	2.5	63.6	0.2016	4.313	0.000	0.456	0.180
121.0	2.8704	84.3	2.5	63.6	0.2029	4.384	0.000	0.457	0.180
126.0	2.8812	84.4	2.5	63.5	0.2043	4.454	0.000	0.457	0.180
131.0	2.8919	84.4	2.5	63.4	0.2058	4.525	0.000	0.458	0.180
136.0	2.9028	84.5	2.5	63.3	0.2072	4.592	0.000	0.459	0.180
141.0	2.9143	84.5	2.5	63.2	0.2086	4.645	0.000	0.460	0.180
146.0	2.9257	84.6	2.6	63.1	0.2098	4.699	0.000	0.461	0.180
151.0	2.9372	84.6	2.6	63.1	0.2108	4.752	0.000	0.462	0.180
156.0	2.9487	84.7	2.6	63.0	0.2115	4.806	0.000	0.463	0.180
161.0	2.9602	84.8	2.6	63.0	0.2120	4.859	0.000	0.464	0.180
166.0	2.9716	84.9	2.6	63.0	0.2121	4.913	0.000	0.465	0.180
171.0	2.9745	85.0	2.6	63.0	0.2120	4.925	0.000	0.465	0.180
176.0	2.9773	85.1	2.6	63.0	0.2115	4.938	0.000	0.465	0.180
181.0	2.9802	85.2	2.6	63.1	0.2107	4.951	0.000	0.465	0.180
186.0	2.9830	85.3	2.6	63.1	0.2098	4.951	0.000	0.466	0.180
191.0	2.9859	85.4	2.7	63.2	0.2087	4.976	0.000	0.467	0.180
196.0	2.9887	85.6	2.7	63.3	0.2075	4.989	0.000	0.468	0.180
201.0	2.9795	85.7	2.7	63.4	0.2062	4.862	0.000	0.468	0.180
206.0	2.9703	85.9	2.7	63.4	0.2050	4.935	0.000	0.469	0.180
211.0	2.9611	86.1	2.7	63.5	0.2039	4.908	0.000	0.469	0.180
216.0	2.9519	86.3	2.7	63.6	0.2027	4.881	0.000	0.470	0.180
221.0	2.9426	86.4	2.7	63.6	0.2017	4.803	0.000	0.470	0.180
226.0	2.9334	86.6	2.7	63.7	0.2008	4.828	0.000	0.470	0.180
231.0	2.9284	86.8	2.7	63.8	0.1999	4.582	0.000	0.471	0.180
236.0	2.9245	87.0	2.7	63.8	0.1992	4.718	0.000	0.472	0.180
241.0	2.9205	87.2	2.7	63.8	0.1985	4.660	0.000	0.473	0.180
246.0	2.9166	87.5	2.7	63.9	0.1979	4.606	0.000	0.473	0.180
251.0	2.9126	87.7	2.7	63.9	0.1973	4.544	0.000	0.474	0.180
256.0	2.9087	87.9	2.7	64.0	0.1968	4.486	0.000	0.474	0.180
261.0	2.9121	88.1	2.7	64.0	0.1963	4.437	0.000	0.475	0.180
266.0	2.9205	88.3	2.7	64.0	0.1959	4.394	0.000	0.476	0.180
271.0	2.9289	88.5	2.7	64.0	0.1955	4.355	0.000	0.476	0.180
276.0	2.9372	88.7	2.7	64.1	0.1951	4.345	0.000	0.475	0.180

281.0	2.9456	88.9	2.7	64.1	0.1948	4.266	0.000	0.475	0.180
286.0	2.9540	89.1	2.7	64.1	0.1945	4.220	0.000	0.476	0.180
291.0	2.9687	89.3	2.7	64.1	0.1942	4.190	0.000	0.476	0.180
296.0	2.9877	89.5	2.7	64.1	0.1939	4.255	0.000	0.475	0.180
301.0	3.0066	89.7	2.7	64.2	0.1936	4.149	0.000	0.474	0.180
306.0	3.0256	89.8	2.7	64.2	0.1934	4.129	0.000	0.475	0.180
311.0	3.0446	90.0	2.7	64.2	0.1931	4.108	0.000	0.475	0.180
316.0	3.0636	90.1	2.8	64.2	0.1929	4.088	0.000	0.475	0.180
321.0	3.0721	90.3	2.8	64.2	0.1927	4.029	0.000	0.454	0.180
326.0	3.0649	90.4	2.8	64.2	0.1923	3.911	0.000	0.455	0.180
331.0	3.0577	90.5	2.8	64.2	0.1922	3.793	0.000	0.455	0.180
336.0	3.0506	90.6	2.8	64.2	0.1920	3.676	0.000	0.455	0.180
341.0	3.0434	90.7	2.9	64.3	0.1919	3.558	0.000	0.456	0.180
346.0	3.0362	90.8	2.9	64.3	0.1918	3.440	0.000	0.456	0.180
351.0	3.0315	90.8	2.9	64.3	0.1917	3.360	0.000	0.457	0.180
356.0	3.0306	90.8	3.0	64.3	0.1916	3.336	0.000	0.457	0.180
361.0	3.0297	90.8	3.0	64.3	0.1916	3.313	0.000	0.457	0.180

E. 2022 FULL YEAR 1200

yyyy/mmdd(or -ddd)/hh.h):2022/-366/12.0LT geog Lat/Long/Alt= 36.4/ 243.2/ 1.8

IRIcor2 is used for topside Ne profile
URSI maps are used for the F2 peak density (NmF2)
foF2 STORM model is turned on
Shubin2015model is used for F2 peak height (hmF2)
ABT-2009 option is used for the bottomside thickness parameter B0
Scotto-97 no L option is used for the F1 occurrence probability
foE auroral storm model is turned off
IRI-1990 option is used for D-region
TBT-2012 with solar dependence is used for the electron temperature
Tru-2021 option is used for the ion temperature
RBV10+TBT15 option is used for ion composition
CGM coordinates not computed
auroral boundaries not computed

Solar and magnetic parameter for the 1st profile point:
Solar Zenith Angle/degree 59.4
Dip (Magnetic Inclination)/degree 61.32
Modip (Modified Dip)/degree 50.03
Solar Sunspot Number (12-months running mean) Rz12 40.7
Ionospheric-Effective Solar Index IG12 37.3
Solar radio flux F10.7 (daily) 90.8
Solar radio flux F10.7 (81-day average) 101.3

TEC [1.E16 m-2] is obtained by numerical integration in 1km steps
from 50 to 1500.0 km. t is the percentage of TEC above the F peak.

-

DAYOF	M3000	B0	B1	E-VALLEY		PLASMA FREQUENCIES / MHz			
YEAR		km		W/km	Depth	foF2	foF1	foE	foD
1.0	3.3775	81.2	2.3	15.9	0.9080	7.825	0.000	3.058	0.205
6.0	3.3687	81.3	2.3	15.9	0.9081	7.797	0.000	3.070	0.208

11.0	3.3599	81.7	2.3	15.9	0.9082	7.768	0.000	3.090	0.211
16.0	3.3491	82.4	2.3	15.9	0.9083	8.084	0.000	3.115	0.216
21.0	3.3305	83.3	2.3	15.9	0.9085	7.806	0.000	3.138	0.220
26.0	3.3118	84.5	2.2	15.9	0.9087	7.856	0.000	3.162	0.225
31.0	3.2932	85.9	2.2	15.9	0.9089	7.906	0.000	3.186	0.230
36.0	3.2746	87.7	2.2	15.9	0.9091	8.367	0.000	3.214	0.235
41.0	3.2559	89.7	2.2	15.9	0.9093	8.147	0.000	3.242	0.239
46.0	3.2331	91.8	2.2	15.8	0.9095	8.060	0.000	3.273	0.244
51.0	3.1935	94.1	2.1	15.8	0.9536	8.165	4.479	3.301	0.247
56.0	3.1539	96.6	2.1	15.8	0.9538	8.195	4.515	3.329	0.251
61.0	3.1143	99.1	2.1	15.8	0.9540	8.262	4.550	3.359	0.254
66.0	3.0747	101.4	2.1	15.8	0.9542	8.329	4.584	3.386	0.257
71.0	3.0351	103.8	2.0	15.8	0.9543	8.450	4.616	3.411	0.260
76.0	2.9994	106.2	2.0	15.8	0.9545	8.401	4.647	3.438	0.263
81.0	2.9697	108.6	2.0	15.8	0.9546	8.312	4.676	3.463	0.265
86.0	2.9399	111.0	2.0	15.8	0.9548	8.219	4.704	3.486	0.267
91.0	2.9102	113.3	2.0	15.8	0.9549	8.127	4.730	3.506	0.269
96.0	2.8804	115.6	2.0	15.7	0.9550	8.045	4.754	3.528	0.270
101.0	2.8507	117.8	1.9	15.7	0.9551	7.956	4.776	3.548	0.272
106.0	2.8255	120.0	1.9	15.7	0.9552	7.857	4.796	3.564	0.273
111.0	2.8184	122.0	1.9	15.7	0.9552	7.718	4.816	3.579	0.274
116.0	2.8113	123.9	1.9	15.7	0.9553	7.579	4.834	3.590	0.276
121.0	2.8042	125.7	1.9	15.7	0.9554	7.439	4.851	3.601	0.277
126.0	2.7971	127.2	1.9	15.7	0.9554	7.300	4.866	3.611	0.278
131.0	2.7900	128.6	1.9	15.7	0.9555	7.161	4.880	3.621	0.279
136.0	2.7849	129.8	1.9	15.7	0.9555	7.042	4.893	3.630	0.280
141.0	2.7877	130.8	1.9	15.7	0.9555	7.003	4.903	3.638	0.281
146.0	2.7906	131.6	1.9	15.7	0.9556	6.965	4.912	3.645	0.281
151.0	2.7935	132.2	1.9	15.7	0.9556	6.926	4.920	3.650	0.282
156.0	2.7963	132.6	1.9	15.7	0.9556	6.888	4.927	3.656	0.283
161.0	2.7992	132.7	1.9	15.7	0.9556	6.849	4.934	3.661	0.283
166.0	2.8021	132.7	1.9	15.7	0.9556	6.776	4.939	3.666	0.284
171.0	2.8074	132.5	1.9	15.7	0.9556	6.858	4.944	3.667	0.284
176.0	2.8128	132.0	1.9	15.7	0.9556	6.906	4.947	3.666	0.285
181.0	2.8181	131.3	1.9	15.7	0.9556	6.953	4.950	3.666	0.285
186.0	2.8235	130.4	1.9	15.7	0.9556	7.001	4.952	3.667	0.285
191.0	2.8288	129.4	1.9	15.7	0.9556	7.048	4.953	3.668	0.286
196.0	2.8342	128.2	1.9	15.7	0.9556	7.096	4.954	3.668	0.286
201.0	2.8310	126.8	1.9	15.7	0.9555	7.233	4.954	3.665	0.286
206.0	2.8279	125.3	1.9	15.7	0.9555	7.370	4.952	3.664	0.286
211.0	2.8248	123.6	1.9	15.7	0.9555	7.507	4.950	3.660	0.287
216.0	2.8216	121.8	1.9	15.7	0.9554	7.644	4.946	3.655	0.287
221.0	2.8185	119.8	1.9	15.7	0.9554	7.716	4.941	3.647	0.287
226.0	2.8153	117.8	1.9	15.7	0.9553	7.918	4.935	3.640	0.287
231.0	2.8271	115.6	1.9	15.7	0.9553	8.021	4.926	3.632	0.287
236.0	2.8426	113.4	1.9	15.7	0.9552	8.354	4.916	3.624	0.286
241.0	2.8581	111.1	1.9	15.7	0.9551	8.582	4.903	3.615	0.286
246.0	2.8736	108.7	2.0	15.7	0.9550	8.762	4.889	3.604	0.285
251.0	2.8892	106.3	2.0	15.7	0.9549	9.037	4.873	3.590	0.285
256.0	2.9047	103.9	2.0	15.8	0.9548	9.263	4.855	3.573	0.284
261.0	2.9276	101.5	2.0	15.8	0.9547	9.491	4.835	3.558	0.283
266.0	2.9556	99.1	2.0	15.8	0.9545	9.719	4.812	3.541	0.281
271.0	2.9836	96.8	2.0	15.8	0.9544	9.947	4.788	3.519	0.280
276.0	3.0116	94.7	2.0	15.8	0.9542	10.128	4.762	3.492	0.278
281.0	3.0395	92.7	2.0	15.8	0.9541	10.402	4.734	3.469	0.275

286.0	3.0675	90.8	2.0	15.8	0.9539	10.630	4.705	3.448	0.273
291.0	3.0974	89.1	2.0	15.8	0.9537	10.784	0.000	3.423	0.270
296.0	3.1286	87.6	2.0	15.8	0.9535	11.269	0.000	3.393	0.267
301.0	3.1598	86.3	2.1	15.9	0.9532	10.995	0.000	3.364	0.263
306.0	3.1911	85.2	2.1	15.9	0.9530	11.100	0.000	3.339	0.259
311.0	3.2223	84.4	2.1	15.9	0.9528	11.697	0.000	3.314	0.255
316.0	3.2535	83.8	2.1	15.9	0.9526	11.310	0.000	3.289	0.250
321.0	3.2737	83.6	2.1	15.9	0.9524	11.326	0.000	3.202	0.246
326.0	3.2774	83.7	2.1	15.9	0.9084	11.209	0.000	3.182	0.241
331.0	3.2810	84.2	2.1	15.9	0.9082	11.091	0.000	3.165	0.237
336.0	3.2847	85.0	2.1	15.9	0.9081	10.973	0.000	3.150	0.234
341.0	3.2884	86.2	2.1	15.9	0.9080	10.855	0.000	3.139	0.231
346.0	3.2920	87.8	2.1	16.0	0.9079	10.738	0.000	3.131	0.228
351.0	3.2905	89.8	2.1	16.0	0.9079	10.657	0.000	3.126	0.227
356.0	3.2812	92.2	2.1	16.0	0.9079	10.633	0.000	3.126	0.227
361.0	3.2718	95.1	2.1	16.0	0.9079	10.609	0.000	3.130	0.228

APPENDIX D. STORE GLACIER GREENLAND IRI 2020 DATA FOR MATLAB MODELING

A. 20MAR2022 FULL DAY

yyyy/mmdd(or -ddd)/hh.h):2022/ 320/ 0.0LT geog Lat/Long/Alt= 70.3/ 310.2/ 100.0

IRIcor2 is used for topside Ne profile
URSI maps are used for the F2 peak density (NmF2)
foF2 STORM model is turned on
Shubin2015model is used for F2 peak height (hmF2)
ABT-2009 option is used for the bottomside thickness parameter B0
Scotto-97 no L option is used for the F1 occurrence probability
foE auroral storm model is turned off
IRI-1990 option is used for D-region
TBT-2012 with solar dependence is used for the electron temperature
Tru-2021 option is used for the ion temperature
RBV10+TBT15 option is used for ion composition
CGM coordinates not computed
auroral boundaries not computed

Solar and magnetic parameter for the 1st profile point:
Solar Zenith Angle/degree 109.2
Dip (Magnetic Inclination)/degree 81.02
Modip (Modified Dip)/degree 67.70
Solar Sunspot Number (12-months running mean) Rz12 48.6
Ionospheric-Effective Solar Index IG12 46.9
Solar radio flux F10.7 (daily) 94.1
Solar radio flux F10.7 (81-day average) 118.9

TEC [1.E16 m-2] is obtained by numerical integration in 1km steps
from 50 to 1500.0 km. t is the percentage of TEC above the F peak.

-

HOUR	M3000	B0	B1	E-VALLEY		PLASMA FREQUENCIES / MHz			
L.T.		km		W/km	Depth	foF2	foF1	foE	foD
1.0	2.8651	102.9	1.6	62.9	0.2464	2.990	0.000	0.448	0.180
2.0	2.8766	106.9	1.7	57.7	0.3264	2.948	0.000	0.448	0.180
3.0	2.9044	111.6	1.7	48.2	0.4742	2.971	0.000	0.448	0.180
4.0	2.9448	116.3	1.8	36.1	0.6614	3.071	0.000	0.550	0.180
5.0	2.9900	120.3	1.8	26.4	0.8112	3.261	0.000	0.824	0.180
6.0	3.0317	123.3	1.8	21.1	0.8931	3.555	0.000	1.252	0.180
7.0	3.0637	125.8	1.8	18.8	0.9288	3.934	0.000	1.707	0.180
8.0	3.0824	128.4	1.7	17.9	0.9428	4.336	0.000	2.052	0.180
9.0	3.0863	131.2	1.7	17.6	0.9480	4.674	0.000	2.287	0.180
10.0	3.0759	133.9	1.7	17.5	0.9500	4.894	0.000	2.440	0.180
11.0	3.0553	136.4	1.6	17.4	0.9507	5.003	0.000	2.529	0.180
12.0	3.0322	138.6	1.6	17.4	0.9509	5.054	0.000	2.563	0.180
13.0	3.0156	140.2	1.6	17.4	0.9508	5.090	0.000	2.544	0.180
14.0	3.0103	140.9	1.6	17.5	0.9502	5.113	0.000	2.470	0.180
15.0	3.0138	140.2	1.5	17.6	0.9488	5.091	0.000	2.336	0.180
16.0	3.0176	137.4	1.5	17.8	0.9448	4.988	0.000	2.128	0.180

17.0	3.0126	132.3	1.5	18.5	0.9343	4.790	0.000	1.817	0.180
18.0	2.9954	125.4	1.4	20.2	0.9073	4.513	0.000	1.388	0.180
19.0	2.9694	117.9	1.4	24.4	0.8430	4.194	0.000	0.937	0.180
20.0	2.9414	110.9	1.4	32.6	0.7155	3.875	0.000	0.617	0.180
21.0	2.9167	105.3	1.4	44.3	0.5337	3.596	0.000	0.448	0.180
22.0	2.8965	101.5	1.4	55.1	0.3675	3.375	0.000	0.448	0.180
23.0	2.8799	99.8	1.5	61.5	0.2669	3.208	0.000	0.448	0.180
24.0	2.8680	100.4	1.5	64.5	0.2203	3.081	0.000	0.448	0.180

B. 21JUN2022 FULL DAY

yyyy/mmdd(or -ddd)/hh.h):2022/ 621/ 0.0LT geog Lat/Long/Alt= 70.3/ 310.2/ 100.0

IRIcor2 is used for topside Ne profile
URSI maps are used for the F2 peak density (NmF2)
foF2 STORM model is turned on
Shubin2015model is used for F2 peak height (hmF2)
ABT-2009 option is used for the bottomside thickness parameter B0
Scotto-97 no L option is used for the F1 occurrence probability
foE auroral storm model is turned off
IRI-1990 option is used for D-region
TBT-2012 with solar dependence is used for the electron temperature
Tru-2021 option is used for the ion temperature
RBV10+TBT15 option is used for ion composition
CGM coordinates not computed
auroral boundaries not computed

Solar and magnetic parameter for the 1st profile point:
Solar Zenith Angle/degree 85.7
Dip (Magnetic Inclination)/degree 81.02
Modip (Modified Dip)/degree 67.70
Solar Sunspot Number (12-months running mean) Rz12 57.9
Ionospheric-Effective Solar Index IG12 66.6
Solar radio flux F10.7 (daily) 143.2
Solar radio flux F10.7 (81-day average) 130.0

TEC [1.E16 m-2] is obtained by numerical integration in 1km steps
from 50 to 1500.0 km. t is the percentage of TEC above the F peak.

-

HOUR	M3000	B0	B1	E-VALLEY		PLASMA FREQUENCIES / MHz			
L.T.		km		W/km	Depth	foF2	foF1	foE	foD
1.0	2.9733	118.7	1.4	17.4	0.9511	4.544	0.000	1.714	0.180
2.0	2.9476	125.6	1.5	17.4	0.9511	4.544	0.000	1.853	0.180
3.0	2.9354	133.6	1.5	17.4	0.9511	4.548	0.000	2.050	0.180
4.0	2.9381	141.3	1.5	17.4	0.9511	4.569	0.000	2.265	0.180
5.0	2.9436	147.6	1.5	17.4	0.9511	4.631	0.000	2.471	0.180
6.0	2.9356	151.6	1.5	17.4	0.9511	4.740	0.000	2.657	0.180
7.0	2.9070	153.6	1.5	17.4	0.9511	4.863	0.000	2.817	0.196
8.0	2.8641	154.9	1.5	17.4	0.9511	4.958	4.153	2.949	0.226
9.0	2.8214	156.6	1.6	17.4	0.9511	5.018	4.230	3.053	0.244
10.0	2.7910	159.2	1.6	17.4	0.9511	5.078	4.285	3.127	0.254

11.0	2.7768	162.5	1.6	17.4	0.9511	5.166	4.318	3.172	0.259
12.0	2.7762	166.1	1.5	17.4	0.9511	5.254	4.329	3.188	0.261
13.0	2.7858	169.5	1.5	17.4	0.9511	5.297	4.319	3.174	0.259
14.0	2.8043	171.9	1.5	17.4	0.9511	5.290	4.287	3.130	0.254
15.0	2.8308	172.1	1.4	17.4	0.9511	5.273	4.233	3.057	0.244
16.0	2.8610	169.0	1.4	17.4	0.9511	5.272	4.157	2.955	0.227
17.0	2.8888	161.8	1.4	17.4	0.9511	5.264	0.000	2.824	0.197
18.0	2.9106	150.9	1.3	17.4	0.9511	5.216	0.000	2.666	0.180
19.0	2.9287	138.4	1.3	17.4	0.9511	5.121	0.000	2.481	0.180
20.0	2.9494	127.0	1.3	17.4	0.9511	4.996	0.000	2.276	0.180
21.0	2.9748	118.4	1.3	17.4	0.9511	4.859	0.000	2.061	0.180
22.0	2.9986	113.4	1.3	17.4	0.9511	4.727	0.000	1.862	0.180
23.0	3.0090	112.0	1.4	17.4	0.9511	4.622	0.000	1.718	0.180
24.0	2.9988	114.0	1.4	17.4	0.9511	4.563	0.000	1.665	0.180

C. 22SEP2022 FULL DAY

yyyy/mmdd(or -ddd)/hh.h):2022/ 922/ 0.0LT geog Lat/Long/Alt= 70.3/ 310.2/ 100.0

IRIcor2 is used for topside Ne profile
URSI maps are used for the F2 peak density (NmF2)
foF2 STORM model is turned on
Shubin2015model is used for F2 peak height (hmF2)
ABT-2009 option is used for the bottomside thickness parameter B0
Scotto-97 no L option is used for the F1 occurrence probability
foE auroral storm model is turned off
IRI-1990 option is used for D-region
TBT-2012 with solar dependence is used for the electron temperature
Tru-2021 option is used for the ion temperature
RBV10+TBT15 option is used for ion composition
CGM coordinates not computed
auroral boundaries not computed

Solar and magnetic parameter for the 1st profile point:
Solar Zenith Angle/degree 108.6
Dip (Magnetic Inclination)/degree 81.01
Modip (Modified Dip)/degree 67.69
Solar Sunspot Number (12-months running mean) Rz12 65.0
Ionospheric-Effective Solar Index IG12 88.1
Solar radio flux F10.7 (daily) 137.7
Solar radio flux F10.7 (81-day average) 132.6

TEC [1.E16 m-2] is obtained by numerical integration in 1km steps
from 50 to 1500.0 km. t is the percentage of TEC above the F peak.

-

HOUR	M3000	B0	B1	E-VALLEY		PLASMA FREQUENCIES / MHz			
L.T.		km		W/km	Depth	foF2	foF1	foE	foD
1.0	2.9249	84.7	1.6	61.6	0.2658	3.819	0.000	0.476	0.180
2.0	2.9339	86.9	1.7	55.2	0.3655	3.719	0.000	0.476	0.180
3.0	2.9507	90.2	1.7	44.5	0.5310	3.696	0.000	0.476	0.180
4.0	2.9752	93.9	1.8	32.8	0.7132	3.784	0.000	0.631	0.180
5.0	3.0042	97.5	1.8	24.5	0.8417	4.012	0.000	0.957	0.180

6.0	3.0323	100.4	1.7	20.3	0.9067	4.388	0.000	1.421	0.180
7.0	3.0538	102.8	1.7	18.5	0.9341	4.870	0.000	1.862	0.180
8.0	3.0641	105.2	1.7	17.8	0.9447	5.357	0.000	2.182	0.180
9.0	3.0618	108.1	1.6	17.6	0.9488	5.747	0.000	2.397	0.180
10.0	3.0488	111.4	1.6	17.5	0.9502	5.985	0.000	2.535	0.180
11.0	3.0299	115.0	1.6	17.4	0.9507	6.077	0.000	2.611	0.180
12.0	3.0116	118.6	1.6	17.4	0.9509	6.074	0.000	2.630	0.180
13.0	2.9998	121.7	1.6	17.4	0.9507	6.029	0.000	2.596	0.180
14.0	2.9968	123.9	1.6	17.5	0.9500	5.974	0.000	2.504	0.180
15.0	3.0004	124.6	1.6	17.6	0.9480	5.898	0.000	2.347	0.180
16.0	3.0049	123.0	1.6	17.9	0.9427	5.768	0.000	2.106	0.180
17.0	3.0040	118.8	1.6	18.9	0.9286	5.563	0.000	1.751	0.180
18.0	2.9946	112.6	1.5	21.2	0.8927	5.300	0.000	1.283	0.180
19.0	2.9780	105.4	1.4	26.5	0.8104	5.018	0.000	0.845	0.180
20.0	2.9589	98.4	1.4	36.2	0.6600	4.750	0.000	0.564	0.180
21.0	2.9422	92.4	1.4	48.3	0.4729	4.514	0.000	0.476	0.180
22.0	2.9306	87.9	1.4	57.8	0.3256	4.311	0.000	0.476	0.180
23.0	2.9242	85.1	1.4	62.9	0.2460	4.131	0.000	0.476	0.180
24.0	2.9222	84.1	1.5	65.1	0.2115	3.965	0.000	0.476	0.180

D. 2022 FULL YEAR 0000

yyyy/mmdd(or -ddd)/hh.h):2022/-366/ 0.0LT geog Lat/Long/Alt= 70.3/ 310.0/ 100.0

IRIcor2 is used for topside Ne profile
URSI maps are used for the F2 peak density (NmF2)
foF2 STORM model is turned on
Shubin2015model is used for F2 peak height (hmF2)
ABT-2009 option is used for the bottomside thickness parameter B0
Scotto-97 no L option is used for the F1 occurrence probability
foE auroral storm model is turned off
IRI-1990 option is used for D-region
TBT-2012 with solar dependence is used for the electron temperature
Tru-2021 option is used for the ion temperature
RBV10+TBT15 option is used for ion composition
CGM coordinates not computed
auroral boundaries not computed

Solar and magnetic parameter for the 1st profile point:
Solar Zenith Angle/degree 132.7
Dip (Magnetic Inclination)/degree 81.05
Modip (Modified Dip)/degree 67.70
Solar Sunspot Number (12-months running mean) Rz12 40.7
Ionospheric-Effective Solar Index IG12 37.3
Solar radio flux F10.7 (daily) 90.8
Solar radio flux F10.7 (81-day average) 101.3

TEC [1.E16 m-2] is obtained by numerical integration in 1km steps
from 50 to 1500.0 km. t is the percentage of TEC above the F peak.

-

DAYOF	M3000	B0	B1	E-VALLEY		PLASMA FREQUENCIES / MHz			
YEAR		km		W/km	Depth	foF2	foF1	foE	foD
1.0	2.9813	76.1	1.7	66.5	0.1902	2.780	0.000	0.431	0.180

6.0	2.9756	76.8	1.7	66.5	0.1902	2.793	0.000	0.432	0.180
11.0	2.9698	77.7	1.7	66.5	0.1903	2.807	0.000	0.434	0.180
16.0	2.9638	78.8	1.7	66.5	0.1903	2.903	0.000	0.436	0.180
21.0	2.9565	79.9	1.7	66.5	0.1904	2.817	0.000	0.437	0.180
26.0	2.9493	81.3	1.7	66.5	0.1905	2.849	0.000	0.438	0.180
31.0	2.9420	82.7	1.7	66.5	0.1906	2.818	0.000	0.438	0.180
36.0	2.9348	84.4	1.7	66.4	0.1908	2.810	0.000	0.439	0.180
41.0	2.9276	86.2	1.6	66.4	0.1911	2.818	0.000	0.440	0.180
46.0	2.9198	88.0	1.6	66.4	0.1915	2.825	0.000	0.441	0.180
51.0	2.9101	90.0	1.6	66.4	0.1922	2.855	0.000	0.442	0.180
56.0	2.9004	92.0	1.6	66.3	0.1932	2.886	0.000	0.442	0.180
61.0	2.8906	93.9	1.6	66.2	0.1946	2.917	0.000	0.444	0.180
66.0	2.8809	95.7	1.6	66.1	0.1969	3.019	0.000	0.445	0.180
71.0	2.8712	97.6	1.6	65.8	0.2004	2.999	0.000	0.445	0.180
76.0	2.8665	99.3	1.5	65.5	0.2063	3.030	0.000	0.447	0.180
81.0	2.8695	101.1	1.5	64.8	0.2164	3.116	0.000	0.448	0.180
86.0	2.8726	102.8	1.5	63.6	0.2349	3.201	0.000	0.449	0.180
91.0	2.8756	104.4	1.5	61.2	0.2725	3.200	0.000	0.450	0.180
96.0	2.8786	106.0	1.5	54.9	0.3700	3.372	0.000	0.452	0.180
101.0	2.8816	107.5	1.5	17.4	0.9511	3.345	0.000	0.508	0.180
106.0	2.8853	108.9	1.5	17.4	0.9511	3.458	0.000	0.587	0.180
111.0	2.8921	110.2	1.5	17.4	0.9511	3.638	0.000	0.682	0.180
116.0	2.8989	111.4	1.5	17.4	0.9511	3.731	0.000	0.790	0.180
121.0	2.9056	112.4	1.4	17.4	0.9511	3.803	0.000	0.907	0.180
126.0	2.9124	113.3	1.4	17.4	0.9511	3.919	0.000	1.029	0.180
131.0	2.9191	114.1	1.4	17.4	0.9511	4.013	0.000	1.151	0.180
136.0	2.9274	114.6	1.4	17.4	0.9511	4.104	0.000	1.265	0.180
141.0	2.9418	115.0	1.4	17.4	0.9511	4.184	0.000	1.368	0.180
146.0	2.9562	115.3	1.4	17.4	0.9511	4.264	0.000	1.457	0.180
151.0	2.9706	115.4	1.4	17.4	0.9511	4.345	0.000	1.530	0.180
156.0	2.9850	115.3	1.4	17.4	0.9511	4.425	0.000	1.587	0.180
161.0	2.9994	115.1	1.4	17.4	0.9511	4.506	0.000	1.628	0.180
166.0	3.0138	114.7	1.4	17.4	0.9511	4.586	0.000	1.654	0.180
171.0	3.0014	114.1	1.4	17.4	0.9511	4.566	0.000	1.665	0.180
176.0	2.9890	113.4	1.4	17.4	0.9511	4.546	0.000	1.660	0.180
181.0	2.9767	112.4	1.4	17.4	0.9511	4.526	0.000	1.641	0.180
186.0	2.9643	111.4	1.4	17.4	0.9511	4.438	0.000	1.608	0.180
191.0	2.9519	110.3	1.4	17.4	0.9511	4.485	0.000	1.560	0.180
196.0	2.9395	109.0	1.4	17.4	0.9511	4.465	0.000	1.497	0.180
201.0	2.9390	107.6	1.4	17.4	0.9511	4.193	0.000	1.417	0.180
206.0	2.9384	106.1	1.4	17.4	0.9511	4.392	0.000	1.323	0.180
211.0	2.9379	104.4	1.4	17.4	0.9511	4.356	0.000	1.215	0.180
216.0	2.9374	102.7	1.4	17.4	0.9511	4.319	0.000	1.098	0.180
221.0	2.9368	101.0	1.4	17.4	0.9511	4.045	0.000	0.976	0.180
226.0	2.9363	99.1	1.5	17.4	0.9511	4.246	0.000	0.856	0.180
231.0	2.9367	97.2	1.5	17.4	0.9511	3.876	0.000	0.744	0.180
236.0	2.9373	95.3	1.5	17.4	0.9511	4.148	0.000	0.642	0.180
241.0	2.9378	93.3	1.5	17.4	0.9511	4.098	0.000	0.556	0.180
246.0	2.9384	91.4	1.5	17.4	0.9511	4.046	0.000	0.485	0.180
251.0	2.9390	89.4	1.5	58.1	0.3203	3.992	0.000	0.474	0.180
256.0	2.9396	87.4	1.5	61.9	0.2606	3.947	0.000	0.474	0.180
261.0	2.9324	85.5	1.5	63.7	0.2327	3.943	0.000	0.475	0.180
266.0	2.9201	83.7	1.5	64.7	0.2174	3.971	0.000	0.476	0.180
271.0	2.9077	82.0	1.5	65.3	0.2083	4.056	0.000	0.476	0.180
276.0	2.8954	80.4	1.5	65.7	0.2026	4.039	0.000	0.475	0.180

281.0	2.8830	79.0	1.5	65.9	0.1988	4.096	0.000	0.475	0.180
286.0	2.8707	77.8	1.6	66.1	0.1963	4.080	0.000	0.476	0.180
291.0	2.8679	76.7	1.6	66.2	0.1945	4.121	0.000	0.476	0.180
296.0	2.8714	75.8	1.6	66.3	0.1933	4.160	0.000	0.475	0.180
301.0	2.8750	75.1	1.6	66.3	0.1924	4.222	0.000	0.474	0.180
306.0	2.8786	74.6	1.6	66.4	0.1918	4.272	0.000	0.475	0.180
311.0	2.8821	74.4	1.6	66.4	0.1913	4.322	0.000	0.475	0.180
316.0	2.8857	74.4	1.6	66.4	0.1910	4.372	0.000	0.475	0.180
321.0	2.8888	74.8	1.6	66.5	0.1908	4.390	0.000	0.454	0.180
326.0	2.8911	75.5	1.6	66.5	0.1906	4.360	0.000	0.455	0.180
331.0	2.8934	76.5	1.6	66.5	0.1904	4.330	0.000	0.455	0.180
336.0	2.8958	78.0	1.7	66.5	0.1904	4.300	0.000	0.455	0.180
341.0	2.8981	79.7	1.7	66.5	0.1903	4.270	0.000	0.456	0.180
346.0	2.9004	81.8	1.7	66.5	0.1903	4.240	0.000	0.456	0.180
351.0	2.8996	84.3	1.7	66.5	0.1902	4.221	0.000	0.457	0.180
356.0	2.8940	87.2	1.7	66.5	0.1902	4.220	0.000	0.457	0.180
361.0	2.8883	90.4	1.7	66.5	0.1902	4.219	0.000	0.457	0.180

E. 2022 FULL YEAR 1200

yyyy/mmdd(or -ddd)/hh.h):2022/-366/12.0LT geog Lat/Long/Alt= 70.3/ 310.0/ 100.0

IRIcor2 is used for topside Ne profile
URSI maps are used for the F2 peak density (NmF2)
foF2 STORM model is turned on
Shubin2015model is used for F2 peak height (hmF2)
ABT-2009 option is used for the bottomside thickness parameter B0
Scotto-97 no L option is used for the F1 occurrence probability
foE auroral storm model is turned off
IRI-1990 option is used for D-region
TBT-2012 with solar dependence is used for the electron temperature
Tru-2021 option is used for the ion temperature
RBV10+TBT15 option is used for ion composition
CGM coordinates not computed
auroral boundaries not computed

Solar and magnetic parameter for the 1st profile point:
Solar Zenith Angle/degree 93.3
Dip (Magnetic Inclination)/degree 81.05
Modip (Modified Dip)/degree 67.70
Solar Sunspot Number (12-months running mean) Rz12 40.7
Ionospheric-Effective Solar Index IG12 37.3
Solar radio flux F10.7 (daily) 90.8
Solar radio flux F10.7 (81-day average) 101.3

TEC [1.E16 m-2] is obtained by numerical integration in 1km steps
from 50 to 1500.0 km. t is the percentage of TEC above the F peak.

-

DAYOF	M3000	B0	B1	E-VALLEY		PLASMA FREQUENCIES / MHz			
YEAR		km		W/km	Depth	foF2	foF1	foE	foD
1.0	3.2968	93.4	1.8	19.2	0.8768	4.475	0.000	1.137	0.180
6.0	3.3021	94.8	1.8	19.0	0.8796	4.513	0.000	1.189	0.180

11.0	3.3073	96.4	1.8	18.7	0.8828	4.551	0.000	1.262	0.180
16.0	3.3099	98.4	1.8	18.5	0.8861	4.812	0.000	1.357	0.180
21.0	3.3016	100.6	1.7	18.3	0.8892	4.665	0.000	1.469	0.180
26.0	3.2934	103.1	1.7	18.1	0.8920	4.735	0.000	1.453	0.180
31.0	3.2851	105.8	1.7	17.9	0.8943	4.805	0.000	1.563	0.180
36.0	3.2768	108.9	1.7	17.8	0.8963	5.110	0.000	1.684	0.180
41.0	3.2686	112.2	1.7	17.7	0.8978	4.946	0.000	1.809	0.180
46.0	3.2551	115.7	1.7	17.6	0.8990	5.004	0.000	1.931	0.180
51.0	3.2208	119.3	1.7	17.6	0.9486	5.071	0.000	2.046	0.180
56.0	3.1865	123.0	1.7	17.5	0.9494	5.024	0.000	2.154	0.180
61.0	3.1522	126.7	1.7	17.5	0.9499	5.034	0.000	2.257	0.180
66.0	3.1180	130.0	1.6	17.5	0.9503	5.044	0.000	2.350	0.180
71.0	3.0837	133.4	1.6	17.4	0.9506	5.134	0.000	2.436	0.180
76.0	3.0505	136.6	1.6	17.4	0.9508	5.057	0.000	2.517	0.180
81.0	3.0190	139.9	1.6	17.4	0.9509	5.049	0.000	2.592	0.180
86.0	2.9875	143.0	1.6	17.4	0.9510	5.041	0.000	2.660	0.180
91.0	2.9561	146.0	1.6	17.4	0.9511	5.032	0.000	2.723	0.180
96.0	2.9246	149.0	1.6	17.4	0.9511	5.024	0.000	2.783	0.185
101.0	2.8931	151.8	1.6	17.4	0.9511	5.000	0.000	2.838	0.199
106.0	2.8660	154.4	1.6	17.4	0.9511	5.019	0.000	2.886	0.211
111.0	2.8562	156.8	1.6	17.4	0.9511	5.069	4.112	2.931	0.220
116.0	2.8464	159.0	1.6	17.4	0.9511	5.119	4.145	2.970	0.228
121.0	2.8366	161.0	1.5	17.4	0.9511	5.168	4.175	3.006	0.234
126.0	2.8268	162.7	1.5	17.4	0.9511	5.218	4.203	3.038	0.240
131.0	2.8170	164.2	1.5	17.4	0.9511	5.268	4.227	3.068	0.245
136.0	2.8082	165.4	1.5	17.4	0.9511	5.306	4.249	3.095	0.248
141.0	2.8038	166.3	1.5	17.4	0.9511	5.290	4.268	3.118	0.251
146.0	2.7993	167.0	1.5	17.4	0.9511	5.290	4.284	3.137	0.254
151.0	2.7949	167.4	1.5	17.4	0.9511	5.282	4.297	3.153	0.256
156.0	2.7904	167.5	1.5	17.4	0.9511	5.274	4.309	3.166	0.258
161.0	2.7860	167.4	1.5	17.4	0.9511	5.266	4.317	3.177	0.259
166.0	2.7815	167.0	1.5	17.4	0.9511	5.215	4.324	3.185	0.260
171.0	2.7768	166.3	1.5	17.4	0.9511	5.255	4.328	3.188	0.261
176.0	2.7720	165.3	1.5	17.4	0.9511	5.252	4.330	3.186	0.261
181.0	2.7672	164.1	1.6	17.4	0.9511	5.249	4.329	3.183	0.261
186.0	2.7625	162.6	1.6	17.4	0.9511	5.246	4.327	3.178	0.260
191.0	2.7577	161.0	1.6	17.4	0.9511	5.243	4.322	3.170	0.260
196.0	2.7530	159.1	1.6	17.4	0.9511	5.239	4.314	3.160	0.258
201.0	2.7672	157.0	1.6	17.4	0.9511	5.217	4.305	3.145	0.257
206.0	2.7815	154.7	1.6	17.4	0.9511	5.295	4.293	3.128	0.255
211.0	2.7957	152.3	1.6	17.4	0.9511	5.323	4.278	3.107	0.252
216.0	2.8100	149.7	1.6	17.4	0.9511	5.350	4.261	3.081	0.249
221.0	2.8242	146.9	1.6	17.4	0.9511	5.134	4.241	3.051	0.244
226.0	2.8385	144.0	1.6	17.4	0.9511	5.406	4.217	3.019	0.239
231.0	2.8587	141.0	1.6	17.4	0.9511	5.241	4.190	2.984	0.232
236.0	2.8803	137.9	1.6	17.4	0.9511	5.530	0.000	2.946	0.224
241.0	2.9019	134.7	1.6	17.4	0.9511	5.595	0.000	2.904	0.213
246.0	2.9235	131.4	1.6	17.4	0.9511	5.580	0.000	2.857	0.201
251.0	2.9452	128.0	1.6	17.4	0.9511	5.710	0.000	2.804	0.185
256.0	2.9668	124.6	1.6	17.4	0.9510	5.792	0.000	2.746	0.180
261.0	2.9907	121.2	1.6	17.4	0.9509	5.927	0.000	2.684	0.180
266.0	3.0161	117.9	1.6	17.4	0.9508	6.109	0.000	2.616	0.180
271.0	3.0414	114.6	1.6	17.4	0.9507	6.290	0.000	2.540	0.180
276.0	3.0668	111.5	1.6	17.4	0.9504	6.577	0.000	2.455	0.180
281.0	3.0922	108.5	1.6	17.5	0.9501	6.653	0.000	2.367	0.180

286.0	3.1176	105.7	1.6	17.5	0.9496	6.835	0.000	2.272	0.180
291.0	3.1349	103.0	1.6	17.5	0.9490	6.942	0.000	2.168	0.180
296.0	3.1467	100.5	1.6	17.6	0.9482	7.292	0.000	2.053	0.180
301.0	3.1586	98.1	1.6	17.7	0.9470	7.057	0.000	1.933	0.180
306.0	3.1705	96.0	1.6	17.8	0.9456	7.115	0.000	1.810	0.180
311.0	3.1823	94.1	1.6	17.9	0.9438	7.173	0.000	1.686	0.180
316.0	3.1942	92.5	1.6	18.0	0.9415	7.230	0.000	1.567	0.180
321.0	3.2005	91.2	1.6	18.2	0.9389	7.232	0.000	1.440	0.180
326.0	3.1984	90.3	1.6	18.4	0.8879	7.150	0.000	1.448	0.180
331.0	3.1964	89.6	1.6	18.6	0.8847	7.067	0.000	1.345	0.180
336.0	3.1943	89.4	1.5	18.8	0.8815	6.985	0.000	1.261	0.180
341.0	3.1923	89.5	1.5	19.0	0.8785	6.903	0.000	1.197	0.180
346.0	3.1902	90.0	1.5	19.2	0.8760	6.820	0.000	1.153	0.180
351.0	3.1904	90.8	1.5	19.3	0.8744	6.777	0.000	1.127	0.180
356.0	3.1941	92.1	1.5	19.3	0.8740	6.794	0.000	1.121	0.180
361.0	3.1977	93.7	1.5	19.3	0.8748	6.811	0.000	1.134	0.180

APPENDIX E. MCMURDO STATION, ANTARCTICA IRI 2020 DATA FOR MATLAB MODELING

A. 20MAR2022 FULL DAY

yyyy/mmdd(or -ddd)/hh.h):2022/ 320/ 0.0LT geog Lat/Long/Alt=-77.8/ 166.7/ 100.0

IRIcor2 is used for topside Ne profile
URSI maps are used for the F2 peak density (NmF2)
foF2 STORM model is turned on
Shubin2015model is used for F2 peak height (hmF2)
ABT-2009 option is used for the bottomside thickness parameter B0
Scotto-97 no L option is used for the F1 occurrence probability
foE auroral storm model is turned off
IRI-1990 option is used for D-region
TBT-2012 with solar dependence is used for the electron temperature
Tru-2021 option is used for the ion temperature
RBV10+TBT15 option is used for ion composition
CGM coordinates not computed
auroral boundaries not computed

Solar and magnetic parameter for the 1st profile point:
Solar Zenith Angle/degree 101.9
Dip (Magnetic Inclination)/degree -80.65
Modip (Modified Dip)/degree -71.94
Solar Sunspot Number (12-months running mean) Rz12 48.6
Ionospheric-Effective Solar Index IG12 46.9
Solar radio flux F10.7 (daily) 94.1
Solar radio flux F10.7 (81-day average) 118.9

TEC [1.E16 m-2] is obtained by numerical integration in 1km steps
from 50 to 1500.0 km. t is the percentage of TEC above the F peak.

-

HOUR	M3000	B0	B1	E-VALLEY		PLASMA FREQUENCIES / MHz			
L.T.		km		W/km	Depth	foF2	foF1	foE	foD
1.0	2.9110	90.5	0.9	17.5	0.9507	3.374	0.000	0.473	0.180
2.0	2.9326	90.0	1.0	17.5	0.9507	3.353	0.000	0.515	0.180
3.0	2.9614	89.7	1.0	17.5	0.9507	3.449	0.000	0.600	0.180
4.0	2.9948	89.7	1.1	17.5	0.9507	3.651	0.000	0.745	0.180
5.0	3.0295	90.1	1.1	17.5	0.9507	3.936	0.000	0.959	0.180
6.0	3.0614	91.0	1.1	17.5	0.9507	4.272	0.000	1.230	0.180
7.0	3.0859	92.4	1.1	17.5	0.9507	4.610	0.000	1.511	0.180
8.0	3.0994	94.6	1.1	17.5	0.9507	4.908	0.000	1.751	0.180
9.0	3.1009	97.3	1.1	17.5	0.9507	5.135	0.000	1.931	0.180
10.0	3.0918	100.4	1.1	17.5	0.9507	5.283	0.000	2.053	0.180
11.0	3.0748	103.2	1.1	17.5	0.9507	5.364	0.000	2.126	0.180
12.0	3.0524	105.2	1.1	17.5	0.9507	5.397	0.000	2.153	0.180
13.0	3.0268	106.1	1.0	17.5	0.9507	5.396	0.000	2.135	0.180
14.0	2.9999	105.8	1.0	17.5	0.9507	5.365	0.000	2.072	0.180
15.0	2.9747	104.6	1.0	17.5	0.9506	5.307	0.000	1.960	0.180
16.0	2.9545	102.8	1.0	17.6	0.9504	5.226	0.000	1.792	0.180

17.0	2.9410	100.6	1.0	17.6	0.9497	5.120	0.000	1.562	0.180
18.0	2.9331	98.5	1.0	17.7	0.9477	4.980	0.000	1.284	0.180
19.0	2.9274	96.7	1.0	18.1	0.9424	4.797	0.000	1.003	0.180
20.0	2.9202	95.1	0.9	19.0	0.9278	4.570	0.000	0.773	0.180
21.0	2.9107	93.8	0.9	21.5	0.8898	4.307	0.000	0.614	0.180
22.0	2.9011	92.7	0.9	27.2	0.8018	4.020	0.000	0.518	0.180
23.0	2.8957	91.8	0.9	37.4	0.6428	3.740	0.000	0.468	0.180
24.0	2.8985	91.1	0.9	49.7	0.4525	3.510	0.000	0.450	0.180

B. 21JUN2022 FULL DAY

yyyy/mmdd(or -ddd)/hh.h):2022/ 621/ 0.0LT geog Lat/Long/Alt=-77.8/ 166.7/ 100.0

IRIcor2 is used for topside Ne profile
URSI maps are used for the F2 peak density (NmF2)
foF2 STORM model is turned on
Shubin2015model is used for F2 peak height (hmF2)
ABT-2009 option is used for the bottomside thickness parameter B0
Scotto-97 no L option is used for the F1 occurrence probability
foE auroral storm model is turned off
IRI-1990 option is used for D-region
TBT-2012 with solar dependence is used for the electron temperature
Tru-2021 option is used for the ion temperature
RBV10+TBT15 option is used for ion composition
CGM coordinates not computed
auroral boundaries not computed

Solar and magnetic parameter for the 1st profile point:
Solar Zenith Angle/degree 125.1
Dip (Magnetic Inclination)/degree -80.64
Modip (Modified Dip)/degree -71.94
Solar Sunspot Number (12-months running mean) Rz12 57.9
Ionospheric-Effective Solar Index IG12 66.6
Solar radio flux F10.7 (daily) 143.2
Solar radio flux F10.7 (81-day average) 130.0

TEC [1.E16 m-2] is obtained by numerical integration in 1km steps
from 50 to 1500.0 km. t is the percentage of TEC above the F peak.

-

HOUR	M3000	B0	B1	E-VALLEY		PLASMA FREQUENCIES / MHz			
L.T.		km		W/km	Depth	foF2	foF1	foE	foD
1.0	2.9639	71.8	1.0	66.7	0.1901	3.043	0.000	0.465	0.180
2.0	2.9806	69.8	1.0	66.7	0.1902	2.925	0.000	0.465	0.180
3.0	2.9946	67.6	1.1	66.6	0.1905	2.813	0.000	0.465	0.180
4.0	3.0035	65.5	1.1	66.6	0.1912	2.703	0.000	0.465	0.180
5.0	3.0105	63.6	1.1	66.4	0.1934	2.612	0.000	0.465	0.180
6.0	3.0211	62.3	1.1	66.0	0.1991	2.583	0.000	0.465	0.180
7.0	3.0380	61.9	1.1	65.0	0.2141	2.658	0.000	0.465	0.180
8.0	3.0567	62.7	1.1	62.4	0.2516	2.837	0.000	0.465	0.180
9.0	3.0685	64.5	1.0	56.7	0.3343	3.068	0.000	0.465	0.180
10.0	3.0686	67.0	0.9	47.1	0.4735	3.283	0.000	0.465	0.180

11.0	3.0607	69.5	0.8	37.0	0.6197	3.443	0.000	0.483	0.180
12.0	3.0541	71.6	0.7	32.6	0.6837	3.550	0.000	0.498	0.180
13.0	3.0550	73.2	0.7	36.6	0.6258	3.615	0.000	0.484	0.180
14.0	3.0597	74.4	0.7	46.5	0.4820	3.647	0.000	0.465	0.180
15.0	3.0571	75.0	0.7	56.3	0.3405	3.651	0.000	0.465	0.180
16.0	3.0373	75.4	0.8	62.2	0.2547	3.637	0.000	0.465	0.180
17.0	3.0015	75.5	0.8	64.9	0.2154	3.603	0.000	0.465	0.180
18.0	2.9610	75.6	0.8	66.0	0.1996	3.550	0.000	0.465	0.180
19.0	2.9301	75.7	0.8	66.4	0.1936	3.494	0.000	0.465	0.180
20.0	2.9161	75.7	0.9	66.6	0.1913	3.456	0.000	0.465	0.180
21.0	2.9167	75.6	0.9	66.6	0.1905	3.431	0.000	0.465	0.180
22.0	2.9248	75.2	0.9	66.7	0.1902	3.386	0.000	0.465	0.180
23.0	2.9355	74.5	0.9	66.7	0.1901	3.297	0.000	0.465	0.180
24.0	2.9482	73.4	0.9	66.7	0.1900	3.172	0.000	0.465	0.180

C. 22SEP2022 FULL DAY

yyyy/mmdd(or -ddd)/hh.h):2022/ 922/ 0.0LT geog Lat/Long/Alt=-77.8/ 166.7/ 100.0

IRIcor2 is used for topside Ne profile
URSI maps are used for the F2 peak density (NmF2)
foF2 STORM model is turned on
Shubin2015model is used for F2 peak height (hmF2)
ABT-2009 option is used for the bottomside thickness parameter B0
Scotto-97 no L option is used for the F1 occurrence probability
foE auroral storm model is turned off
IRI-1990 option is used for D-region
TBT-2012 with solar dependence is used for the electron temperature
Tru-2021 option is used for the ion temperature
RBV10+TBT15 option is used for ion composition
CGM coordinates not computed
auroral boundaries not computed

Solar and magnetic parameter for the 1st profile point:
Solar Zenith Angle/degree 101.7
Dip (Magnetic Inclination)/degree -80.63
Modip (Modified Dip)/degree -71.94
Solar Sunspot Number (12-months running mean) Rz12 65.0
Ionospheric-Effective Solar Index IG12 88.1
Solar radio flux F10.7 (daily) 137.7
Solar radio flux F10.7 (81-day average) 132.6

TEC [1.E16 m-2] is obtained by numerical integration in 1km steps
from 50 to 1500.0 km. t is the percentage of TEC above the F peak.

- HOUR	M3000	B0	B1	E-VALLEY		PLASMA FREQUENCIES / MHz			
L.T.		km		W/km	Depth	foF2	foF1	foE	foD
1.0	2.9521	116.5	0.6	17.5	0.9507	4.056	0.000	0.493	0.180
2.0	2.9738	117.8	0.7	17.5	0.9507	4.005	0.000	0.548	0.180
3.0	2.9965	119.5	0.8	17.5	0.9507	4.056	0.000	0.651	0.180
4.0	3.0228	121.6	0.9	17.5	0.9507	4.228	0.000	0.820	0.180
5.0	3.0538	124.1	0.9	17.5	0.9507	4.525	0.000	1.061	0.180
6.0	3.0855	126.8	1.0	17.5	0.9507	4.903	0.000	1.352	0.180

7.0	3.1097	129.8	1.0	17.5	0.9507	5.286	0.000	1.635	0.180
8.0	3.1186	132.8	1.0	17.5	0.9507	5.609	0.000	1.867	0.180
9.0	3.1097	135.9	1.0	17.5	0.9507	5.841	0.000	2.036	0.180
10.0	3.0873	138.7	0.9	17.5	0.9507	5.978	0.000	2.149	0.180
11.0	3.0589	140.8	0.9	17.5	0.9507	6.041	0.000	2.213	0.180
12.0	3.0305	141.6	0.9	17.5	0.9507	6.061	0.000	2.230	0.180
13.0	3.0042	140.9	0.9	17.5	0.9507	6.062	0.000	2.203	0.180
14.0	2.9797	138.7	0.9	17.5	0.9507	6.042	0.000	2.130	0.180
15.0	2.9570	135.4	0.9	17.5	0.9507	5.992	0.000	2.006	0.180
16.0	2.9375	131.5	0.8	17.5	0.9507	5.910	0.000	1.825	0.180
17.0	2.9230	127.6	0.8	17.5	0.9507	5.795	0.000	1.583	0.180
18.0	2.9134	123.9	0.8	17.5	0.9507	5.633	0.000	1.295	0.180
19.0	2.9067	120.9	0.7	17.5	0.9507	5.420	0.000	1.014	0.180
20.0	2.9016	118.6	0.6	17.5	0.9507	5.174	0.000	0.789	0.180
21.0	2.8991	116.9	0.6	17.5	0.9507	4.915	0.000	0.635	0.180
22.0	2.9022	116.0	0.6	17.5	0.9507	4.655	0.000	0.544	0.180
23.0	2.9131	115.6	0.6	17.5	0.9507	4.405	0.000	0.499	0.180
24.0	2.9309	115.8	0.6	17.5	0.9507	4.194	0.000	0.488	0.180

D. 2022 FULL YEAR 0000

yyyy/mmdd(or -ddd)/hh.h):2022/-366/ 0.0LT geog Lat/Long/Alt=-77.8/ 166.7/ 100.0

IRIcor2 is used for topside Ne profile
URSI maps are used for the F2 peak density (NmF2)
foF2 STORM model is turned on
Shubin2015model is used for F2 peak height (hmF2)
ABT-2009 option is used for the bottomside thickness parameter B0
Scotto-97 no L option is used for the F1 occurrence probability
foE auroral storm model is turned off
IRI-1990 option is used for D-region
TBT-2012 with solar dependence is used for the electron temperature
Tru-2021 option is used for the ion temperature
RBV10+TBT15 option is used for ion composition
CGM coordinates not computed
auroral boundaries not computed

Solar and magnetic parameter for the 1st profile point:
Solar Zenith Angle/degree 79.2
Dip (Magnetic Inclination)/degree -80.66
Modip (Modified Dip)/degree -71.94
Solar Sunspot Number (12-months running mean) Rz12 40.7
Ionospheric-Effective Solar Index IG12 37.3
Solar radio flux F10.7 (daily) 90.8
Solar radio flux F10.7 (81-day average) 101.3

TEC [1.E16 m-2] is obtained by numerical integration in 1km steps
from 50 to 1500.0 km. t is the percentage of TEC above the F peak.

-

DAYOF	M3000	B0	B1	E-VALLEY		PLASMA FREQUENCIES / MHz			
YEAR		km		W/km	Depth	foF2	foF1	foE	foD
1.0	2.9891	124.9	0.6	17.5	0.9507	4.505	0.000	2.065	0.180

6.0	2.9840	124.2	0.6	17.5	0.9507	4.494	0.000	2.037	0.180
11.0	2.9790	123.2	0.6	17.5	0.9507	4.482	0.000	2.001	0.180
16.0	2.9752	121.9	0.6	17.5	0.9507	4.348	0.000	1.952	0.180
21.0	2.9764	120.4	0.6	17.5	0.9507	4.430	0.000	1.888	0.180
26.0	2.9777	118.6	0.7	17.5	0.9507	4.389	0.000	1.806	0.180
31.0	2.9790	116.6	0.7	17.5	0.9507	4.357	0.000	1.708	0.180
36.0	2.9803	114.2	0.7	17.5	0.9507	4.094	0.000	1.593	0.180
41.0	2.9815	111.7	0.7	17.5	0.9507	4.285	0.000	1.459	0.180
46.0	2.9798	109.0	0.8	17.5	0.9507	4.231	0.000	1.309	0.180
51.0	2.9659	106.1	0.8	17.5	0.9507	4.060	0.000	1.150	0.180
56.0	2.9521	103.3	0.8	17.5	0.9507	3.985	0.000	0.990	0.180
61.0	2.9382	100.4	0.8	17.5	0.9507	3.862	0.000	0.840	0.180
66.0	2.9244	97.8	0.9	17.5	0.9507	3.740	0.000	0.707	0.180
71.0	2.9106	95.2	0.9	17.5	0.9507	3.515	0.000	0.595	0.180
76.0	2.9007	92.6	0.9	17.5	0.9507	3.530	0.000	0.506	0.180
81.0	2.8969	90.1	0.9	56.6	0.3465	3.497	0.000	0.448	0.180
86.0	2.8931	87.7	0.9	63.3	0.2420	3.465	0.000	0.449	0.180
91.0	2.8893	85.4	0.9	65.1	0.2136	3.442	0.000	0.450	0.180
96.0	2.8856	83.1	0.9	65.9	0.2022	3.399	0.000	0.452	0.180
101.0	2.8818	81.0	1.0	66.2	0.1967	3.428	0.000	0.454	0.180
106.0	2.8802	79.1	1.0	66.4	0.1939	3.341	0.000	0.455	0.180
111.0	2.8876	77.3	1.0	66.5	0.1923	3.346	0.000	0.456	0.180
116.0	2.8950	75.7	1.0	66.6	0.1914	3.350	0.000	0.456	0.180
121.0	2.9024	74.4	1.0	66.6	0.1909	3.355	0.000	0.457	0.180
126.0	2.9098	73.3	1.0	66.6	0.1906	3.360	0.000	0.457	0.180
131.0	2.9172	72.4	1.0	66.7	0.1904	3.364	0.000	0.458	0.180
136.0	2.9234	71.7	1.0	66.7	0.1902	3.362	0.000	0.459	0.180
141.0	2.9251	71.2	1.0	66.7	0.1901	3.330	0.000	0.460	0.180
146.0	2.9269	71.0	1.0	66.7	0.1901	3.299	0.000	0.461	0.180
151.0	2.9286	71.0	1.0	66.7	0.1901	3.267	0.000	0.462	0.180
156.0	2.9303	71.2	1.0	66.7	0.1900	3.236	0.000	0.463	0.180
161.0	2.9320	71.6	0.9	66.7	0.1900	3.204	0.000	0.464	0.180
166.0	2.9337	72.3	0.9	66.7	0.1900	3.173	0.000	0.465	0.180
171.0	2.9458	73.2	0.9	66.7	0.1900	3.172	0.000	0.465	0.180
176.0	2.9579	74.3	0.9	66.7	0.1900	3.172	0.000	0.465	0.180
181.0	2.9700	75.6	0.9	66.7	0.1900	3.171	0.000	0.465	0.180
186.0	2.9821	77.1	0.9	66.7	0.1900	3.171	0.000	0.466	0.180
191.0	2.9942	78.8	0.9	66.7	0.1900	3.170	0.000	0.467	0.180
196.0	3.0063	80.6	0.8	66.7	0.1901	3.170	0.000	0.468	0.180
201.0	2.9953	82.6	0.8	66.7	0.1901	3.326	0.000	0.468	0.180
206.0	2.9843	84.7	0.8	66.7	0.1902	3.221	0.000	0.469	0.180
211.0	2.9733	87.0	0.8	66.7	0.1902	3.247	0.000	0.469	0.180
216.0	2.9623	89.4	0.8	66.6	0.1904	3.273	0.000	0.470	0.180
221.0	2.9513	91.9	0.7	66.6	0.1906	3.426	0.000	0.470	0.180
226.0	2.9403	94.5	0.7	66.6	0.1910	3.325	0.000	0.470	0.180
231.0	2.9390	97.1	0.7	66.6	0.1918	3.516	0.000	0.471	0.180
236.0	2.9402	99.8	0.7	66.5	0.1931	3.540	0.000	0.472	0.180
241.0	2.9413	102.5	0.7	66.3	0.1955	3.657	0.000	0.473	0.180
246.0	2.9425	105.3	0.6	66.0	0.2002	3.924	0.000	0.473	0.180
251.0	2.9437	108.1	0.6	65.4	0.2101	4.001	0.000	0.474	0.180
256.0	2.9448	110.9	0.6	63.9	0.2332	4.007	0.000	0.474	0.180
261.0	2.9391	113.6	0.6	59.5	0.3017	4.114	0.000	0.475	0.180
266.0	2.9288	116.3	0.6	17.5	0.9507	4.215	0.000	0.488	0.180
271.0	2.9185	118.9	0.6	17.5	0.9507	4.315	0.000	0.569	0.180
276.0	2.9082	121.3	0.6	17.5	0.9507	4.454	0.000	0.672	0.180

281.0	2.8980	123.6	0.6	17.5	0.9507	4.516	0.000	0.798	0.180
286.0	2.8877	125.7	0.6	17.5	0.9507	4.616	0.000	0.944	0.180
291.0	2.8859	127.6	0.6	17.5	0.9507	4.712	0.000	1.103	0.180
296.0	2.8899	129.4	0.6	17.5	0.9507	4.678	0.000	1.266	0.180
301.0	2.8939	130.9	0.6	17.5	0.9507	4.898	0.000	1.425	0.180
306.0	2.8979	132.2	0.6	17.5	0.9507	4.991	0.000	1.572	0.180
311.0	2.9018	133.3	0.6	17.5	0.9507	5.084	0.000	1.702	0.180
316.0	2.9058	134.1	0.6	17.5	0.9507	5.177	0.000	1.813	0.180
321.0	2.9054	134.6	0.7	17.5	0.9507	5.217	0.000	1.869	0.180
326.0	2.8984	134.8	0.7	17.5	0.9507	5.178	0.000	1.946	0.180
331.0	2.8913	134.6	0.7	17.5	0.9507	5.140	0.000	2.009	0.180
336.0	2.8843	134.1	0.7	17.5	0.9507	5.101	0.000	2.058	0.180
341.0	2.8773	133.3	0.8	17.5	0.9507	5.063	0.000	2.096	0.180
346.0	2.8703	132.1	0.8	17.5	0.9507	5.024	0.000	2.122	0.180
351.0	2.8640	130.6	0.9	17.5	0.9507	5.011	0.000	2.138	0.180
356.0	2.8589	128.7	0.9	17.5	0.9507	5.036	0.000	2.143	0.180
361.0	2.8537	126.4	1.0	17.5	0.9507	5.060	0.000	2.137	0.180

E. 2022 FULL YEAR 1200

yyyy/mmdd(or -ddd)/hh.h):2022/-366/12.0LT geog Lat/Long/Alt=-77.8/ 166.7/ 100.0

IRIcor2 is used for topside Ne profile
URSI maps are used for the F2 peak density (NmF2)
foF2 STORM model is turned on
Shubin2015model is used for F2 peak height (hmF2)
ABT-2009 option is used for the bottomside thickness parameter B0
Scotto-97 no L option is used for the F1 occurrence probability
foE auroral storm model is turned off
IRI-1990 option is used for D-region
TBT-2012 with solar dependence is used for the electron temperature
Tru-2021 option is used for the ion temperature
RBV10+TBT15 option is used for ion composition
CGM coordinates not computed
auroral boundaries not computed

Solar and magnetic parameter for the 1st profile point:
Solar Zenith Angle/degree 54.9
Dip (Magnetic Inclination)/degree -80.66
Modip (Modified Dip)/degree -71.94
Solar Sunspot Number (12-months running mean) Rz12 40.7
Ionospheric-Effective Solar Index IG12 37.3
Solar radio flux F10.7 (daily) 90.8
Solar radio flux F10.7 (81-day average) 101.3

TEC [1.E16 m-2] is obtained by numerical integration in 1km steps
from 50 to 1500.0 km. t is the percentage of TEC above the F peak.

-

DAYOF	M3000	B0	B1	E-VALLEY		PLASMA FREQUENCIES / MHz			
YEAR		km		W/km	Depth	foF2	foF1	foE	foD
1.0	2.8648	160.0	0.8	17.5	0.9507	5.429	0.000	2.881	0.223
6.0	2.8592	158.7	0.8	17.5	0.9507	5.390	0.000	2.870	0.222

11.0	2.8536	156.9	0.9	17.5	0.9507	5.350	0.000	2.860	0.220
16.0	2.8526	154.7	0.9	17.5	0.9507	5.135	0.000	2.846	0.217
21.0	2.8704	152.2	1.0	17.5	0.9507	5.323	0.000	2.824	0.212
26.0	2.8881	149.3	1.0	17.5	0.9507	5.293	0.000	2.795	0.207
31.0	2.9059	146.2	1.0	17.5	0.9507	5.328	0.000	2.762	0.200
36.0	2.9236	142.4	1.1	17.5	0.9507	4.935	0.000	2.725	0.191
41.0	2.9414	138.3	1.1	17.5	0.9507	5.334	0.000	2.682	0.180
46.0	2.9586	134.0	1.1	17.5	0.9507	5.339	0.000	2.636	0.180
51.0	2.9737	129.5	1.1	17.5	0.9507	5.355	0.000	2.582	0.180
56.0	2.9888	124.9	1.1	17.5	0.9507	5.371	0.000	2.522	0.180
61.0	3.0040	120.3	1.1	17.5	0.9507	5.387	0.000	2.457	0.180
66.0	3.0191	116.1	1.1	17.5	0.9507	5.267	0.000	2.383	0.180
71.0	3.0342	111.8	1.1	17.5	0.9507	5.310	0.000	2.301	0.180
76.0	3.0469	107.7	1.1	17.5	0.9507	5.416	0.000	2.211	0.180
81.0	3.0561	103.5	1.1	17.5	0.9507	5.384	0.000	2.112	0.180
86.0	3.0653	99.5	1.0	17.5	0.9506	5.352	0.000	2.000	0.180
91.0	3.0745	95.7	1.0	17.6	0.9504	5.166	0.000	1.877	0.180
96.0	3.0837	91.9	1.0	17.6	0.9502	5.289	0.000	1.741	0.180
101.0	3.0929	88.3	1.0	17.6	0.9497	5.170	0.000	1.595	0.180
106.0	3.1002	84.9	1.0	17.7	0.9488	5.163	0.000	1.439	0.180
111.0	3.0994	81.8	0.9	17.7	0.9475	5.139	0.000	1.268	0.180
116.0	3.0986	79.0	0.9	17.9	0.9453	5.062	0.000	1.120	0.180
121.0	3.0978	76.5	0.9	18.1	0.9419	5.058	0.000	0.987	0.180
126.0	3.0971	74.4	0.9	18.4	0.9367	4.908	0.000	0.872	0.180
131.0	3.0963	72.6	0.9	19.0	0.9286	4.831	0.000	0.776	0.180
136.0	3.0939	71.2	0.8	19.8	0.9164	4.729	0.000	0.698	0.180
141.0	3.0849	70.1	0.8	20.9	0.8528	4.530	0.000	0.636	0.180
146.0	3.0759	69.4	0.8	22.5	0.8297	4.331	0.000	0.588	0.180
151.0	3.0669	69.0	0.8	24.6	0.7992	4.132	0.000	0.553	0.180
156.0	3.0579	69.0	0.8	27.1	0.7626	3.933	0.000	0.527	0.180
161.0	3.0489	69.4	0.8	29.7	0.7247	3.734	0.000	0.510	0.180
166.0	3.0399	70.1	0.8	31.8	0.6947	3.535	0.000	0.501	0.180
171.0	3.0517	71.3	0.7	32.6	0.6831	3.547	0.000	0.497	0.180
176.0	3.0636	72.9	0.7	31.8	0.6949	3.560	0.000	0.501	0.180
181.0	3.0754	74.8	0.7	29.7	0.7247	3.573	0.000	0.511	0.180
186.0	3.0872	77.1	0.7	27.2	0.7622	3.691	0.000	0.528	0.180
191.0	3.0990	79.6	0.7	24.7	0.7983	3.598	0.000	0.554	0.180
196.0	3.1108	82.5	0.7	22.6	0.8285	3.611	0.000	0.590	0.180
201.0	3.1136	85.6	0.7	21.0	0.8516	3.764	0.000	0.638	0.180
206.0	3.1164	89.0	0.7	19.8	0.8683	3.925	0.000	0.699	0.180
211.0	3.1192	92.7	0.7	19.0	0.8799	4.082	0.000	0.777	0.180
216.0	3.1220	96.6	0.7	18.5	0.8877	4.239	0.000	0.872	0.180
221.0	3.1247	100.7	0.8	18.1	0.8928	4.459	0.000	0.986	0.180
226.0	3.1275	105.0	0.8	17.9	0.8961	4.554	0.000	1.118	0.180
231.0	3.1215	109.4	0.8	17.8	0.9473	4.659	0.000	1.265	0.180
236.0	3.1134	114.0	0.8	17.7	0.9487	4.991	0.000	1.439	0.180
241.0	3.1052	118.6	0.8	17.6	0.9496	5.216	0.000	1.600	0.180
246.0	3.0970	123.4	0.8	17.6	0.9501	5.442	0.000	1.753	0.180
251.0	3.0889	128.2	0.8	17.6	0.9504	5.753	0.000	1.895	0.180
256.0	3.0807	133.1	0.9	17.5	0.9506	5.892	0.000	2.024	0.180
261.0	3.0573	137.8	0.9	17.5	0.9507	6.016	0.000	2.143	0.180
266.0	3.0238	142.5	0.9	17.5	0.9507	6.072	0.000	2.251	0.180
271.0	2.9903	147.0	0.9	17.5	0.9507	6.181	0.000	2.346	0.180
276.0	2.9567	151.3	0.9	17.5	0.9507	6.186	0.000	2.431	0.180
281.0	2.9232	155.3	1.0	17.5	0.9507	6.260	0.000	2.510	0.180

286.0	2.8897	159.0	1.0	17.5	0.9507	6.297	0.000	2.584	0.180
291.0	2.8739	162.4	1.0	17.5	0.9507	6.323	0.000	2.650	0.180
296.0	2.8699	165.5	1.0	17.5	0.9507	6.060	0.000	2.705	0.180
301.0	2.8659	168.2	1.0	17.5	0.9507	6.335	0.000	2.756	0.192
306.0	2.8618	170.5	1.1	17.5	0.9507	6.341	0.000	2.804	0.205
311.0	2.8578	172.3	1.1	17.5	0.9507	6.347	0.000	2.847	0.216
316.0	2.8538	173.7	1.1	17.5	0.9507	6.353	0.000	2.883	0.225
321.0	2.8451	174.5	1.1	17.5	0.9507	6.338	0.000	2.859	0.232
326.0	2.8293	174.7	1.1	17.5	0.9507	6.291	0.000	2.887	0.238
331.0	2.8136	174.2	1.1	17.5	0.9507	6.244	0.000	2.911	0.243
336.0	2.7978	173.1	1.2	17.5	0.9507	6.197	0.000	2.930	0.246
341.0	2.7821	171.3	1.2	17.5	0.9507	6.150	0.000	2.945	0.249
346.0	2.7663	168.8	1.2	17.5	0.9507	6.102	0.000	2.956	0.251
351.0	2.7543	165.6	1.2	17.5	0.9507	6.068	0.000	2.963	0.252
356.0	2.7479	161.7	1.2	17.5	0.9507	6.052	0.000	2.965	0.252
361.0	2.7416	157.0	1.2	17.5	0.9507	6.037	0.000	2.963	0.252

LIST OF REFERENCES

[1] K. Nessly, "Informing Terrestrial Passive Radar Experimental Design Using Jupiter's Radio Emissions for Echo Detection," presented at the AGU Fall Meeting 2022, Chicago IL, Chicago IL, Dec. 14, 2022.

[2] Christopher Gerekos, Lorenzo Bruzzone, and Masafumi Imai, "Coherent Method for Simulating Active and Passive Radar Sounding of the Jovian Icy Moons," IEEE Transactions on Geoscience and Remote Sensing, vol. 58, no. 4, Apr. 2020.

[3] Thomas F, Tascione, "Chapter 2: Solar Physics," in Introduction to the Space Environment, 2nd ed.Malabar, FL: Krieger Publishing Company, 2010.

[4] "Solar radiation at radio frequencies and its relation to sunspots," Proc. R. Soc. Lond. A, vol. 190, no. 1022, pp. 357–375, Aug. 1947, doi: 10.1098/rspa.1947.0081.

[5] Peters, S. T., Nessly, K., Roberts, T. M., Schroeder, D. M., and Romero-Wolf, A., "Assessing Spatial Coherence Constraints on Passive Radar Experiments Using Radio-Astronomical Sources for Echo Detection," vol. 2022, 2022.

[6] S. T. Peters et al., "Glaciological Monitoring Using the Sun as a Radio Source for Echo Detection," Geophysical Research Letters, vol. 48, no. 14, Jul. 2021, doi: 10.1029/2021GL092450.

[7] G. Steinbruegge et al., "PRIME — A Passive Radar Sounding Concept for Io," Bulletin of the AAS, vol. 53, no. 4, Mar. 2021, doi: 10.3847/25c2cfeb.49659984.

[8] P. Zarka et al., "Jupiter radio emission induced by Ganymede and consequences for the radio detection of exoplanets," A&A, vol. 618, p. A84, Oct. 2018, doi: 10.1051/0004-6361/201833586.

[9] S. T. Peters, D. M. Schroeder, M. S. Haynes, D. Castelletti, and A. Romero-Wolf, "Passive Synthetic Aperture Radar Imaging Using Radio-Astronomical Sources," IEEE Trans. Geosci. Remote Sensing, vol. 59, no. 11, pp. 9144–9159, Nov. 2021, doi: 10.1109/TGRS.2021.3050429.

[10] L. Carrer, D. M. Schroeder, A. Romero-Wolf, P. A. Ries, and L. Bruzzone, "Analysis of Temporal and Structural Characteristics of Jovian Radio Emissions for Passive Radar Sounding of Jupiter's Icy Moons," IEEE Trans. Geosci. Remote Sensing, vol. 59, no. 5, pp. 3857–3874, May 2021, doi: 10.1109/TGRS.2020.3023249.

[11] M. Yoneda et al., “Io’s volcanism controls Jupiter’s radio emissions: IO’S VOLCANIC ROLE ON THE HOM EMISSION,” Geophys. Res. Lett., vol. 40, no. 4, pp. 671–675, Feb. 2013, doi: 10.1002/grl.50095.

[12] K. Imai, L. Wang, and T. D. Can, “Modeling Jupiter’s decametric modulation lanes,” J. Geophys. Res., vol. 102, no. A4, pp. 7127–7136, Apr. 1997, doi: 10.1029/96JA03960.

[13] B. Cecconi et al., “Natural radio emission of Jupiter as interferences for radar investigations of the icy satellites of Jupiter,” Planetary and Space Science, vol. 61, no. 1, pp. 32–45, Feb. 2012, doi: 10.1016/j.pss.2011.06.012.

[14] T. D. Carr et al., “Very Long Baseline Interferometry of Jupiter at 18 MHz,” Radio Sci., vol. 5, no. 10, pp. 1223–1226, Oct. 1970, doi: 10.1029/RS005i010p01223.

[15] C. K. Louis et al., “Latitudinal Beaming of Jupiter’s Radio Emissions From Juno/Waves Flux Density Measurements,” JGR Space Physics, vol. 126, no. 10, Oct. 2021, doi: 10.1029/2021JA029435.

[16] T. M. Roberts, A. Romero-Wolf, L. Bruzzone, L. Carrer, S. Peters, and D. M. Schroeder, “Conditioning Jovian Burst Signals for Passive Sounding Applications,” IEEE Trans. Geosci. Remote Sensing, vol. 60, pp. 1–14, 2022, doi: 10.1109/TGRS.2021.3109106.

[17] A. Romero-Wolf, S. Vance, F. Maiwald, E. Heggy, P. Ries, and K. Liewer, “A passive probe for subsurface oceans and liquid water in Jupiter’s icy moons,” Icarus, vol. 248, pp. 463–477, Mar. 2015, doi: 10.1016/j.icarus.2014.10.043.

[18] C. Grima, D. D. Blankenship, and D. M. Schroeder, “Radar signal propagation through the ionosphere of Europa,” Planetary and Space Science, vol. 117, pp. 421–428, Nov. 2015, doi: 10.1016/j.pss.2015.08.017.

[19] Radio-Sky Publishing, “Radio-Sky Radio-Jupiter Pro 3.” Radio-Sky Publishing. [Online]. Available: http://www.radiosky.com/

[20] Peters, Sean, Schroeder, Dustin, Castelletti, D., Haynes, M., and Romero-Wolf, Andrew, “In Situ Demonstration of a Passive Radio Sounding Approach Using the Sun for Echo Detection,” IEEE Transactions on Geoscience and Remote Sensing, vol. 56, Dec. 2018.

[21] J. Yue, M.-Y. Chou, and D. Bilitza, “International Reference Ionosphere 2020 InstantRun.” Community Coordinated Modeling Center. [Online]. Available: https://kauai.ccmc.gsfc.nasa.gov/instantrun/iri

[22] Sean Peters, Schroeder, Dustin, and Romero-Wolf, Andrew, "Passive radio sounding to correct for Europa's ionospheric distortion of VHF signal," *Planetary and Space Science*, vol. 187, 2020, [Online]. Available: https://www.sciencedirect.com/science/article/pii/S0032063319301424

[23] S. T. Peters, T. M. Roberts, K. Nessly, D. M. Schroeder and A. Romero-Wolf, "Revisiting the Limits of Spatial Coherence for Passive Radar Sounding Using Radio-Astronomical Sources," IGARSS 2022 - 2022 IEEE International Geoscience and Remote Sensing Symposium, Kuala Lumpur, Malaysia, 2022, pp. 3880–3883, doi: 10.1109/IGARSS46834.2022.9884673.

[24] Karissa Nessly, Sean Peters, Gregor Steinbrugge, Dustin Schroeder, and Andrew Romero-Wolf, "System Parameter Constraints On Terrestrial Passive Radar Sounding Using Jovian Decametric Radiation," IEEE Geoscience and Remote Sensing Society, Accepted 2023.

THIS PAGE INTENTIONALLY LEFT BLANK

INITIAL DISTRIBUTION LIST

1. Defense Technical Information Center
   Ft. Belvoir, Virginia

2. Dudley Knox Library
   Naval Postgraduate School
   Monterey, California